WARSAW UNIVERSITY OF TECHNOLOGY

FACULTY OF MECHATRONICS

Ph.D. Thesis

Maciej Szudarek, M.Sc.

Modelling selected properties
of mechanical oscillator flowmeters

Modelowanie wybranych właściwości
przepływomierzy z oscylatorem mechanicznym

Supervisor
dr hab. inż. Mateusz Turkowski, prof. PW

Co-supervisor
dr inż. Adam Piechna

Warsaw 2020

Podziękowania

Chciałbym podziękować osobom, dzięki którym mogłem spełnić swoje marzenie prowadzenia badań naukowych i napisania niniejszej rozprawy doktorskiej.

Szanownemu Panu Profesorowi PW dr hab. inż. Mateuszowi Turkowskiemu dziękuję za zainteresowanie mnie dziedziną metrologii przepływów jeszcze na studiach inżynierskich, życzliwość, o której zawsze będę pamiętać i nieocenione merytoryczne wsparcie, na które zawsze mogłem liczyć.

Dziękuję promotorowi pomocniczemu dr inż. Adamowi Piechnie, za wiele cennych rad, zaangażowanie i za wprowadzenie mnie w fascynującą dziedzinę numerycznej mechaniki płynów.

Mojej mamie i Kasi, za wsparcie i anielską cierpliwość, zwłaszcza gdy sam miewałem chwile zwątpienia.

Dyrektorowi Instytutu Metrologii i Inżynierii Biomedycznej prof. dr hab. inż. Adamowi Woźniakowi, za udzielone wsparcie finansowe dla Laboratorium Przepływów.

Kolegom z Instytutu: Michałowi Nowickiemu, Piotrowi Gaździe, Pawłowi Nowakowi, Arturowi Szczeckiemu, Tomaszowi Charubinowi, Andrzejowi Jusiowi i Maciejowi Kachniarzowi, za wzajemną mobilizację i niepowtarzalną atmosferę pracy.

Streszczenie

Słowa kluczowe: metrologia przepływów, numeryczna mechanika płynów, modelowanie

W niniejszej rozprawie doktorskiej poruszono tematykę właściwości metrologicznych i użytkowych przepływomierzy z oscylatorem mechanicznym. Głównym celem pracy było zwiększenie zakresu stosowalności tych urządzeń poprzez rozwój stanu wiedzy oraz weryfikację dotychczasowych modeli i założeń. Badania zostały zawężone do konstrukcji przepływomierza, która z powodzeniem była stosowana w przemyśle. W ramach pracy opracowano model numeryczny przepływomierza i wykonano jego walidację. Pozwolił on na zbadanie pracy przepływomierza dając szereg informacji dotyczących jego działania. Wykazano, że nieliniowość charakterystyki przepływomierza wynika między innymi ze zmienności kształtu wlotowego profilu prędkości w funkcji liczby Reynoldsa. Przedstawiono metodę poprawy liniowości charakterystyki, która zwiększa zakresowość przepływomierza z 6:1 do 26:1 przy nieliniowościach nieprzekraczających 0,5%. Wykorzystując opracowany model przeprowadzono symulacje wariantowe zmieniając parametry pracy przepływomierza oraz jego wymiary i konfiguracje geometryczne. Na podstawie badań eksperymentalnych określono wytyczne dla projektanta i wykazano, że bezwymiarowa sztywność F jest poprawnym kryterium optymalizacji geometrii. Poprawia ona próg rozruchu przepływomierza i zmniejsza wpływ tarcia w łożyskach na charakterystykę przetwarzania. W ramach pracy zebrano cenne dane dotyczące wymagań instalacyjnych. Na podstawie przeprowadzonych doświadczeń wykazano, że dotychczasowe zalecenia dotyczące długości odcinków dolotowych mogą zostać złagodzone. Zaproponowano również metodę szacowania wpływu zaburzeń w układzie dolotowym na pracę przepływomierza na bazie wyników uproszczonego modelu numerycznego. Wykazano, że w przypadku obecności pulsacji przepływu możliwe jest wystąpienie zjawiska unoszenia częstotliwości. W ramach pracy przeprowadzono również unikatowe w skali światowej badania w warunkach kriogenicznych. W wyniku badań przy zastosowaniu ciekłego azotu i skroplonego gazu ziemnego dowiedziono, że przepływomierz z oscylatorem mechanicznym z powodzeniem może pracować w warunkach kriogenicznych. Na podstawie otrzymanych wyników wykazano, że przepływomierz spełnia wymogi metrologiczne stawiane instalacjom do pomiaru skroplonego gazu ziemnego. W rezultacie PGNiG wykazało zainteresowanie wdrożeniem przepływomierza do pomiaru skroplonego gazu ziemnego w lokalnych punktach regazyfikacji w Polsce. Wyniki otrzymane w ramach niniejszej pracy są w dużej mierze unikatowe i nie były do tej pory publikowane przez nikogo w czasopismach naukowych.

Abstract

Keywords: flow metrology, computational fluid dynamics, modelling

The thesis investigates the metrological and operational properties of mechanical oscillator flowmeters. The objective was to broaden their application range by providing validation and extension of existing studies. The thesis focused on a particular design of the flowmeter that was validated in the industrial environment. A computational fluid dynamics model of a mechanical oscillator flowmeter was developed and validated. The developed model provided insight into the principle of operation of the flowmeter and allowed for design exploration. It was demonstrated that the nonlinearity of the calibration curve of the flowmeter is among others a result of the shape of the inlet flow profile, which is a function of Reynolds number. A cost-effective method of improving linearity was examined, which allows increasing rangeability of the flowmeter from 6:1 to 26:1 for nonlinearities below 0,5%. Previous studies on the optimal shape of the oscillator were verified and extended. Parametric study allowed outlining design recommendations and confirmed that maximizing the nondimensional stiffness F is a correct optimization parameter. It improves the threshold flow rate for flowmeter operation and reduces the influence of bearing wear. Valuable data regarding installation requirements were collected. Basing on the conducted experimental study it was demonstrated that previous recommendations on inlet pipe lengths may be relaxed. It was shown that the impact of disturbance sources not covered by the study can be verified with the use of a simplified numerical model. It was verified, that in the case of pulsatile flow the frequency lock-in phenomenon may occur. Of practical significance was also the study on alternative methods of oscillation frequency measurement. Inductive proximity sensors, Hall sensors and fast piezoelectric pressure sensors may extend the application range of mechanical oscillator flowmeter. Finally, a study on cryogenic fluids was conducted with the use of liquid nitrogen and liquefied natural gas, which was unique on a global scale. It was a huge organizational effort and required preparing an ATEX-certified measurement system. In the study, it was verified that the mechanical oscillator flowmeter not only operates properly in cryogenic conditions, but also meets the legal criteria of LNG measurement. Basing on the experimental results the potential of the flowmeter was ultimately confirmed. At the time of writing the thesis, PGNiG has stated interest in investing in this measurement method for the measurement of LNG at local regasification plants in Poland. All in all, the main objective stated in the thesis was accomplished. The results presented in this work are mostly unique and have not been published in scientific journals.

Nomenclature

a	body force per unit mass (m/s^2)
A	cross-sectional area (m^2)
A_p	pulsation amplitude (-)
b	baffle height (m)
c	sensitivity coefficient
C_C	Coriolis coefficient (-)
C_φ	spring stiffness equivalent (N/m)
C_f	flatness parameter (-)
C_{fm}	momentum of flatness parameter (-)
C_M	moment coefficient (-)
D	pipe diameter (m)
E	relative error (%)
E_k	kinetic energy (J)
f	frequency (Hz)
f_o	oscillator frequency (Hz)
f_{os}	oscillator frequency in steady flow conditions (Hz)
f_p	frequency of pulsatile flow (Hz)
F	nondimensional stiffness, criterial function for optimizing oscillator's geometry (-)
g	gravitational acceleration (m/s^2)
G	grid number (-)
h	height (m) / representative cell size (m)
I	moment of inertia ($kg \cdot m^2$)
j	auxiliary parameter that groups oscillator dimensions ($m^{-3/2} \cdot kg^{-1/2}$)
k	coverage factor (-)
k', k'_d	components of the F function (-)
K	volumetric calibration constant ($1/m^3$)
K_m	mass calibration constant (1/kg)
l	level arm (m)
L	length (m)
m	mass (kg)
p	pressure (Pa)

p_{NON}	nondimensional pressure $p / \rho v^2$ (-)
P	force (N)
q_m	mass flow rate (kg/s)
q_v	volumetric flow rate (m^3/s)
Q	Q-criterion ($1/s^2$)
r	refinement factor (-) / correction factor for density (m^3/kg)
R	radius (m)
Ra	roughness average (m)
Re	Reynolds number (-)
Re_{os}	Reynolds number based on the amplitude of the oscillatory component of cross-sectional mean velocity (-)
Re_{ta}	Reynolds number based on time-averaged value of cross-sectional mean velocity (-)
Rp	maximum profile peak height (m)
Rv	maximum profile valley depth (m)
Rz	maximum height of the profile (m)
s	width (m)
S_a	swirl angle (rad)
S_n	swirl number (-)
t	time (s)
T	temperature (K)
v	velocity (m/s)
v’	variable component of velocity (m/s)
v_{NON}	nondimensional velocity, $v/\bar{v}$ (-)
v_r	radial velocity (m/s)
v_x	axial velocity (m/s)
$v_{x\,ref}$	reference axial velocity (m/s)
v_Θ	circumferential velocity (m/s)
V	volume (m^3)
w	mean velocity in a channel of a stream divider (m/s)
x	linear position (m)
x_{CG}	distance between rotation axis and the center of gravity (m)
y^+	nondimensional wall distance (-)
z	distance between the rear edge of the oscillator and the baffle (m)

α, γ	angles describing the shape of oscillator (rad)
β	diameter ratio (-)
δ	Kronecker delta (-)
Δp	pressure difference (Pa)
Δt	time step (s)
ε	roughness height (m)
θ	dominant eigenvalue (-)
λ_T	linear thermal expansion coefficient (1/K)
μ	dynamic viscosity (Pa·s)
ν	kinematic viscosity (m^2/s)
ξ	pressure loss coefficient (-)
ρ	density (kg/m^3)
τ	torque (Nm)
φ	angular position (rad)
ψ	trigonometric expression (-)
ω	angular velocity (rad/s)
$\sqrt{\omega'}$	dimensionless pulsation parameter (-)
$( )_0$	initial value of ( )
$\overline{( )}$, $( )_{RMS}$	mean value of ( ), root mean square of ( )
$u( )$	standard uncertainty of ( )
$U_{95}( )$	expanded uncertainty of ( ) for coverage factor of $k = 2$

CFD	Computational Fluid Dynamics
CFL	Courant-Friedrichs-Lewy condition
LCOs	Limit Cycle Oscillations
LNG	Liquefied Natural Gas
MPE	Maximum Permissible Error
PGNiG	Polskie Górnictwo Naftowe i Gazownictwo (Polish Oil and Gas Company)
PSG	Polska Spółka Gazownictwa (Polish Operator of the Gas Distribution System)
RANS	Reynolds-Averaged Navier-Stokes

Table of contents

Chapter 1 Introduction 13
1.1 The motivation for the work 13
1.2 Structure of the thesis 15
Chapter 2 Literature review 16
2.1 Oscillatory flowmeters with a moving body 16
2.2 Analytical models 20
2.2.1. Principle of operation 20
2.2.2. Geometry optimization attempts 22
2.2.3. Oscillator's dynamics 22
2.2.4. Summary 23
2.3 Comparison with other flowmeter types 23
Chapter 3 Objective of the work 26
Chapter 4 Experimental setup 27
4.1 Selected flowmeters 27
4.2. Water calibration facility 30
4.3. Low-pressure air facility 32
4.4. Bell prover 34
4.5. Calibration with liquid nitrogen and liquefied natural gas 34
Chapter 5 Development of a numerical model 35
5.1 Introduction 35
5.2 Geometry and boundary conditions 37
5.3 Meshing strategy and solver settings 40
5.3.1. Static mesh 40
5.3.2. Dynamic mesh 41
5.3.3. Solver settings and convergence criteria 44
5.4 Grid independence test 44
5.5 Time step sensitivity study 46
5.6 Practical remarks 51
Chapter 6 Modelling 53
6.1 Discussion about the principle of operation 53
6.2 A method of improving calibration curve linearity 58
6.2.1 Introduction and methods 58
6.2.2 Results and discussion 59

6.2.3 Conclusions 63
Chapter 7 Influence of oscillator's shape on the energy of oscillations 64
7.1. Previous findings 64
7.2 Parametric study 68
7.2.1. Static cases 68
7.2.2. Dynamic cases 71
7.3 The positive effects of increased energy of the oscillations 78
7.4 Bearing wear 82
7.4.1. Introduction 82
7.4.2. Constructed test stand 83
7.4.3. Quantification of forces acting on the oscillator 84
7.4.4. Summary 85
Chapter 8 Installation constraints 86
8.1 Inlet flow disturbance effects 86
8.1.1 Introduction 86
8.1.2. Methods 89
8.1.3. Results and discussion 91
8.1.4. Conclusions 100
8.2 Performance in the presence of pulsatile flow 101
8.2.1. Introduction 101
8.2.2. Test stand 102
8.2.3. Results and discussion 105
8.2.4. Conclusions 108
8.3 Influence of pipe wall roughness 110
8.3.1. Introduction 110
8.3.2. Methods 110
8.3.3. Results and discussion 112
8.3.4. Conclusions 113
Chapter 9 Experiments in cryogenic conditions 114
9.1 Influence of density and temperature on calibration constant 114
9.1.1. Introduction 114
9.1.2. Materials and methods 116
9.1.3. Results and discussion 119
9.2 Performance in cryogenic conditions 119
Chapter 10 Summary 125

10.1 Main contributions 125
10.2 Future study directions 127
10.3 Acknowledgements 128
References 129
Appendix Uncertainty analysis 140
A.1.1 Calibration using water 140
A.1.2 Calibration using air, low-pressure air facility 141
A.1.3 Calibration using air, bell prover 142
A.1.4 Calibration using liquid nitrogen and LNG 143
A.1.5 Density correction coefficient *r* 144

Chapter 1

Introduction

1.1 The motivation for the work

There are no universal flowmeters which are suitable for all the applications, each has its strengths and limitations. Selecting proper technology for the measurement task requires that the user considers parameters of the fluid such as density, viscosity, conductivity, lubricity, abrasiveness, compressibility or flammability. In industrial conditions, these parameters may vary in wide limits and their influence on the flow measurement can be complex. Other important factors are flow stability, operating temperature, operating pressure, permissible pressure drop and many others. An area where the requirements on the flow measurement accuracy are the strictest is the custody transfer of large quantities of high-value fluids. Rigorous standards of performance may be also demanded in control applications, where the fluid quantity impacts the quality of the final product. Meanwhile, new technologies and applications pose even more stringent requirements on the accuracy and reliability of the flow measurement, especially conventional and nuclear energy production. For that reason, researchers seek new solutions to measure single-phase and multi-phase flows more accurately.

One such a new application is the custody transfer of liquefied natural gas (LNG). After the inauguration of an LNG import terminal in Świnoujście in 2015, the LNG market in Poland has substantially grown. Small-scale LNG liquefaction plants are suitable for deliveries of natural gas to remote areas not connected to pipelines (Blacharski *et al.*, 2016). At present in Poland neither tank trucks nor the final customers possess flowmeters dedicated to LNG measurement. Therefore the market is limited to the customers that can receive the entire gas load of a tanker truck. Direct measurement with a flowmeter would allow dividing the load and increasing the number of LNG users. As the customer interest in this energy source is constantly growing, the installation of dedicated flowmeters at a large scale is inevitable (PGNiG, 2018).

The problem of LNG measurement is of growing importance worldwide, not only in Poland. Numerous ongoing projects, e.g. run by Euramet (EURAMET, 2010, 2017), are contributing to clarify and reduce measurement uncertainties by developing measurement standards, methods and procedures. LNG is a natural gas that has been cooled below its boiling point, which is -160°C at the atmospheric pressure. In its liquid state, natural gas has a density of ca.

450 kg/m^3 and viscosity of $1 \cdot 10^{-4}$ Pa·s, which is roughly 45% and 10% that of water, correspondingly (GIIGNL, 2017). The legal requirements in Poland (Dz. U. 2016 Poz. 815, 2016) specify the maximum permissible error related to the measured value (MPE) of the measurement installation as 2,5% with a ratio of the maximum to the minimum flow rate (rangeability) of 5:1. The threshold MPE is said to be reduced down to 1,5% in the near future.

Several LNG flowmeter installations have already been established worldwide and the conclusions are as follows (Lucas and Pelevic, 2017). The measurement is troublesome and the key issue is the low operating temperature, as it affects the flowmeter's dimensions and material properties. The most often used type of flowmeters is Coriolis meter, which has a major advantage in that it measures the mass flow rate directly. However, both its initial and operational costs are high. What is more, cryogenic fluids such as LNG are stored and pumped at conditions close to the local saturation temperature. Large pressure drops across Coriolis flowmeter may cause vapor bubbles to form and deteriorate its measurement accuracy. Turbine flowmeters are not well-suited to cryogenic fluids. The low viscosity of LNG leads to poor lubricity and an increased wear of precision bearings. Ultrasonic flowmeters in form of clamp-on transducers are non-invasive. However, they infer the volumetric flow rate from an average velocity measured in several sonic paths, therefore ultrasonic flowmeters are susceptible to flow disturbances (Spitzer, 2001). Differential pressure meters have accuracy and rangeability that do not meet legal requirements for LNG measurement. Vortex flowmeters are susceptible to vibrations generated by pumps. All things considered, each of the flowmeter types has its flaws and there are potentially other solutions for this measurement task.

The thesis focuses on mechanical oscillator flowmeters. Similarly to the vortex and fluidic flowmeters, they utilize naturally occurring oscillations whose frequency varies with the flow velocity. Such a class of meters is often called oscillatory meters (Spitzer, 2001). Unlike vortex-shedding flowmeters that have a stationary bluff body, mechanical oscillator flowmeters have a bluff body that oscillates with the flow. Mechanical oscillator flowmeters have been introduced into the market in response to the need of the industry for rugged, accurate meters that would cover a wider measurement range than orifice flowmeters (Turkowski, 2003b). Although these devices currently have a limited share in the market, they are still mentioned in the latest flow measurement handbooks (Baker, 2016) and the interest in the development of this type of flowmeters is continued (Mahulikar and Sane, 2005). Baker suggested that it would be interesting to know whether there is commercial interest in such a meter. The present work can be treated as an attempt to answer this question.

As shown by the example of LNG measurement, the application potential for mechanical oscillator flowmeters is still present. The main barrier is the lack of published results of their performance in cryogenic applications. The problem concerns many other applications as well, as existing works on mechanical oscillator flowmeters are few and they require validation and extension to specify installation requirements in industrial conditions. What is more, most of the studies have been conducted in the ‘80s and ‘90s, when Computational Fluid Dynamics (CFD) has not yet been a viable scientific tool in flow metrology. Current knowledge may be therefore expanded.

1.2 Structure of the thesis

The thesis is organized as follows. Chapter 2 presents a critical literature review on mechanical oscillator flowmeters. Chapter 3 establishes the goals of the work against state of the art. Chapter 4 presents details of studied flowmeter designs and test stands used for the study. Chapter 5 describes the development and validation of a numerical model. With its aid, analysis of flowmeter operation is performed in Chapter 6 and a parametric study is conducted in Chapter 7. Chapter 8 presents the study on the installation requirements. Chapter 9 reports the experiments conducted in cryogenic conditions. A summary and evaluation of the gathered data and proposed solutions are given in Chapter 10. Future study directions are outlined. Uncertainty budgets are presented in the Appendix.

Chapter 2

Literature review

2.1 Oscillatory flowmeters with a moving body

Periodic oscillations of bodies in the presence of flow are a well-known phenomenon (Williamson and Govardhan, 2004). Formally, such a body operates in a stable limit cycle, which is an isolated closed trajectory (Figure 2.1). Neighboring trajectories are not closed and they spiral toward the cycle (Stramigioli and Van Dijk, 2008; Giné, 2013).

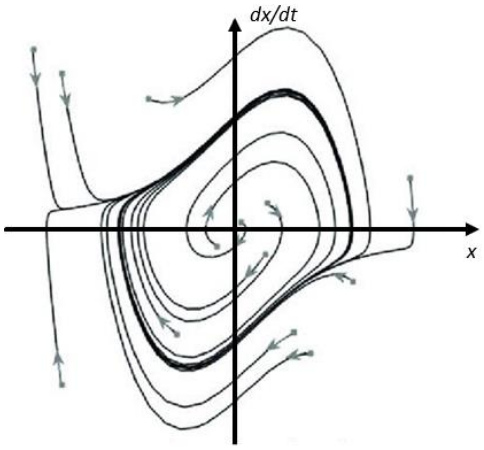

Figure 2.1: Phase plane diagram for the unforced van der Pol oscillator, figure adapted from (Hellevik and Gudmestad, 2017).

Such behavior is exhibited in some of the nonlinear systems, where variable amplification is present, especially if nonlinear terms introduce a phase shift or negative damping in the range of low amplitudes (Thaler and Pastel, 1965; Gibson, 1968; Hayashi, 1968). In engineering practice, the limit cycle is commonly caused by vortex street shedding off the body. The energy loss in a cycle caused e.g. by friction is compensated by the energy extracted from the flow. This has been a subject of numerous studies, e.g. (Balasubramanian and Skop, 1996; Facchinetti, Langre and Biolley, 2002, 2004), as vortex-induced vibrations are a potential cause of fatigue damage for chimneys, suspended bridge cables, power transmission lines, etc. In the field of flow metrology, negative effects concern resonance and fatigue damage of thermowells (Blevins, Tilden and Martens, 1998; Bartran *et al.*, 1999) or averaging pitot tubes (Kabacinski, Lachowicz and Pospolita, 2008; Kabaciński, Lachowicz and Pospolita, 2013). For a simple geometry of a pendulum in a channel subjected to an incoming flow, there were attempts of

analytical description of the phenomena (Bandi *et al.*, 2013; Fani and Gallaire, 2014; Orchini, Kellay and Mazzino, 2015).

On the positive note, it is possible to take advantage of the stability of the limit cycle in propulsion and power extraction applications (Ramesh, Murua and Gopalarathnam, 2015). In the field of flow metrology, the fact that for a given flow rate the amplitude and frequency of oscillations are constant is also favorable.

Early reports of a flowmeter based on a body that oscillates with the flow date back to 1944 (Lagasse, 1944). In this design, two angularly arranged rectangular blades were secured to a pivoted shaft, which extended centrally through a rectangular duct (Figure 2.2a). If a moving body was initially in a neutral position, oscillations would be excited by turbulence. Once disturbed from the equilibrium position, the body was moved in the direction of one of the duct walls because of the greater pressure force acting on one of the blades. When the blade reached the housing wall, it would choke the flow on one side and force the flow towards the second blade, causing the shaft to rotate in the opposite direction. Given that the velocity exceeded the threshold value, the oscillation frequency was proportional to the flow rate. The frequency of oscillations was measured with the use of an arm extending from the shaft, which periodically shadowed a photoelectric cell.

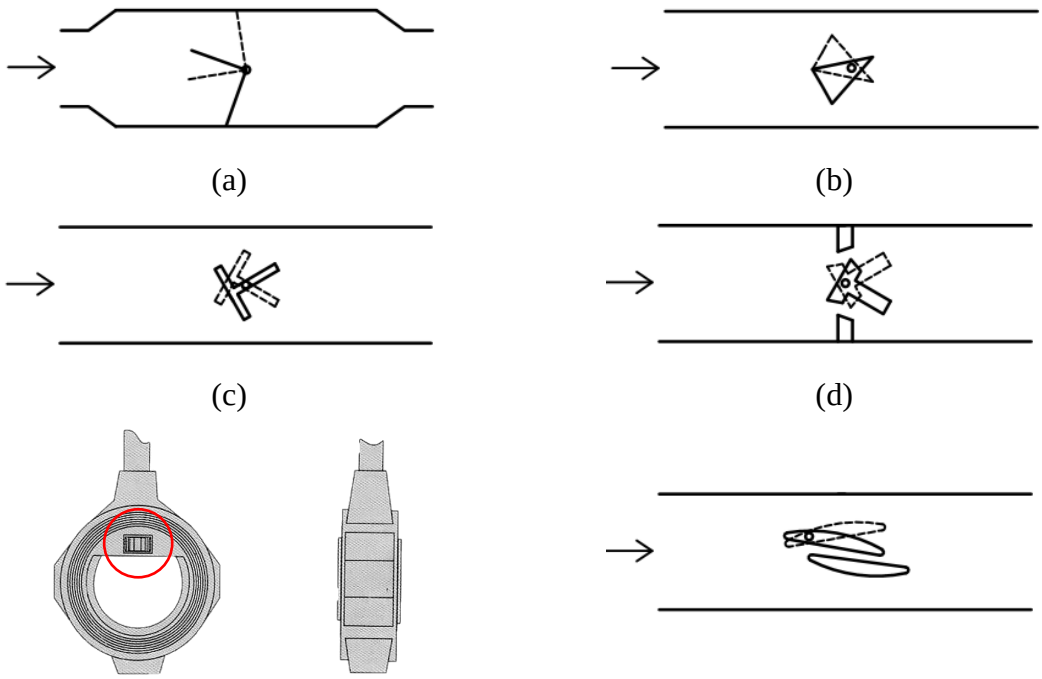

Figure 2.2: Early designs of a mechanical oscillator flowmeter. (a) V-shaped oscillator, figure adapted from (Lagasse, 1944); (b) prism-shaped oscillator, figure adapted from (Shimomura,

1980); (c) T-shaped oscillator, figure adapted from (Shimomura, 1980); (d) design by Waugh and Bahrton, figure adapted from (Bahrton, 1981); (e) design by (Badger Meter Europe, 1985), the oscillator is marked with a circle; (f) oscillating wing, figure adapted from (DeCarlo, 1982).

Numerous improvements have been developed concerning the shape of the oscillating body over the years. (Shimomura, 1980) presented prism-shaped and T-shaped oscillators (Figure 2.2b and c). Besides patent descriptions, no experimental data on metrological nor operational properties are available. Designs proposed by (Waugh, 1963) and (Bahrton, 1981) presented in Figure 2.2d were commercially manufactured by (Badger Meter Europe, 1985) in DN25, DN50 and DN80 variants. Eddy current proximity sensors detected the oscillations of the body. MPEs of 0,5% of the measured value were claimed for the measurement range of (4,8 – 48) m^3/h for water, for the DN50 flowmeter. The shortcoming of this design was that it significantly choked the flow in the neutral position of the oscillator. For that reason, an orifice was installed in a flowmeter body, which directed only part of the flow to the mechanical oscillator flowmeter (Figure 2.2e). This introduced limitations in the case of measurement of low flow rates and in the case of small pipe diameters. (DeCarlo, 1978, 1982) studied design of two wing-shaped bodies, one of which was stationary and the second was pivotally mounted (Figure 2.2f). This device took advantage of a dynamic stall effect combined with a Venturi effect that drew the oscillator towards the fixed wing. It found applications in the measurement of large flow rates in rectangular ventilation ducts. (Peisker and Bohac, 1980) and (Boszniak and Słowskij, 1976) proposed the design of vibrating ball for low flow rates. Ball-type designs were less popular, as they featured narrow gaps so that any foreign solid object could severely affect their performance, plus their error curves were highly nonlinear. On the other hand, due to the simplicity of the geometry, their error curves could have been described with an analytical model (Mahulikar and Sane, 2005).

In the presented designs, oscillating bodies were excited by the flow from both sides at all times, which negatively affected the durability of bearings. (Heckle, 1971, 1973, 1974; Lutz, 1973) introduced a design that utilized a stream divider (Figure 2.3a). The device was of simple construction, sufficient accuracy, and it was resistant to dirt and sediment to some extent. It was manufactured for DN15, DN25, DN50 and DN80 diameters by Rota company (Figure 2.3b). MPEs of 0,5% of the measured value were reported in the range of (4 – 40) m^3/h for the measurement of water. The shortcoming was that the design required the proximity of walls to enhance and stabilize the oscillations. For that reason, the body of a flowmeter had a rectangular cross-section.

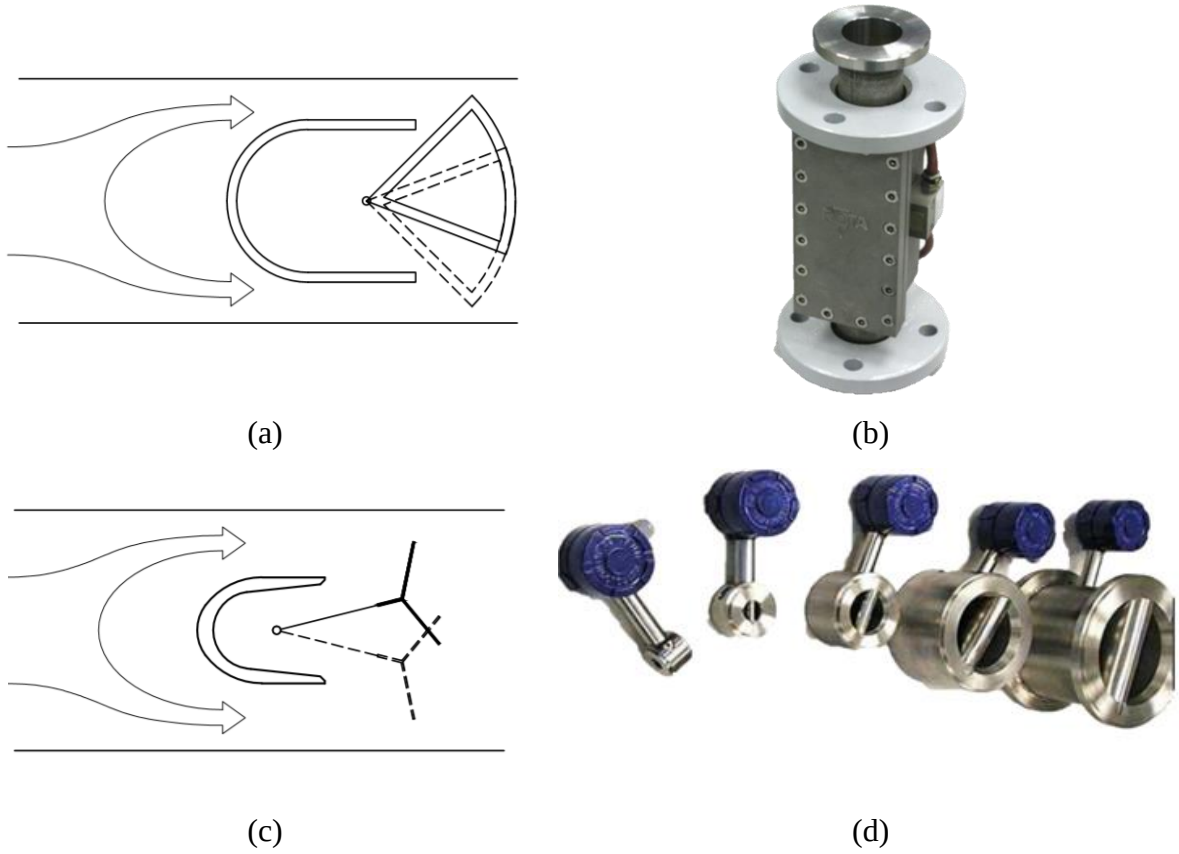

(a) (b)

(c) (d)

Figure 2.3: Designs with a stream divider: (a) hollow prism, figure adapted from (Heckle, 1973); (b) commercial version of the hollow prism design (Rota, 1976); (c) geometry optimized by Turkowski, figure adapted from (Turkowski, 2003b); (d) commercial version designed by (Turkowski, Strzałkowski and Dąbrowski, 2000).

The transition from a circular pipe shape to the rectangular cross-section and a wide oscillator were a source of significant pressure losses, which resulted in large value of a pressure loss coefficient $\xi = 2\Delta p / (\rho v^2) \approx 6,3$ for DN50, where Δp is a pressure difference, ρ is fluid density and v mean flow velocity. Theoretical analysis of the geometry of the oscillator conducted by (Turkowski, 2003b) has shown that further optimization was possible. An optimized oscillator (Figure 2.3c) had higher energy of oscillations and no longer required wall proximity. Therefore the oscillator could be narrower and a flowmeter body of a circular cross-section could have been introduced. The pressure loss coefficient was reduced down to 3,2 for DN50 flowmeter. Additionally, the body of the flowmeter was five times shorter and lighter, which was especially important for larger nominal diameters.

Such a design, described in (Gutkowski and Turkowski, 1985; Turkowski, 1987b, 1987c) and shown in Figure 2.3d, was manufactured serially for the diameter range DN15 – DN 200

and was used in many branches of industry for the measurement of hot and cold water, jet fuel, pre-treated wastewater, liquid sulfur, air, nitrogen, hydrogen, acetylene, oxygen, liquid oxygen, biogas and many others. MPEs did not exceed 0,5% for the rangeability of 10:1 after characteristics linearization. To detect oscillation frequency, a permanent magnet was attached to the oscillator. The magnet generated an alternating magnetic field that could be sensed by a coil, which was placed outside the flowmeter body.

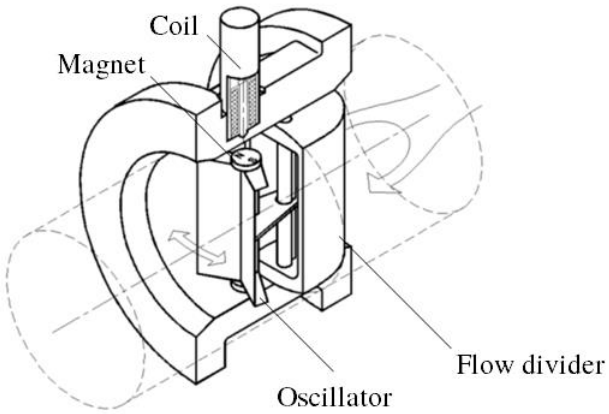

Figure 2.4: Measurement of oscillation frequency with the use of a coil and a magnet attached to the oscillator, figure adapted from (Turkowski, 2002).

The presented thesis focuses on this design, as it has shown the best metrological and operational properties from all the found variants and it has been validated in the industrial environment. What is more, the diameters and flow rate ranges covered by this design are commonly found in LNG applications. This translates to a huge research and application potential. The following chapter describes the principle of operation of the flowmeter and reviews available knowledge with the focus on the topics that require further study.

2.2 Analytical models

2.2.1. Principle of operation

In the case of the design under consideration, a stream divider splits the incoming fluid flowing in the pipe into two streams, which are guided past a pivotally mounted oscillator.

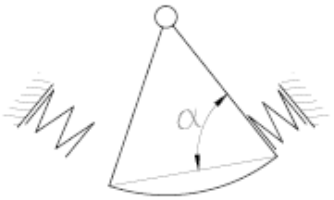

Figure 2.5: Analogy to a compound pendulum, figure adapted from (Heckle, 1973).

The two streams can be regarded as fluidic springs, which characteristics change with the flow rate (Figure 2.5). Following the analogy to a compound pendulum supported by springs, the angular frequency of the oscillator ω can be expressed with the equation (Heckle, 1971):

$$\omega = \sqrt{\frac{C_\varphi}{I}} \tag{2.1}$$

where C_φ is the angular spring stiffness and I is the moment of inertia of the oscillator. The formula describing angular stiffness of "fluidic springs" was developed by (Heckle, 1971) for the prismatic shape of the oscillator from the balance of forces, under assumptions that the flow in the channel of the stream divider is uniform, the flow is incompressible, two-dimensional, inviscid and stationary. In that case, the relationship between the oscillation frequency f and the volumetric flow rate q_v takes the form:

$$f = \frac{l_0 q_v}{2\pi A}\sqrt{\frac{\rho h \sin 2\alpha}{2I}} \tag{2.2}$$

where l_o is the level arm of the fluid force impinging on the oscillator, $A = hx$ is the area of the flow cross-section that impinges on the oscillator, h is the height of the oscillator, x is the width of the oscillator immersed in the fluid stream, ρ is the fluid density, α is the angle marked in Figure 2.5 and I is the moment of inertia of the oscillator.

The resultant relationship between oscillation frequency and volumetric flow rate is linear. Such simplified reasoning concerns the case of an undamped oscillator and does not explain why the flowmeter operates in a limit cycle. Because of numerous assumptions, neither does it allow predicting the calibration constant accurately.

2.2.2. Geometry optimization attempts

(Turkowski, 2003a) developed a model basing on the same assumptions, but for the shape of the oscillator as shown in Figure 2.3c. The development of the simplified model was followed by a geometry optimization attempt (Turkowski, 2003c). The optimization target function was the nondimensional stiffness *F*, calculated as:

$$F = \frac{\tau}{\rho w^2 xhs} \tag{2.3}$$

Where τ is the torque acting on the oscillator, *w* is the mean fluid velocity in the channel of the stream divider and *s* is the oscillator's width.

The nondimensional stiffness *F* depends on the oscillator's shape, therefore it allows comparing performance of various oscillator designs. Turkowski set the optimization goal of achieving maximal *F* value, which translates to maximal potential energy at the extreme angular positions.

In result, Turkowski proposed a shape of the oscillator as shown in Figure 2.3c, which was a compromise between maximal *F* value and current manufacturing capabilities.

Higher energy potentially increases the measurement range, resistance to external disturbances and resistance to bearing wear. However, this fact has not been verified. What is more, an incomplete description of flow parameters in the experimental study made a comparison with presented therein analytical model impossible. The theoretical analysis used for optimization bases on numerous assumptions, which impact and validity has not been studied.

2.2.3. Oscillator's dynamics

A thorough analysis is necessary to outline conditions and reasons for stable oscillations. Special care must be given to terms that introduce nonlinearities or phase shifts in equations describing the flowmeter operation. It is relatively simple for ball shapes, where extensive theoretical and experimental data allow describing phenomena that take place during oscillations of a ball immersed in a fluid accurately. In the studied case it is more challenging, nevertheless attempts to describe oscillator dynamics for shapes of a hollow prism (Figure 2.3a) and design by Turkowski (Figure 2.3c) have been made. Due to the complexity of the models their discussion in this chapter will be limited to short summaries.

(Heckle, 1971) explained the stable oscillations by the wall proximity effects, which occur both at the oscillator sides as well as at its top and bottom. He developed the equation describing the oscillator's dynamics with arbitrarily introduced nonlinear damping functions.

(Górecki and Kubas, 2005) presented a model describing the dynamics of a hollow prism oscillator, where nonlinear damping was related to the vortex shedding effects. Relative differences between oscillation frequency for the model and experiment were in the range of 20%.

(Turkowski, 2003a) developed a model where the phase shift between forces acting on the oscillator was the reason for the operation in a limit cycle.

The weak point of the published models is that in all the cases verification and validation were limited and results were presented for a single set of input parameters. Models utilize arbitrarily introduced constants with no guidelines on how to select them.

2.2.4. Summary

Accurate modelling is necessary for geometry optimization. It would also allow determining factors affecting the error curve and the overall performance. E.g. it is necessary to have an estimate of loads acting on the oscillator to properly select bearings.

Various mathematical models have been developed, but their possibilities have been exhausted. (Turkowski, 2003b) underlined the future role of Computational Fluid Dynamics (CFD) in the development of mechanical oscillator flowmeters. At the time, both commercial software and in-house codes for dynamic mesh applications were employed (Lavante, Humener and Schieber, 2001; Parry, 2001), but computing power was considered inadequate for practical problems. Therefore both an understanding of the operation and optimization of the designs were based on greatly simplified analytical models and an experimental approach. There is still room for improvement in that matter.

The next chapter will compare the mechanical oscillator flowmeter with the other flowmeter types and indicate other vital topics that require further study.

2.3 Comparison with other flowmeter types

Compared with flowmeters that are currently used for LNG measurement, in terms of durability mechanical oscillator flowmeters are worse than any flowmeter with no moving parts. Still, knife-edge bearings do not require lubrication and are more reliable than precision bearings of turbine flowmeters (Bek and Turkowski, 1987). There is little published data on robustness of

mechanical oscillator flowmeters (Turkowski, 1988; Strzałkowski, Gutkowski and Turkowski, 1989) and durability studies are necessary.

MPEs do not exceed 0,5% for rangeability of 10:1 after characteristics linearization (Turkowski, 2002), which is worse than turbine flowmeters and better than orifice flowmeters, but most importantly it suffices to meet legal provisions for LNG measurement. Overall measurement uncertainty is similar to vortex flowmeters, which is better than orifice flowmeters, but worse than the turbine or Coriolis flowmeters. However, published data concerning the performance of mechanical oscillator flowmeters only concerns water, air and liquid sulphur. There are no records of experiments in cryogenic conditions. The question is whether the repeatability and linearity of the meter are maintained in such a scenario.

A typical error curve of a mechanical oscillator flowmeter is shown in Figure 2.6. Three regions are marked. In the 1st part, for higher Reynolds number, the Strouhal number and the meter coefficient is relatively constant. In the earlier studies it was suspected that the hump in the 2nd zone is related to Reynolds number and in the presented thesis it will be proven. As a follow-up, a method of improving the error curve linearity will be presented. The drop in the 3rd part is a result of bearing friction forces which start to dominate.

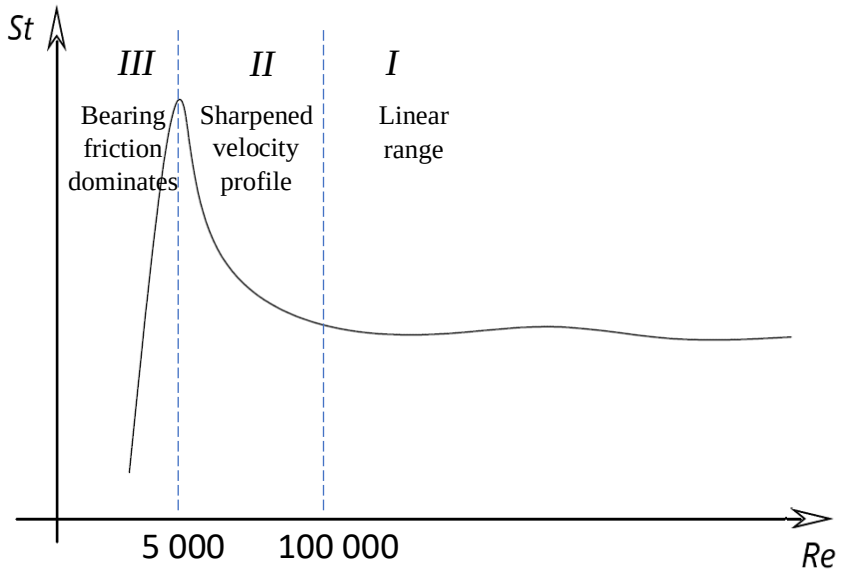

Figure 2.6: Typical error curve for a mechanical oscillator flowmeter, Strouhal number vs Reynolds number.

In comparison with their closest relative, vortex flowmeters, mechanical oscillator flowmeters have a wider measuring range (Turkowski, 2018). In the case of vortex flowmeters,

a stationary bluff body causes the formation of a vortex street. Below Reynolds number of 20 000 vortex shedding is irregular and the output becomes nonlinear. The vortex shedding ceases when Reynolds number falls below 5 000, whereas mechanical oscillator flowmeters operate even at Reynolds numbers of 2 500.

In the case of vortex flowmeter, a pressure signal generated by a vortex street is weak, it requires sophisticated methods of signal conditioning (Takahashi and Itoh, 1993; Johnson, 2001) and it results in increased susceptibility to pipe vibrations, e.g. generated by pumps (Miau, Hu and Chou, 2000). Mechanical oscillator flowmeters are vibration-resistant owing to the large amplitude of the oscillator's motion. The output signal is strong, regular, and simple to process.

Moving to the influence of the fluid properties on the measurement. As shown in eq. (2.2), the frequency of oscillations depends on the density of the measured fluid. Similar to differential pressure flowmeter types (International Organization for Standardization, 2003a, 2003b, 2003c, 2003d), without knowing the fluid density no measurement can be done. This is in contrast to vortex or ultrasonic flowmeters.

Correction factors for density and temperature are another issue. If the flowmeter measures fluid of different density and temperature than the fluid that was used for calibration, then correction factors need to be introduced to properly determine calibration constant. Appropriate equations were proposed by (Turkowski, 2004), but their verification is necessary. Existing studies are limited to water and liquid sulphur. It is unknown whether the equations are still valid in cryogenic temperatures.

Finally, the specification of the flowmeter concerns not only its performance at any flow rate but also at any environmental conditions within the limits of the specification (International Organization for Standardization, 1998). That is why to broaden the application range of mechanical oscillator flowmeters, there should be data that describe the influence of flow pulsation, inlet profile disturbances and pipe surface roughness on the measurement performance. Currently our knowledge in this topic is limited and a further study is necessary.

Chapter 3

Objective of the work

A conclusion drawn from the conducted literature review is that mechanical oscillator flowmeters, due to their metrological and operational properties, may find applications in new measurement scenarios, e.g. measurement of LNG or other cryogenic fluids. Before it could happen, a number of topics outlined in the previous chapter have to be researched. Detected white spots do not concern only the practical aspects, but also scientific details – the principle of operation and modelling.

The main objective of the thesis was to expand research on mechanical oscillator flowmeters to broaden their application range. Considering the state of the art, the following goals were set:

1. Assessment of capabilities of CFD modelling, evaluation of various turbulence models and dynamic mesh methods. No CFD model of a mechanical oscillator flowmeter has been presented in the past.
2. Determination of factors affecting the linearity of the error curve. Only preliminary studies on this issue exist.
3. Verification of the optimal shape of the oscillator and study on the influence of energy of oscillations on the metrological and operational parameters of the flowmeter. No such a study has been presented before.
4. Study of the influence of flow pulsation and inlet profile disturbances on flowmeter's performance. Existing studies require an extension.
5. Study of the influence of pipe surface roughness on measurement characteristics. No such a study has been conducted before.
6. Experimental study in cryogenic conditions and verification of equations describing the influence of fluid properties on the characteristics. Existing studies are limited to water and liquid sulphur.

The next chapter will cover the details of experimental setup and flowmeters that were selected for the study.

Chapter 4

Experimental setup

4.1 Selected flowmeters

Mechanical oscillator flowmeters come in many variants, which were presented in Chapter 2. This thesis focuses on the design proposed by (Turkowski, 2003b), as it shows promising metrological and operational properties and it has been proven in the industrial conditions.

Although the device has been manufactured for all the typical nominal diameters in the range of DN 15 – DN 200, only flowmeters of size DN 50 were selected for the study. This diameter is commonly used in the process of unloading of LNG tank trucks. Additionally, available air and water flow facilities fully covered its measurement range, as shown in Table 4.1 and Table 4.2.

Table 4.1: Measurement range of the studied DN 50 mechanical oscillator flowmeter, data from (Turkowski, 2002).

Fluid	Measurement range
water	(1 – 50) m^3/h
air T = 0°C, p = 1.013 bar	(30 – 600) m^3/h

Standard designs manufactured accordingly to specifications (Turkowski, 2002) were made of austenitic steel. Two copies were available for the study presented in this thesis. Additional prototypes designed for this work were made with a polyamide powder-based additive manufacturing technology Multi Jet Fusion (Figure 4.1). This allowed studying a greater number of designs experimentally, although the durability of polyamide effectively limited the application range to air. The mass properties of oscillators had to be determined for modelling purposes. The geometry of oscillators was recreated in CAD software, which allowed calculating moments of inertia. Density was measured with a precise scale, by comparison of the oscillator's weight in air and water (Figure 4.2).

Figure 4.1: Some of the flowmeter parts prepared for the study.

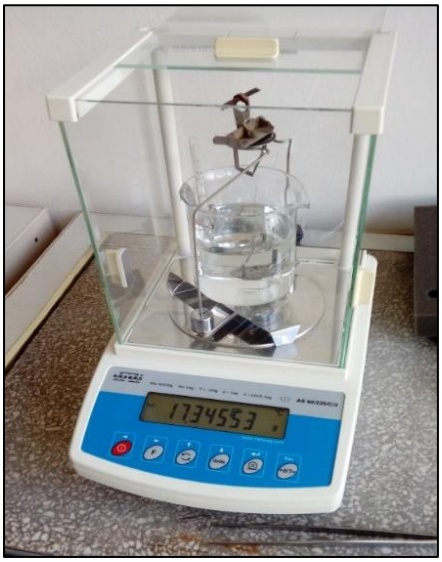

Figure 4.2: Measurement of oscillator's density.

In the previous studies (Turkowski, 2003b), the frequency of oscillations was measured with the use of a coil, which picked up the movement of a magnet attached to the oscillator. To measure the flow rate, it was sufficient. In this study, the coil was replaced with a linear output Hall sensor. It allowed capturing not only frequency, but also the position of the oscillator in the function of time. This provided information on the amplitude of oscillations. Alternative methods of oscillation frequency measurement, besides a coil and a Hall sensor, have also been studied (Figure 4.3). Turbine flowmeters typically use inductive proximity sensors. It was found that in the case of a mechanical oscillator flowmeter they may be applied as well, no differences between frequencies measured by coil and inductive sensor were observed. The other studied

option was a fast piezoelectric pressure sensor placed 1,5*D* downstream of the oscillator. The pressure sensor captured the vortices that were shed behind the oscillator. It showed double the frequency of the coil, as two vortices were swept each oscillation cycle. The relative difference between frequencies measured with coil and pressure sensor was in the range of 0,1% (Figure 4.4).

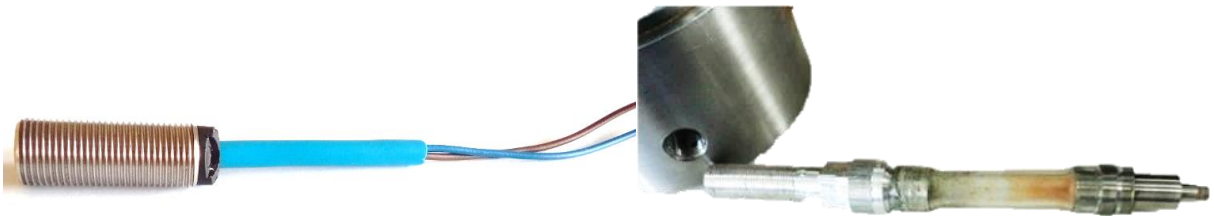

Figure 4.3: Sensors that may be used to measure oscillation frequency, left – Turck Bi3-EG12 inductive proximity sensor, right – fast piezoelectric pressure sensor PCB Piezotronics 106B with a mounting tube.

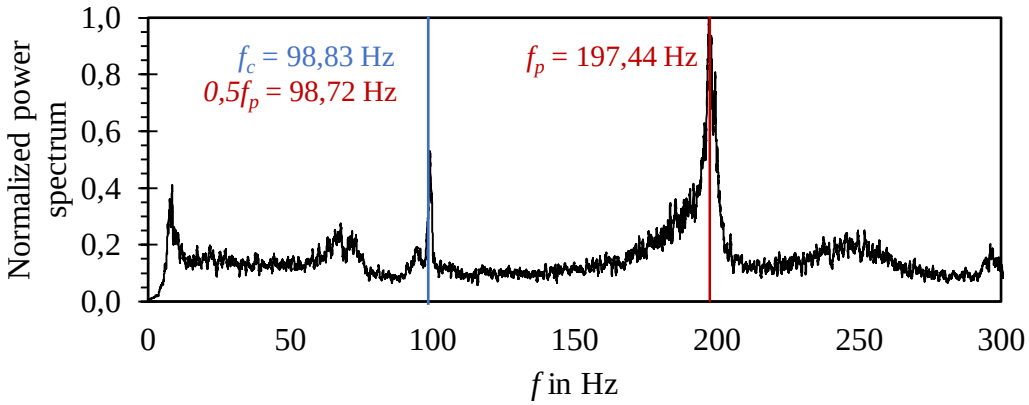

Figure 4.4: Power spectrum obtained by a fast pressure sensor on a water calibration stand, f_p denotes the frequency measured with the pressure sensor and f_c denotes the frequency measured using the coil.

The above findings may extend the application range of the mechanical oscillator flowmeter. Pressure sensor or inductive sensor could be applied as redundancy. These measurement methods do not require a magnet, so they could also find applications in cases were the magnet material would not be compatible with the measured fluid.

Experimental studies were conducted to determine the relationship between the flow rate and the frequency of oscillations. The number of pulses per unit volume or unit mass is referred to as a calibration constant or a *K*-factor. Plots of relative error *E* between the measured and the

reference *K*-factors in the function of flow rate specify the error curve. Error curves were determined using air, water, liquid nitrogen and liquefied natural gas calibration stands.

$$E = \frac{K - K_{ref}}{K_{ref}} \tag{4.1}$$

All of the test stands mentioned in Table 4.2 together with the auxiliary equipment (pressure and temperature transmitters) were approved by the Polish Central Office of Measures and were traceable to the national standards. Uncertainty budgets were calculated accordingly to guidelines specified in (Joint Committee for Guides in Metrology, 2008; European Accreditation Laboratory Committee, 2013) and are presented in the Appendix.

Table 4.2: Details of flow facilities.

Test stand	**Flow rate range for DN 50 unit under test**	**Expanded uncertainty for $k = 2$**
water calibration facility	(0,5 – 48) m^3/h	$U_{95}(V) = 0{,}05\%$
low-pressure air facility	(20 – 300) m^3/h near atmospheric pressure	$U_{95}(V) = 0{,}25\%$
bell prover	(0,04 – 45) m^3/h near atmospheric pressure	$U_{95}(V) = 0{,}17\%$
calibration with liquid nitrogen	(3 – 50) t/h	$U_{95}(m) = 0{,}4\%$
calibration with LNG	(3 – 50) t/h	$U_{95}(m) = 0{,}4\%$

The next part of the thesis c

overs the details of the calibration stands. Those described in subchapters 4.2-4.4 were already present in the laboratory. The author of the thesis had to select and install auxiliary equipment and install proper piping configurations.

4.2. Water calibration facility

Reference volume of water *V* was measured statically with tanks of 1 m^3 and 0,25 m^3 capacity. A gravity flow system was utilized to enhance flow stability and eliminate pulsations generated

by pumps. View of the stand is presented in Figure 4.5 and a detailed diagram is shown in Figure 4.6.

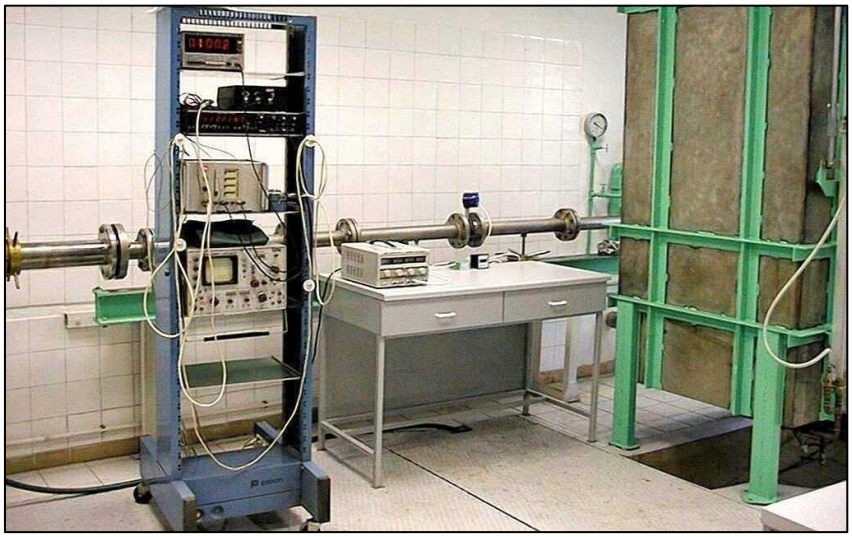

Figure 4.5: Water calibration stand with an installed mechanical oscillator flowmeter.

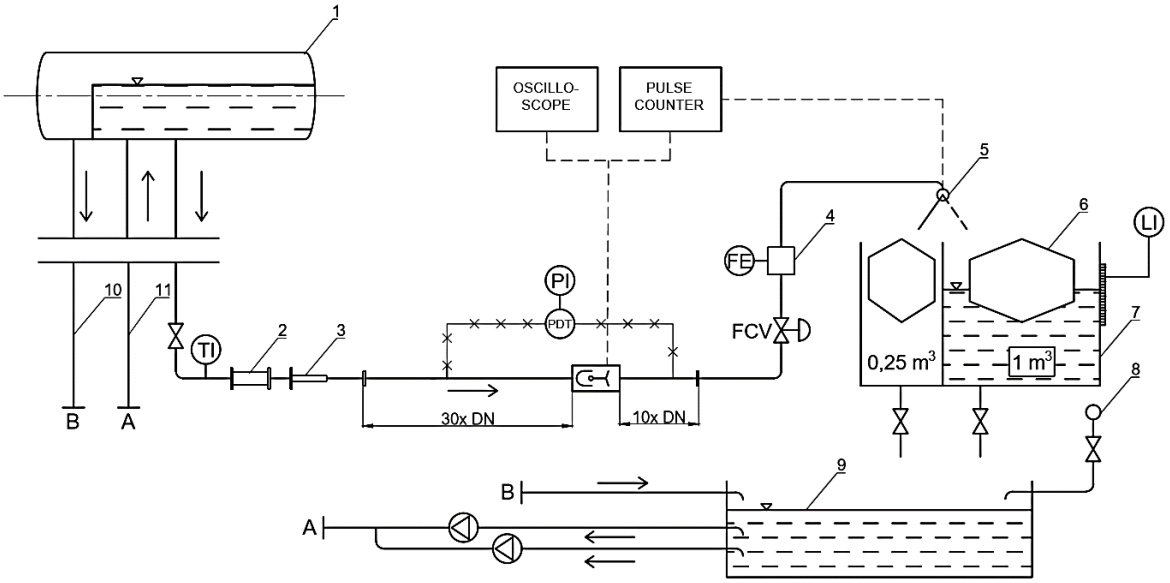

Figure 4.6: Water calibration stand diagram, 1 – water supply reservoir, 2 – in-line sight glass, 3 – telescopic compensator, 4 – electromagnetic flowmeter, 5 – flow diverter, 6 – fixed buoys that increase resolution of level measurement, 7 – measurement tanks, 8 – mains, 9 – storage tank, 10 – overflow pipe, 11 – discharge line, TI – temperature indicator, PDT – pressure difference transmitter, PI - pressure indicator, FCV – flow control valve, FE – flow element, LI – level indicator. Dashed lines denote electrical connections. X-hatched lines denote pressure signal connections.

As the mechanical oscillator flowmeter generates pulse output on the principle of its operation, it was possible to utilize a flying start and finish method (Strzelczyk and Gosk, 2010). In this method, flow through the meter continues uninterrupted and fast, electromagnetically driven diverter switches the flow between tanks. The pulse counter of the flowmeter was synchronized with the diverter. Therefore volume measured with tanks could have been compared with the number of pulses generated by the oscillator. Precise time t measurement was also synchronized with the diverter, which enabled calculating the volumetric flow rate q_v.

$$q_v = \frac{V}{t} \tag{4.2}$$

Measurement of water temperature allowed determining its density and calculating the mass flow rate.

4.3. Low-pressure air facility

The flow of air was forced by a suction blower. The temperature of the inflowing air was stabilized by an air-conditioning system. Depending on the flow rate, either a DN 50, DN 100, DN 150 or DN 300 Instromet SM-RI-X turbine gas meter was installed in series with the flowmeter under test and was used as a reference (Figure 4.7, Figure 4.8).

Figure 4.7: Low-pressure air facility.

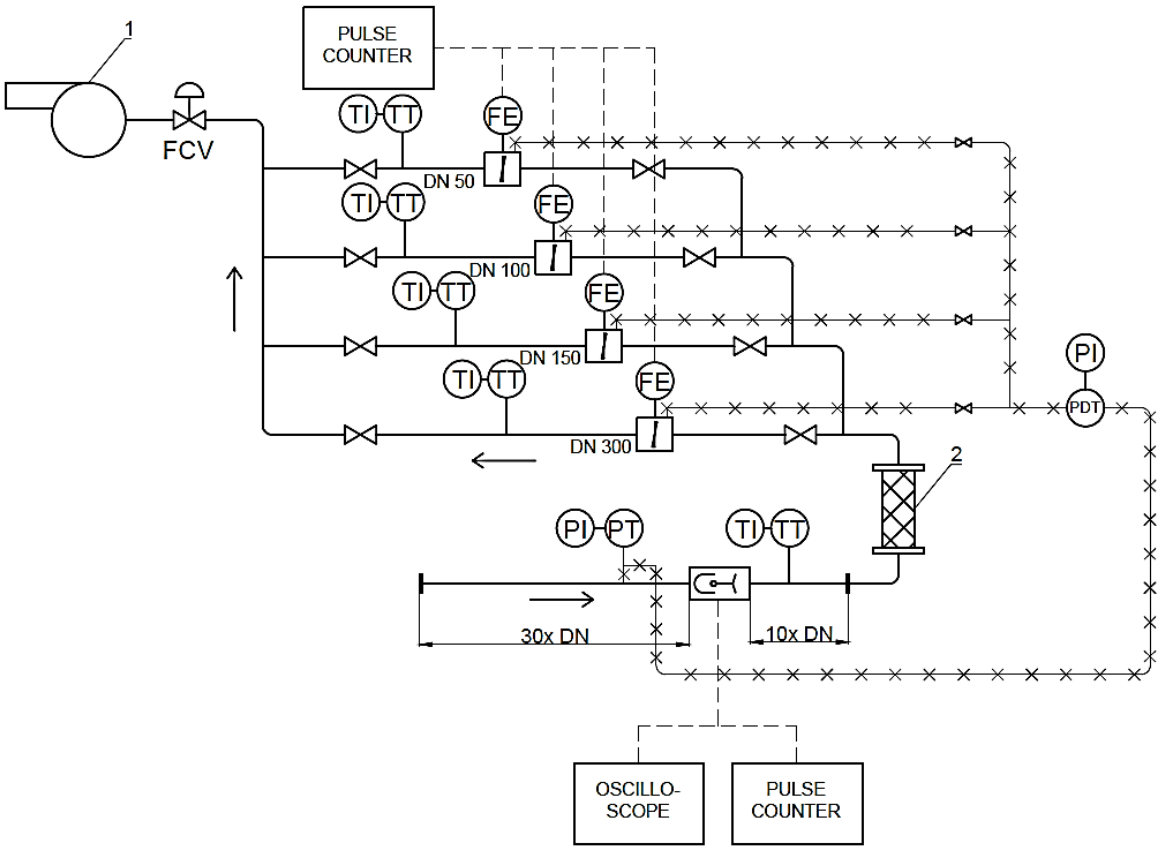

Figure 4.8: Low-pressure air calibration stand diagram, 1 – suction blower, 2 – inline filter, TI – temperature indicator, TT – temperature transmitter, PDT – pressure difference transmitter, PI – pressure indicator, FCV – flow control valve, FE – flow element (turbine flowmeter). Dashed lines denote electrical connections. X-hatched lines denote pressure signal connections.

Reference volume flow rate was calculated as:

$$q_{v,t} = \frac{n}{t \cdot K_t} \tag{4.3}$$

where n is the number of pulses generated by turbine gas meter in time t and K_t is K-factor of the turbine gas meter in pulses/m^3. To relate this value to the volumetric flow rate in conditions at the location of the unit under test, temperatures T and pressures p were measured:

$$q_{v,m} = q_{v,t} \cdot \frac{(p_u - \Delta p)T_u}{p_u T_t} \tag{4.4}$$

where subscript *t* denotes turbine gas meter and subscript *u* denotes unit under test. The density of air was calculated basing on the atmospheric pressure, temperature and humidity.

Measurement of time between flowmeters was synchronized by the operator. The time of measurement was long enough to mitigate the imperfect synchronization of pulse counters.

4.4. Bell prover

Bell prover calibration stand (Figure 4.9) is described in Chapter 8.2.2.

Figure 4.9: Bell prover calibration stand.

4.5. Calibration with liquid nitrogen and liquefied natural gas

Both calibration stands are described in Chapter 9.1.2.

Chapter 5

Development of a numerical model

5.1 Introduction

Test stands described in the previous chapter allowed collecting data that would be used for validation of the developed model of the flowmeter. The model presented in this thesis was formulated with the use of Computational Fluid Dynamics (CFD).

The development of CFD is providing a tool for analyzing flowmeter behavior to an increasing extent. It presents a great supplement to experimental study, as it allows visualizing pressure and velocity fields in detail. What is more, fluid parameters may be freely set and off-design performance may be verified. Numerous works on similar designs, such as the vortex flowmeter, have proven that CFD analysis is a viable method of design exploration (Lavante *et al.*, 1999; Jan and Sheu, 2004; Kabaciński, Pospolita and Zamorowski, 2007; Safinowski, Szudarek and Szewczyk, 2017). In the case of the mechanical oscillator flowmeter, the situation is more complex, as it involves coupling of fluid flow with the movement of an oscillator. Because no CFD model of a mechanical oscillator flowmeter has been presented in the past, it was necessary to establish verification and validation of the numerical model.

The model was developed with a CFD code ANSYS Fluent, in which incompressible Reynolds-Averaged Navier-Stokes (RANS) equations (Reynolds, 1895) were solved using a finite-volume method. Using the Einstein summation convention, the continuity equation takes the form of:

$$\frac{\partial \overline{v}_i}{\partial x_i} = 0 \tag{5.1}$$

and the momentum conservation can be written as:

$$\rho\left(\frac{\partial \overline{v}_i}{\partial t} + \overline{v}_j \frac{\partial \overline{v}_i}{\partial \overline{v}_j}\right) = \rho a_i + \frac{\partial}{\partial x_j}\left[-\overline{p}\delta_{ij} + \mu\left(\frac{\partial \overline{v}_i}{\partial x_j} + \frac{\partial \overline{v}_j}{\partial x_i}\right) - \rho\overline{v'_i v'_j}\right] \tag{5.2}$$

where v_i represents the i-th component of velocity at a point x_i in space, ρ is the fluid density, a_i is the body force (e.g. gravity), p represents the static pressure, μ is the dynamic viscosity, δ_{ij} is

the Kronecker delta, bars denote time-averaged values and apostrophes represent instantaneous values. Because of the averaging process of Navier-Stokes equations, a Reynolds stress tensor $-\rho\overline{v'_i v'_j}$ was introduced. The closure problem arises and additional equations are needed. They are supplemented by turbulence models, which can be roughly categorized in two basic groups: models that solve transport equations for Reynolds stress tensor components and models that follow the Boussinesq hypothesis and introduce turbulent viscosity. Turbulence models selected for this work belong to the latter group, because they are more numerically robust and there is no evidence that they would be less accurate in the studied case. They follow an assumption that the Reynolds stress tensor is proportional to the mean strain rate tensor:

$$-\rho\overline{v'_i v'_j} = \mu_t\left(\frac{\partial\overline{v}_i}{\partial x_j}+\frac{\partial\overline{v}_j}{\partial x_i}\right) \tag{5.3}$$

where μ_t is the turbulent viscosity.

Turbulence modelling is a significant problem and turbulence models that became industry standard due to their low computational cost have limited applicability. For instance, RANS turbulence models simulate all scales of turbulence and resolve none. Their application range concerns cases which do not require explicit resolution of turbulent structures. Furthermore, the shortcoming of RANS turbulence models basing on turbulent viscosity is that they fail to predict strongly rotating flows, strongly decelerated flows or curvature effects. Nevertheless, they were validated in similar applications on the example of vortex flowmeters (Wahed, Johnson and Sproston, 1993; Ozgoren *et al.*, 2015). Even if turbulence models are narrowed down to RANS models basing on eddy viscosity, there are multiple variants which perform differently in various scenarios. For that reason a comparison between different turbulent models for a particular task is usually performed. Following RANS turbulence models were used in the study: Spalart-Allmaras (Spalart and Allmaras, 1992)**,** realizable *k-ε* with Enhanced Wall Treatment (Shih *et al.*, 1995) and *k-ω* SST (Menter, 1994)**.**

CFD simulations are subject to errors and uncertainty. According to (AIAA, 1998), uncertainty is related to user inputs (incomplete information on material properties, boundary conditions, geometry) and physical models (negligence or simplification of turbulence, compressibility, unsteadiness). Errors are introduced by deficiencies not caused by lack of knowledge, i.e. discretization errors, iterative convergence errors and roundoff errors. Numerical errors were estimated, and a comparison with experimental data has shown that

accurate results may be achieved at a reasonable cost. Computations were performed on a high-performance cluster Cray XC40 Okeanos thanks to the support of Interdisciplinary Centre for Mathematical and Computational Modelling at University of Warsaw through grant GB74-0.

5.2 Geometry and boundary conditions

The starting point geometry was the shape of the oscillator developed by (Turkowski, 2003b). Parameters describing the oscillator's geometry are recalled in Figure 5.1 and their values are collected in Table 5.1.

Table 5.1: Baseline oscillator details.

Geometry							**Mass properties**		
D	***s/D***	***α***	***γ***	***b/D***	***z/D***	***h/D***	**material**	**mass *m***	**moment of inertia I_o**
50 mm	43,3%	10°	70,1°	15%	20%	78%	austenitic steel	17,352 g	$1{,}06 \cdot 10^{-5}$ kg·m^2

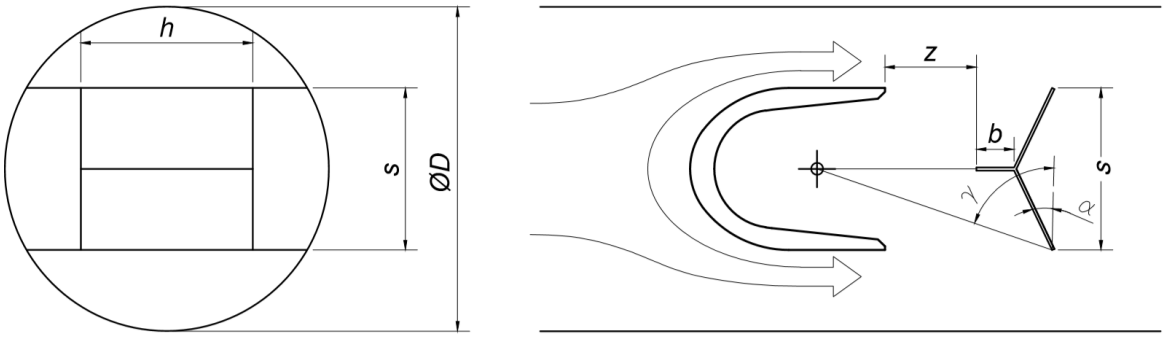

Figure 5.1: Parameters describing the oscillator's shape.

Both a three-dimensional and a two-dimensional planar model have been developed. Although the two-dimensional model cannot capture three-dimensional flow structures, it provides a first-order estimate of the system behavior in a fraction of the time required for a three-dimensional simulation.

The developed two-dimensional model corresponds to the cross-section of a real geometry in the symmetry plane. As depicted in Figure 5.2, minor changes to the geometry must have been introduced. The support has been deleted. It would form an obstacle for incoming fluid that does not exist in real geometry. As such, it would bias the flow pattern and introduce damping in transient simulations. Moreover, the contact point between a stationary knife and a

moving pan would pose a significant meshing difficulty. For that reason, the geometry of the bearing has been simplified to a cylinder that follows the rotation of the oscillator's body.

A three-dimensional model has been developed as well. To reduce its extent, a mirror symmetry has been assumed and only half of the geometry was used. The applied symmetry boundary condition assumes a zero flux (both convective and diffusive) of all quantities across a boundary. It has been verified by comparison with a complete model that introducing symmetry does not noticeably affect the quantities of interest such as torque acting on the oscillator. Just like in the case of the two-dimensional model, the bearing geometry has been reduced to a cylinder. Flow structures near the knife-edge bearing do not bring significant contribution to the torque, therefore this simplification was justified. The rest of the geometry has been left intact.

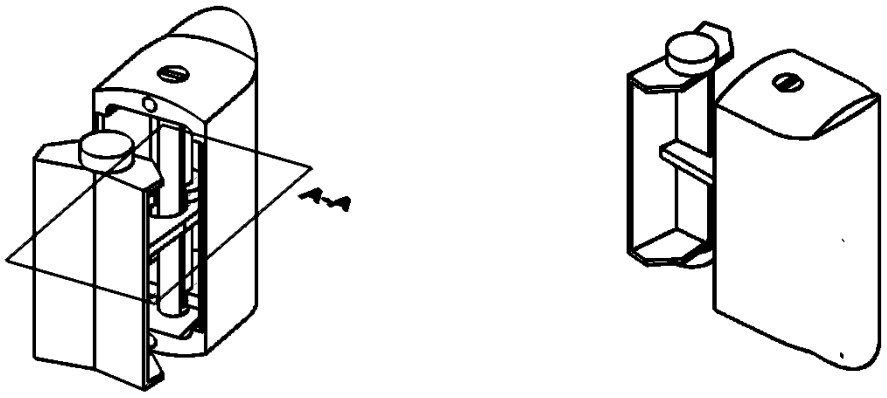

(a)

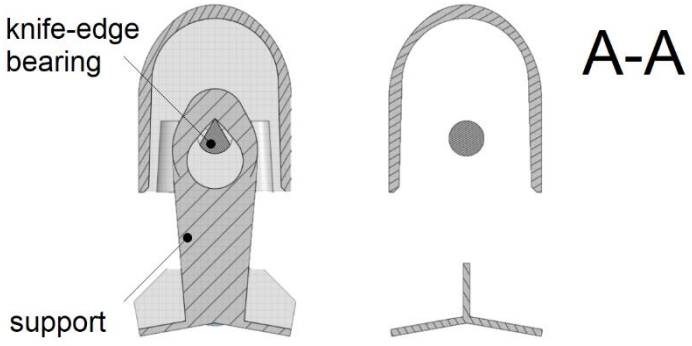

(b)

Figure 5.2: (a) Real geometry, isometric views; (b) comparison of the real geometry in the *A*-*A* symmetry plane and the geometry of a 2D model.

Inlet boundary conditions were in the form of fully-developed profiles of velocity and variables required for turbulence modelling. Required profiles were obtained in separate

simulations of a pipe of an infinite length, which was modelled by a translational periodicity boundary condition.

Figure 5.3 presents all of the applied boundary conditions, i.e. prescribed velocity and turbulence quantities at the inlet, zero gauge pressure at the outlet, no-slip condition at walls and zero normal flux at the symmetry plane. Constant fluid density and viscosity were assumed.

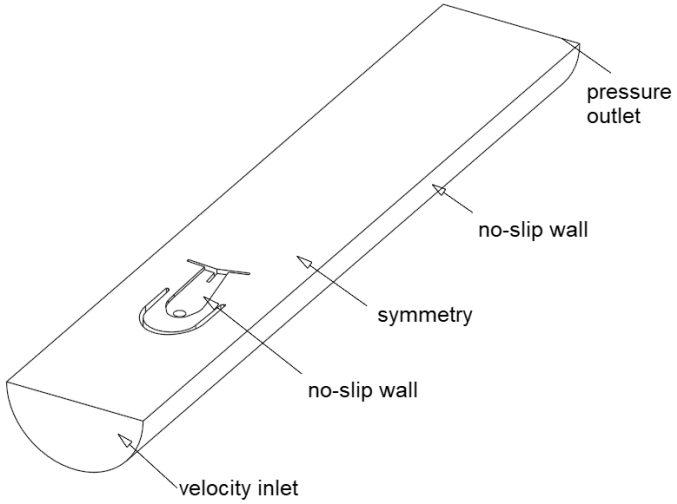

Figure 5.3: Boundary conditions for the three-dimensional case.

The minimal size of the domain which does not affect the frequency and amplitude of oscillations was found. The influence of domain size downstream the flowmeter on oscillator frequency is given in Table 5.2.

Table 5.2: Study of the required length of a straight outlet run

Domain size downstream in nominal diameters	**Shift in frequency related to the largest domain**
0,5	1,60%
1	-0,13%
2	0,06%
3	0,00%
6	reference

As shown, the outlet pipe length of three nominal diameters is sufficient. With the exact same procedure, a minimal required inlet pipe length was determined as 0,8*D*.

5.3 Meshing strategy and solver settings

5.3.1. Static mesh

For steady-state 2D cases with an immobilized oscillator, an unstructured quadrilateral mesh has been applied (Figure 5.4). In the case of 3D simulations, inlet and outlet segments of the domain were meshed with swept hexahedral cells. Polyhedral cells were generated near the components of the flowmeter (Figure 5.5). Sizing functions have been defined in the proximity of the oscillator and near the rear edge of the stream divider.

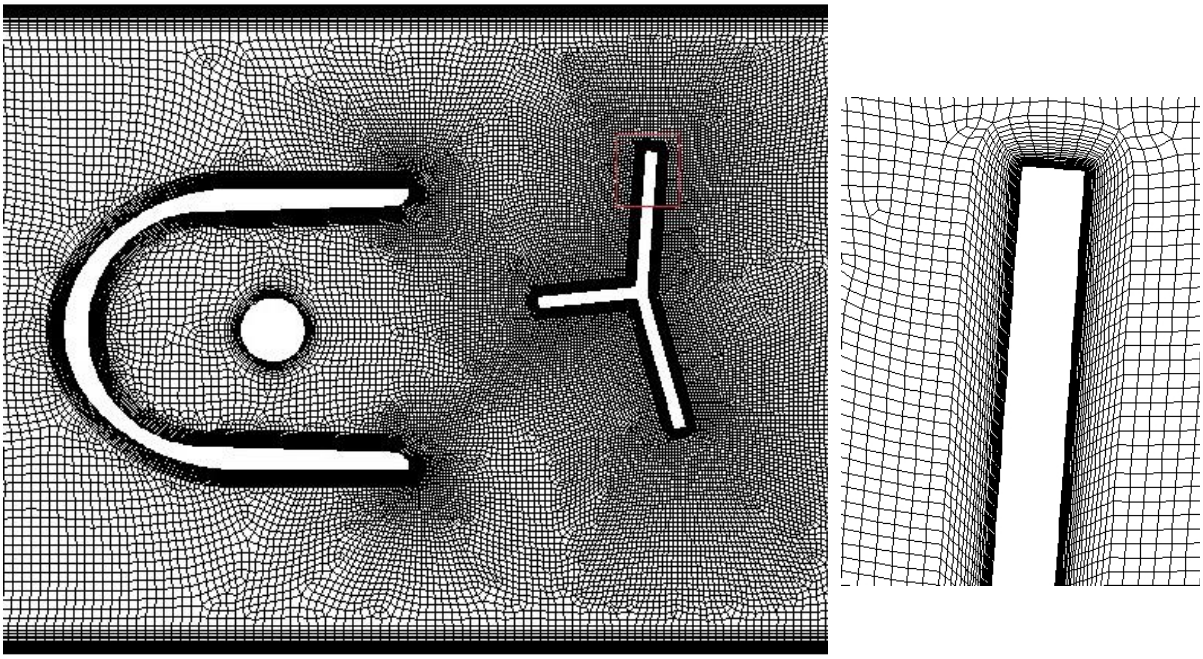

(a) (b)

Figure 5.4: (a) Two-dimensional mesh in the proximity of the oscillator; (b) inflation layer on the oscillator's surface.

The quantity of interest was usually the torque acting on the oscillator. To compute the torque accurately, the viscous sublayer had to be resolved. The first layer thickness was adjusted depending on the boundary conditions to achieve dimensionless wall distance y^+ below 1 at the walls of the stream divider and oscillator. This meant that the first mesh element was placed in the viscous sublayer. The rest of the boundary layer mesh consisted of 15 – 30 prism elements with a growth rate not higher than 1,15.

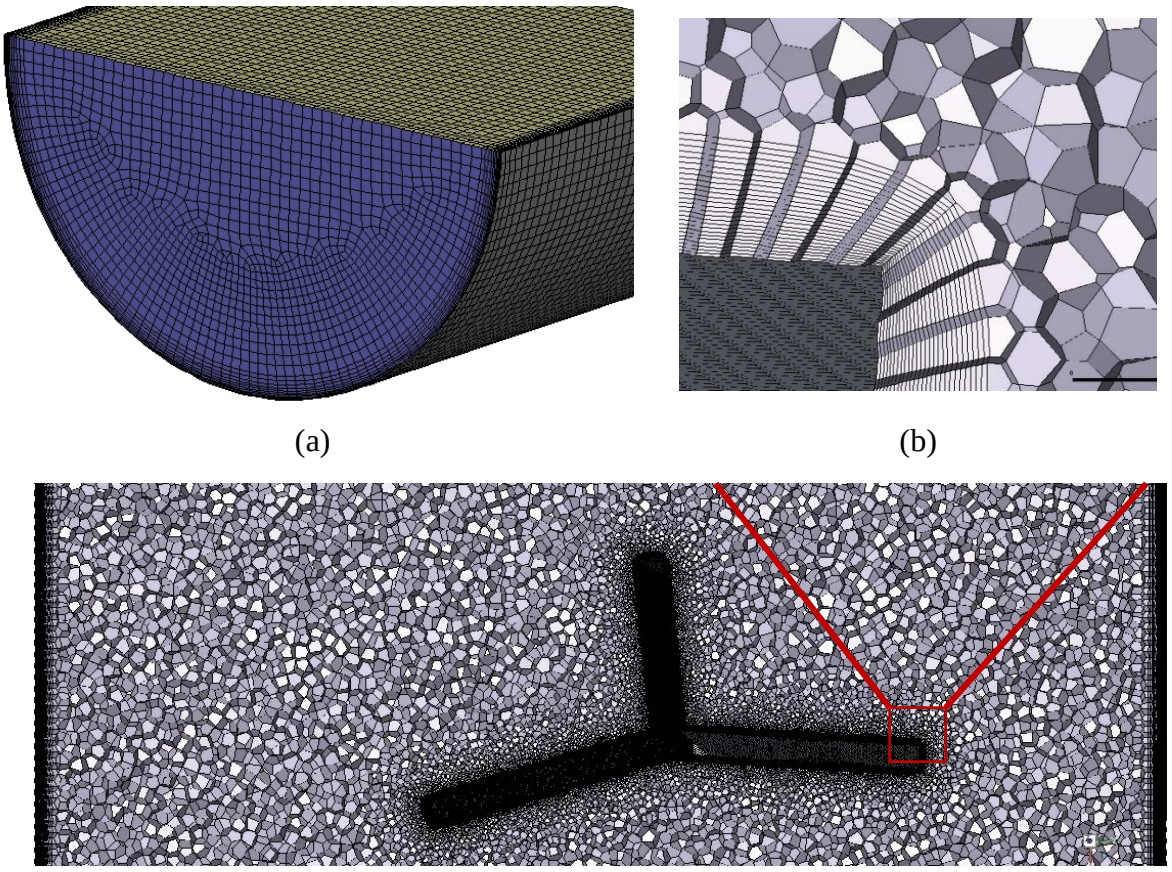

(a) (b)

(c)

Figure 5.5: Three-dimensional computational grid. (a) Inlet of the domain; (b) inflation layer on the oscillator's surface; (c) the proximity of the oscillator, view of cross-section below the support.

For all the studied cases normalized mesh quality parameters were monitored. Mesh skewness did not exceed 0,9 and the orthogonal quality was above 0,1, which means a very good quality of meshes.

5.3.2. Dynamic mesh

Besides steady-state simulations, a considerable number of transient simulations with fluid-structure interaction have been conducted. In each time step, the torque acting on the oscillator was used to compute the angular motion. Then, the computational mesh had to be adjusted to its new position. Various dynamic mesh methods were available:

Smoothing and remeshing – computational mesh stretches or shrinks in a spring-like manner. If the deformation causes a decrease of mesh quality below acceptable levels, local remeshing

is activated. The main disadvantages are variable mesh quality and a tedious procedure of setting the right method parameters.

Layering – computational mesh collapses or is being generated layer by layer. This method is the fastest and it is advantageous because of mesh quality, but the requirement of a hexahedral grid limits applications to simple geometries and motions (pure rotation, pure translation).

Overset mesh (Steger, Dougherty and Benek, 1983) – multiple grids, related to background and moving component, are superimposed on each other. Overset interfaces connect fluid zones by interpolating cell data in the overlapping regions. The advantage is that a moving body mesh and a background mesh can be generated independently, with higher quality and fewer constraints than if the system was meshed as a whole. However, the interpolation between grids is not conservative, so results should be examined carefully. What is more, there was no support for the 2nd order time discretization for dynamic overset mesh at the time of writing this thesis, which required smaller time-step and finer mesh size to maintain accuracy.

For the 2D model, the geometry was simple enough to apply the layering method. Structured zones of the mesh could have been isolated (Figure 5.6). Cell zones in the proximity of the oscillator and the pan are rotating rigidly with them.

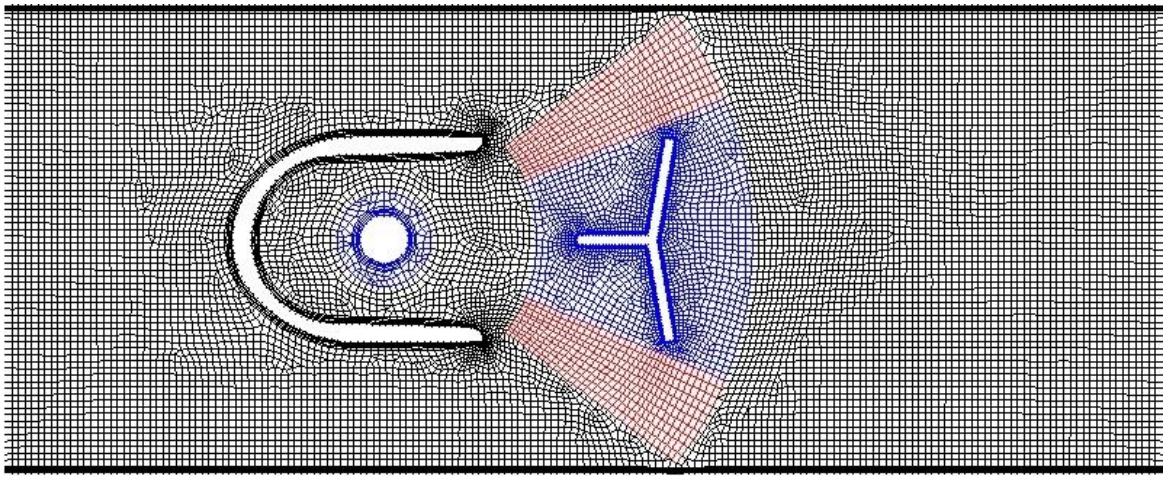

Figure 5.6: Two-dimensional mesh for the layering method: black – stationary zone; red – layering zone; blue – rigid zone.

The angular extent of layering zones limits the maximum angular position of the oscillator. It was not an issue in two dimensions, but in the case of 3D model the walls in the extreme position of the oscillator were too close to each other to isolate structured zones of the mesh while maintaining a reasonable boundary layer. The problematic distance is marked by Δx in Figure 5.7. Therefore in the 3D case, the choice was between remeshing and overset mesh.

Remeshing requires tetrahedral cell elements, which are usually less efficient than polyhedral, therefore the overset method was chosen.

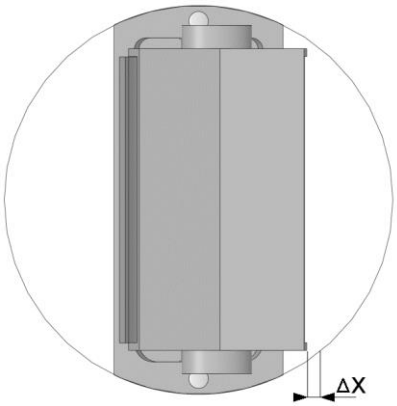

Figure 5.7: The problematic spot in the 3D model which prevents the application of the layering method.

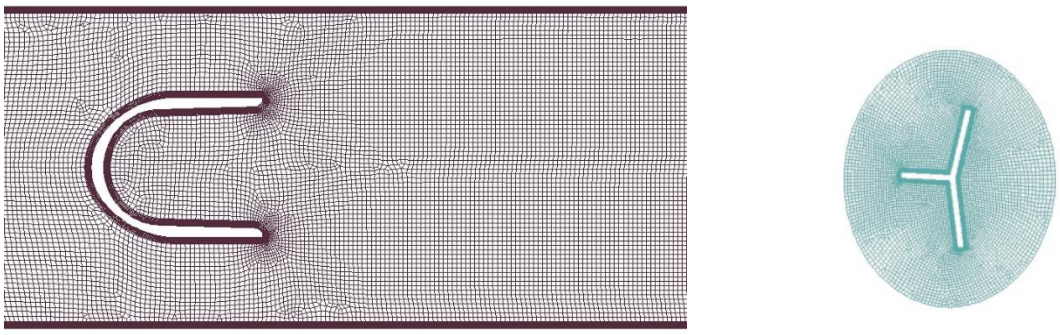

(a) (b)

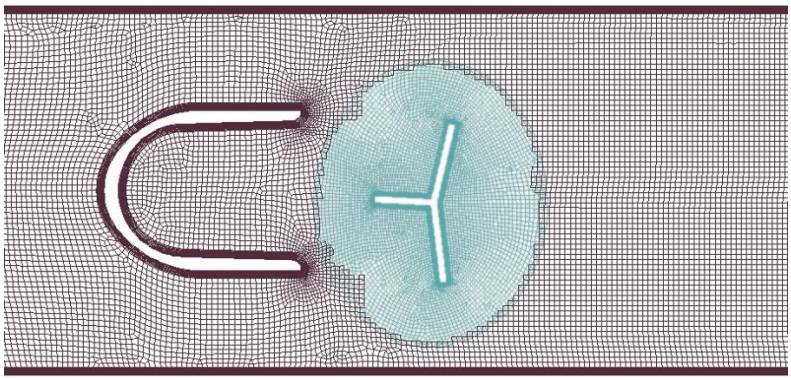

(c)

Figure 5.8: Two-dimensional mesh for the overset method (a) background mesh (b) component mesh, which moves as a rigid body with the oscillator (c) superimposed grids, an overlapping interface between grids is visible.

To verify the overset approach, a comparison between overset and layering methods has been done for 2D. The idea of the overset mesh method in this application is shown in Figure 5.8. After the verification that the overset method yields accurate results, all the dynamic mesh cases for the three-dimensional geometry were calculated with the use of the overset approach.

5.3.3. Solver settings and convergence criteria

Pressure-based solver, implicit formulation and Green-Gauss Node-Based option for calculation of gradients were chosen for all the studied cases, except for overset mesh simulations, which supported only cell-based methods for gradients evaluation. The coupled pseudo-transient scheme was applied for pressure-velocity coupling. Second-order spatial discretization for pressure, momentum, turbulent kinetic energy and turbulent dissipation rate was set.

The torque acting on the oscillator was the monitored value throughout the iterative calculation process. Iterative calculations were run until iteration convergence error was at least one order of magnitude smaller than the discretization error. This corresponded to normalized residual levels in the range of ($1 \cdot 10^{-5}$ – $5 \cdot 10^{-4}$). Iteration error was estimated according to (Ferziger and Peric, 1996) as:

$$E_{iter}^{n} \cong \frac{{C_M}^{n+1} - {C_M}^{n}}{\lambda_i - 1} \tag{5.4}$$

where n is the iteration number, C_M is the moment coefficient about the rotation axis and λ_i is approximated as:

$$\lambda_i \cong \frac{\left|{C_M}^{n+1} - {C_M}^{n}\right|}{\left|{C_M}^{n} - {C_M}^{n-1}\right|} \tag{5.5}$$

5.4 Grid independence test

The aim of the study presented in this subchapter was to assess grid sensitivity. The study was conducted in steady-state, both for 2D and 3D cases. Representative cell size h has been defined as the local cell size in the proximity of the oscillator. Multiple gradually refined meshes with refinement factor $h_{coarse} / h_{fine} = 1{,}3$ and with the same topology were studied. The summary of the studied cases is given in Table 5.3.

Table 5.3: Mesh independence study details.

Grid number	Representative cell size in mm	Element count ·10³ 2D model	Element count ·10³ 3D model
G1	1,2	-	3 841
G2	0,9	33	5 942
G3	0,7	47	8 032
G4	0,5	80	11 272
G5	0,4	116	-

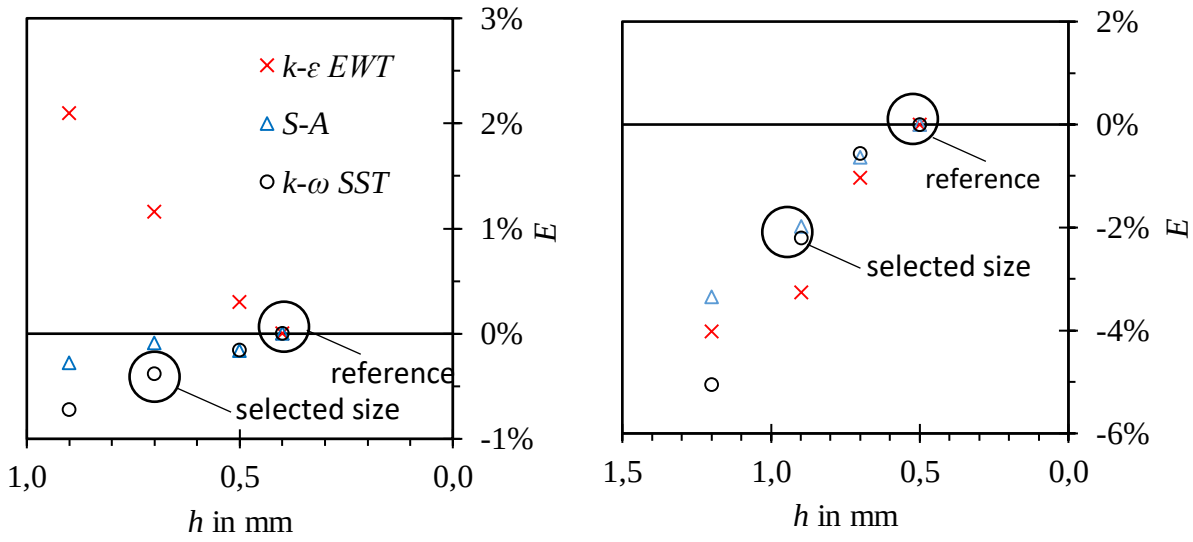

Figure 5.9: Steady-state grid independence test, relative differences between moment coefficient for given mesh size and the reference mesh. (a) Two-dimensional model; (b) three-dimensional model. Grid sizes used for reference and for future calculations are marked.

The results of the grid sensitivity test are shown in Figure 5.9. In two dimensions the *k-ε* turbulence model turned out to be the most sensitive to the grid size. It was expected that it would perform worse than *k-ω*, as the *k-ε* model is not dedicated to applications where y^+ is below 1. S-A model performs well, especially considering the fact that it is a one-equation model, in contrast to *k-ε* and *k- ω* which are two-equation models. In three dimensions all the turbulence models have a similar grid sensitivity. Considering the number of simulations that had to be conducted, the G3 grid was selected for two-dimensional cases and the G2 grid was

selected for three-dimensional cases, as a compromise between computational effort and solution accuracy.

5.5 Time step sensitivity study

There were several criteria to consider when selecting the time step size. Ideally, the time step should be such that the relative mesh motion does not exceed the length of the smallest cell at the dynamic mesh interface. What is more, the Courant-Friedrichs-Lewy condition describes the convergence condition of partial differential equations:

$$CFL = \frac{v_i \Delta t}{\Delta x_i} \leq CFL_{MAX} \tag{5.6}$$

where Δt is time step size and Δx_i is cell size in direction x. Implicit solvers, which were used in the simulations, are less sensitive to numerical instabilities and permit values of CFL_{MAX} in the range of 200. However, increasing time step decreases solution accuracy. Therefore time step sensitivity study was performed.

Observed variables were mean oscillation frequency $\bar{f}$ and amplitude $\bar{A}$. 20 periods of oscillations were captured for each case. A comparison between results obtained with different dynamic mesh methods for the G3 grid is given in Table 5.4.

Table 5.4: Time step sensitivity study for the two-dimensional case.

		Overset mesh		**Layering, 1st order time discretization**		**Layering, 2nd order time discretization**	
Δt in s	**Mean *CFL***	**$\bar{A}$ in deg**	**f in Hz**	**$\bar{A}$ in deg**	**f in Hz**	**$\bar{A}$ in deg**	**f in Hz**
$8 \cdot 10^{-4}$	2,4	13,7	16,63	-	-	-	-
$4 \cdot 10^{-4}$	1,2	13,0	16,38	12,9	16,25	13,6	16,26
$2 \cdot 10^{-4}$	0,6	12,9	16,24	13,6	16,26	12,7	16,24
$1 \cdot 10^{-4}$	0,3	13,1	16,22	12,9	16,26	12,9	16,26

In the case of the layering method, $4 \cdot 10^{-4}$ s was the smallest permissible time step. For higher time steps the solution diverged. The overset mesh method allowed for larger time steps, but that would introduce an additional 2% error in frequency.

Below $4 \cdot 10^{-4}$ s the layering method was not sensitive to the time step value and the results were comparable, regardless of the order of time discretization. The overset mesh method required a smaller time-step to maintain accuracy.

Further tests confirmed the requirement of the mean *CFL* number to be below 1 for the overset case (Figure 5.10). Low sensitivity to time step for *CFL* < 1 has been also verified for the 3D case.

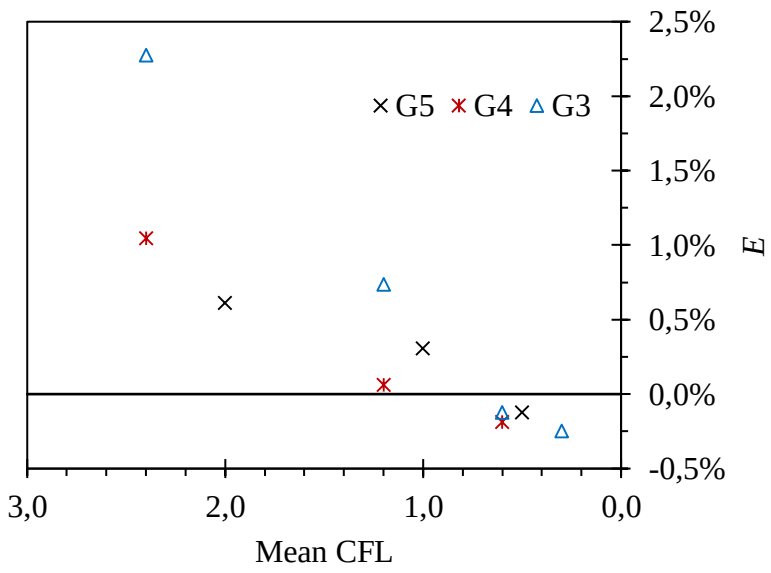

Figure 5.10: Influence of time step size on the oscillation frequency for the overset mesh method in reference to results obtained with the layering method of the same time step size and grid size. Series correspond to different grid sizes.

As an another example of timestep sensitivity, it was observed that with increasing time step parts of the velocity field are filtered out. In result, amplitude and frequency jitter is damped with increasing time step size, as illustrated in Figure 5.11 on the example of the two-dimensional model.

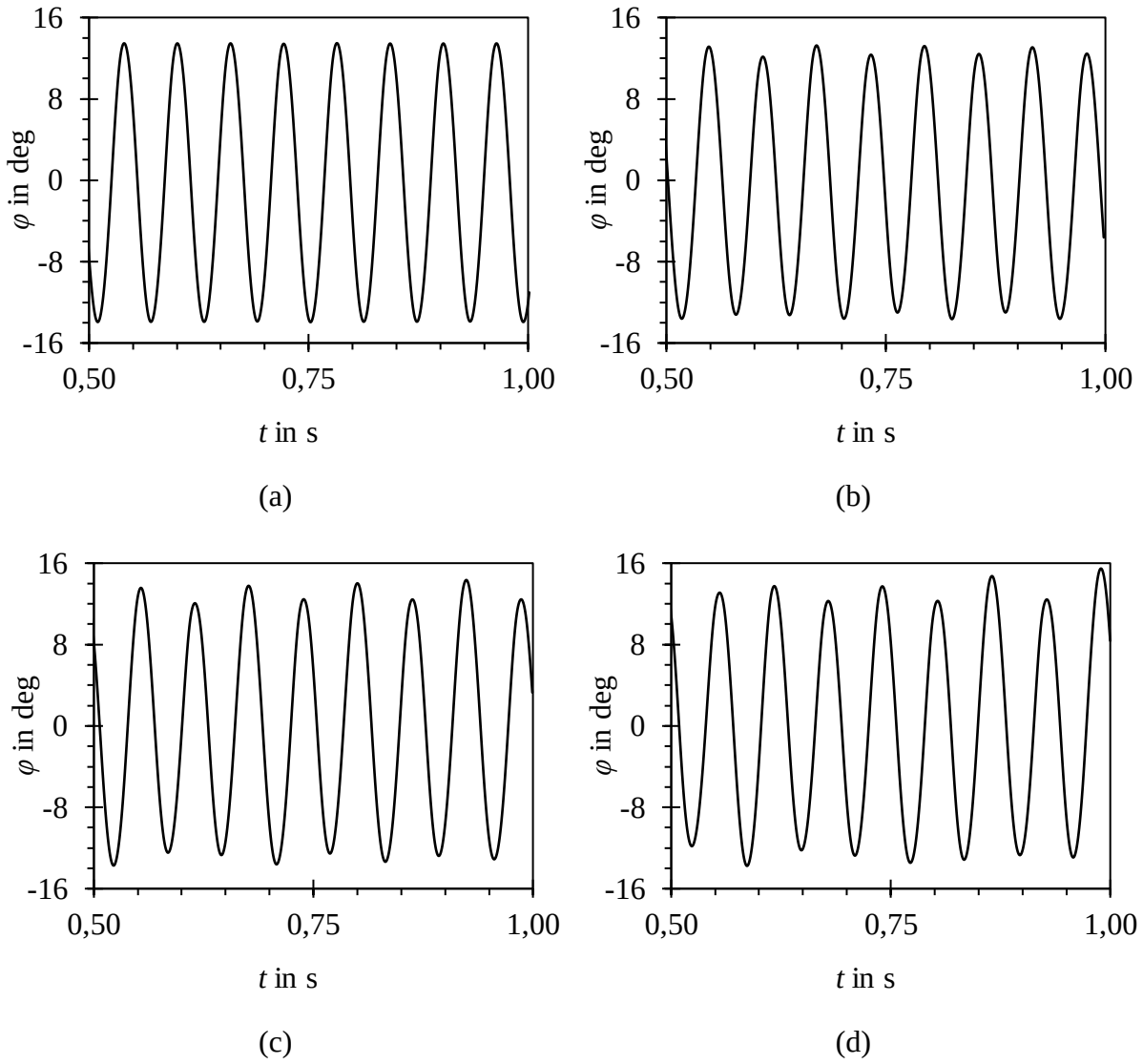

Figure 5.11: Oscillator position vs time for the two-dimensional model, G3 grid, various time step sizes. (a) $8 \cdot 10^{-4}$ s; (b) $4 \cdot 10^{-4}$ s; (c) $2 \cdot 10^{-4}$ s; (d) $1 \cdot 10^{-4}$ s. Increased jitter with reducing time step is visible.

Amplitude jitter was observed in the experiment. As shown in Figure 5.12, a deviation from the true periodicity of oscillations is present, both in terms of amplitude and frequency. Providing that the timestep is small enough, the numerical model captures that effect correctly. Amplitude jitter was confirmed also with visual observations, by mounting the oscillator in an acrylic glass body.

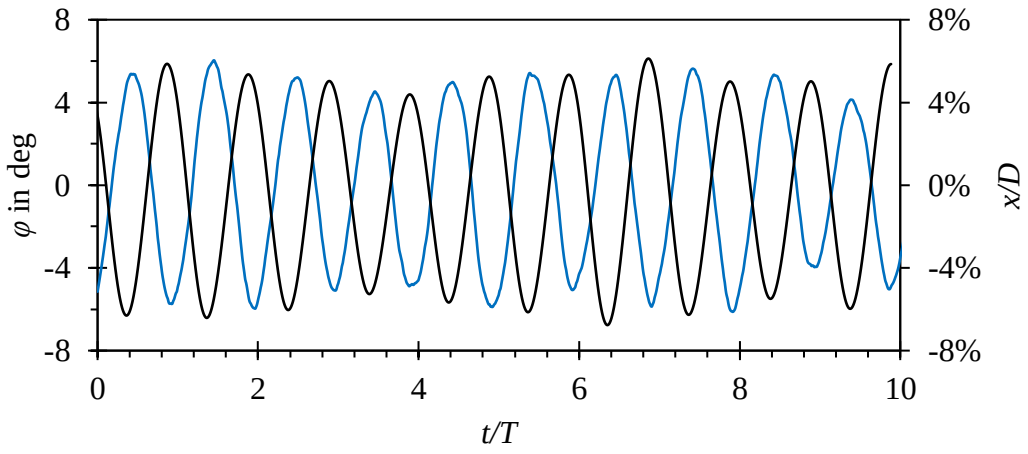

Figure 5.12: Position of the oscillator vs time for q_v = 40 m^3/h. Black line – three-dimensional numerical model, blue line – experiments. Series are offset by 0,5T intentionally, for clarity reasons.

The experimental study has shown that the mean amplitude of oscillations is constant for *Re* > 65 000 (ca. 8 m^3/h in Figure 5.13) and drops from 5,5 degrees to ca. 4,2 degrees for lower values of the Reynolds number. Although the mean amplitude for a given flow rate remains constant, the spread of captured oscillation amplitudes reaches up to 50%.

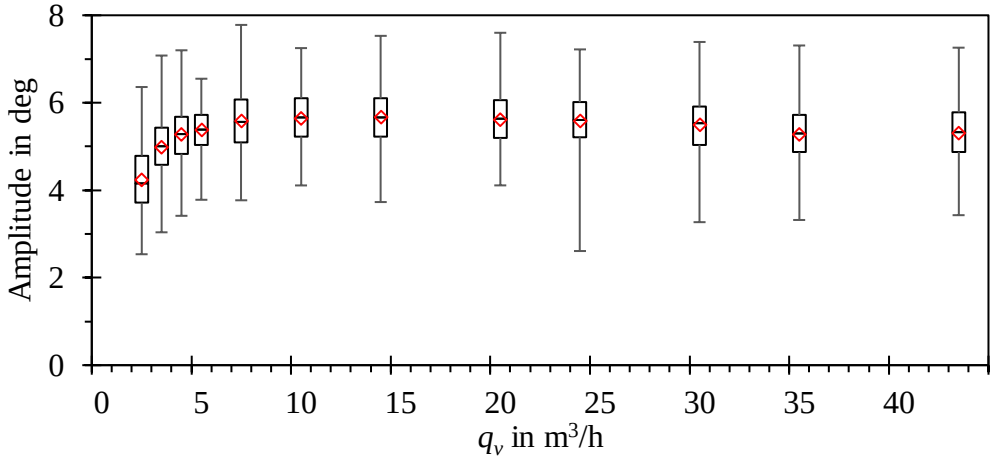

Figure 5.13: Box-whiskers plot of the amplitude of oscillations vs flow rate, measured at the water calibration stand.

In the two-dimensional case predicted amplitudes were ca. 2 times larger than in the three-dimensional case. The 2D model could not capture the circular pipe shape and wall proximity effects that limit the amplitude of oscillation in the real case. For that reason, it was not possible to relate 2D simulation results to the experiment. Nevertheless, the shape of the error curve

$K(q_v) = \overline{f} / q_v$ was qualitatively correct. The differences between results obtained with different turbulent models in 2D did not exceed 2,5%.

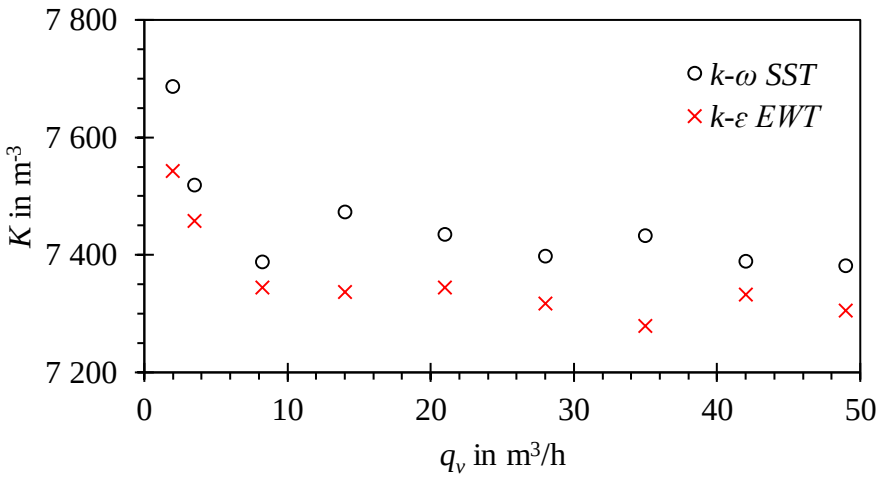

Figure 5.14: Error curve obtained with the two-dimensional model, overset method, G3 grid, mean CFL < 1.

In the 3D case, it was possible to relate the results to experimental values, as shown in Figure 5.15.

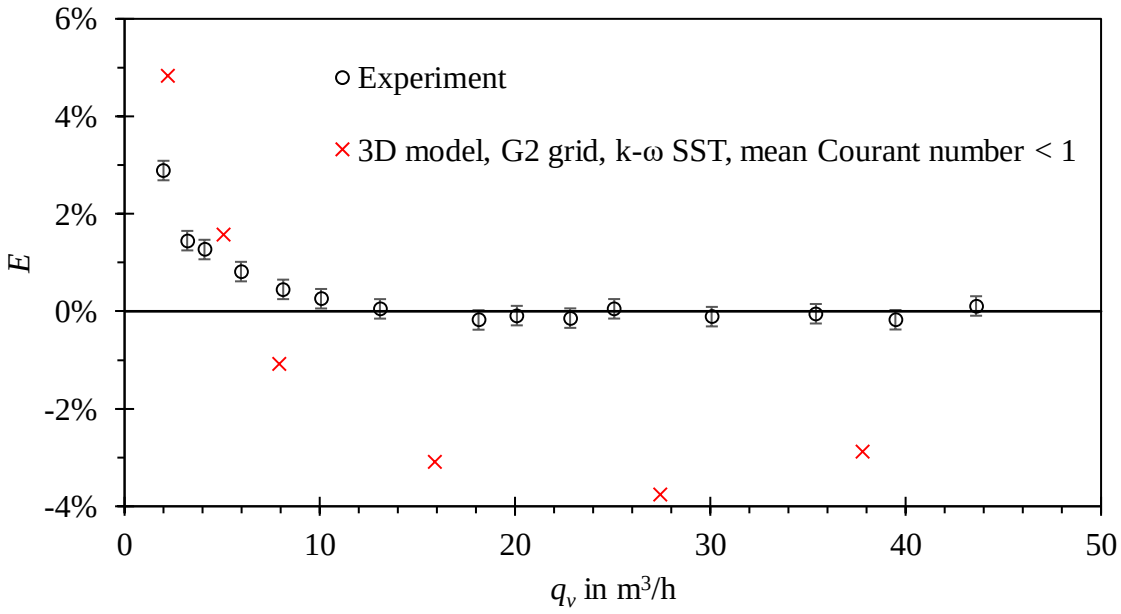

Figure 5.15: Error curves of the flowmeter for K = 10,03 imp/m^3. Validation of the three-dimensional model against experimental data. Error bars denote experiment uncertainty for coverage factor k = 2.

The relative differences between the model and experimental data did not exceed 4%, which is a low value concerning the selected class of turbulence models. Differences were attributed mostly to mesh sensitivity and modelling errors.

Differences between S-A, realizable k-ε and k-ω SST turbulence models were in the range of 1,5% in favor of the k-ω SST model. For that reason, this turbulence model was selected for the rest of the studied cases.

The agreement between error curves' shape for low Reynolds number can be further improved by introducing bearing friction to the numerical model. The results were considered satisfactory for further studies. The qualitative behavior of the model is correct and it allows both studying the flowmeter operation in detail and performing parametric studies.

5.6 Practical remarks

Because the oscillator operates in a limit cycle, the amplitude and frequency of oscillations do not depend on the initial position of the oscillator. Thus, the initial position in simulations could have been set close to the expected amplitude. As shown in Figure 5.16, this allowed reducing computation time by achieving periodic oscillations twice as fast in comparison to initialization with a neutral position of the oscillator.

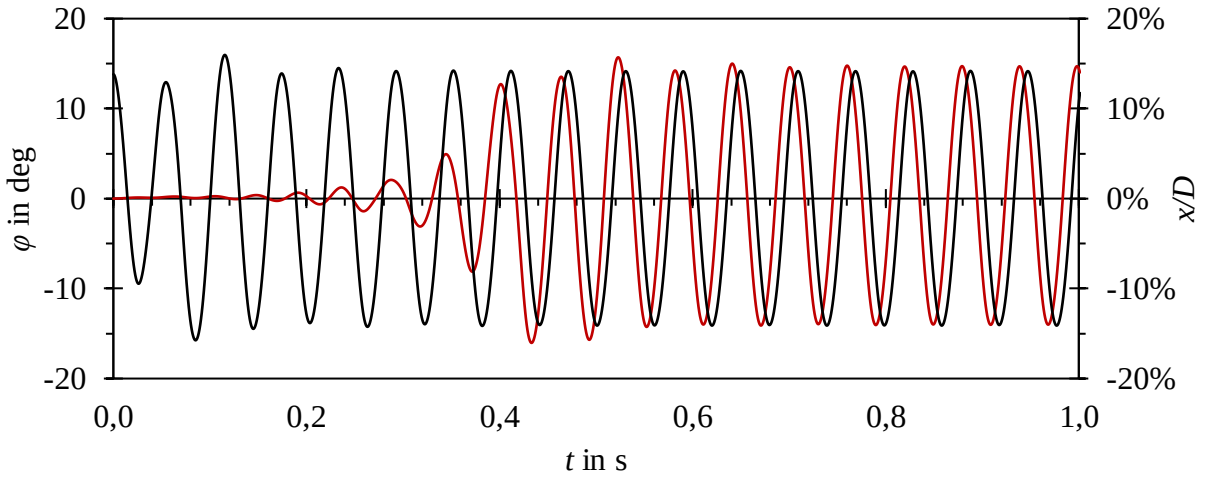

Figure 5.16: Oscillator position vs time for different initial positions of the oscillator. Red line – starting from $\varphi = 0°$, black line – starting from $\varphi = 14°$.

Although the overset mesh approach solves many issues in comparison to other dynamic mesh methods, its application on a high-performance computer turned out to be challenging.

Because of problems with load balancing and parallelization, the scalability of the problem was low, as shown in Figure 5.17.

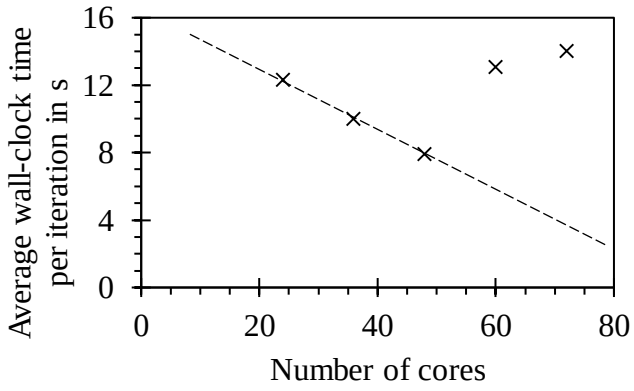

Figure 5.17: Three-dimensional overset dynamic mesh scalability. Dashed line represents the desired linear scalability and *x* markers represent the measured data.

Increasing the number of cores above 48 was counter-productive and increased the computation time. Various partitioning and dynamic load balancing methods were verified as proposed in (Reddy, 2004), but without noticeable improvement.

Chapter 6

Modelling

6.1 Discussion about the principle of operation

CFD modelling allowed studying pressure and velocity fields during the operation of the mechanical oscillator flowmeter. It is the key to understanding the principle of operation of the flowmeter. The following chapter will discuss the collected data.

To analyze forces and moments acting on the oscillator during its motion, let us pick a coordinate system where *x* is an axis in the flow direction and *y* is in the perpendicular direction, as in Figure 6.1. The torque acting on the oscillator has a positive sign if it forces the oscillator to move in the anticlockwise direction.

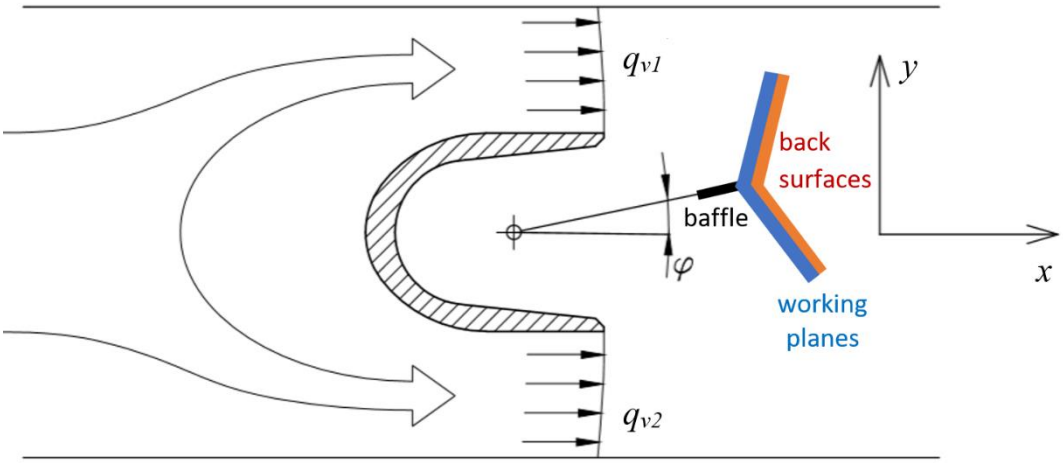

Figure 6.1: The coordinate system used in the presented study.

As the oscillator moves from side to side, it obstructs the flow in one of the passages created by the stream divider. CFD analysis has shown that in the three-dimensional case the maximal imbalance of flow rate between channels of the stream divider equals ca. 3% (Figure 6.2a) and in the two-dimensional case ca. 6% (Figure 6.2b). That means the velocity of the stream impinging on the oscillator is not constant, which was not included by any of the existing analytical models. The differences between 2D and 3D in that case result from different amplitudes of motion.

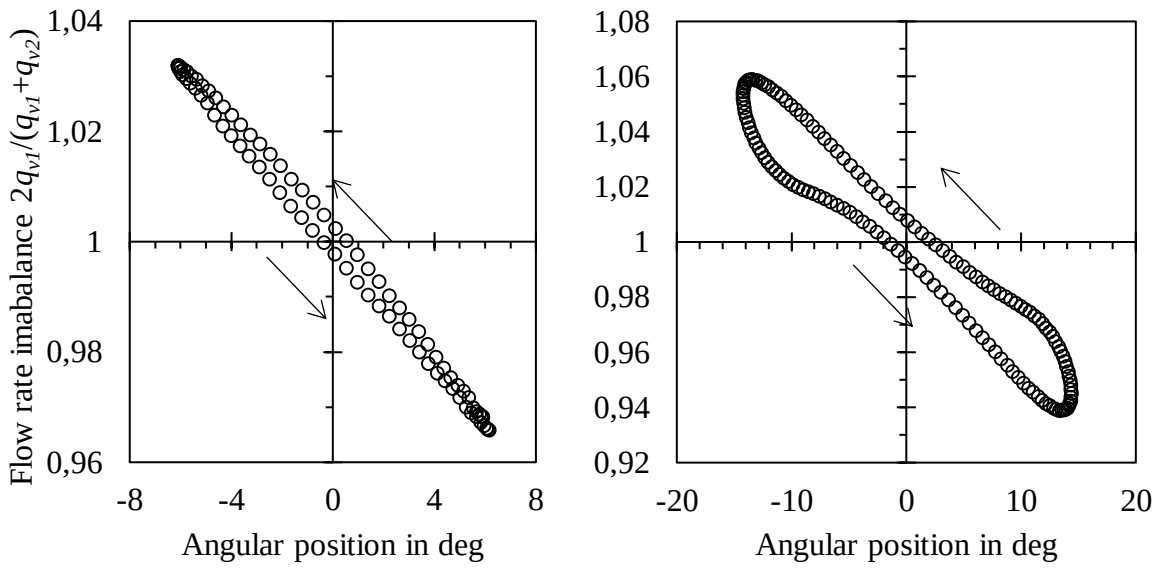

(a) (b)

Figure 6.2: Imbalance of the flow rate between channels of the stream divider in the function of the oscillator position. (a) Three-dimensional CFD model; (b) two-dimensional CFD model.

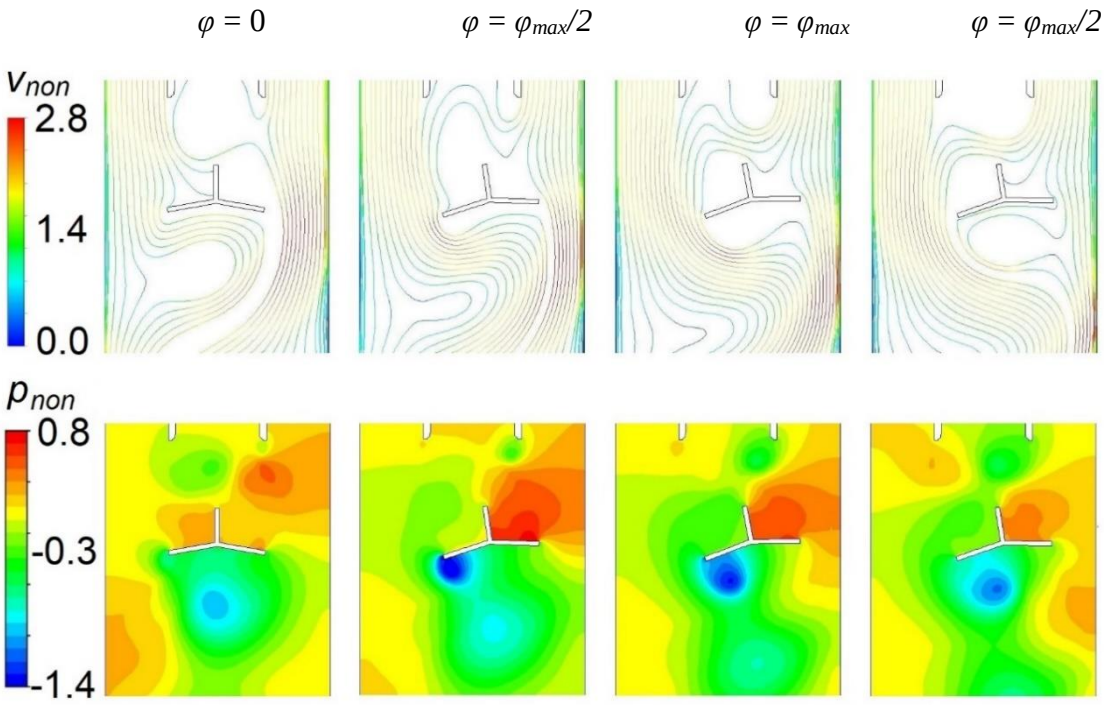

Figure 6.3: Two-dimensional model, a sequence of images over a quarter of an oscillation cycle. Top – pathlines colored by nondimensional velocity (normalized by inlet velocity). Bottom – contours of nondimensional pressure (normalized by dynamic pressure).

More useful information can be derived from observing the flow field in the proximity of the oscillator. Figure 6.3 shows a sequence of images over a quarter of an oscillation cycle. As the oscillator enters the stream, a vortex builds up on the side of the oscillator that is hidden behind the stream divider. It causes a local decrease in pressure and an increase in velocity. As the oscillator reaches the extreme angular position and starts to move back, the vortex detaches and is swept with the flow. The influence of the vortex street on the torque acting on the oscillator will be discussed below.

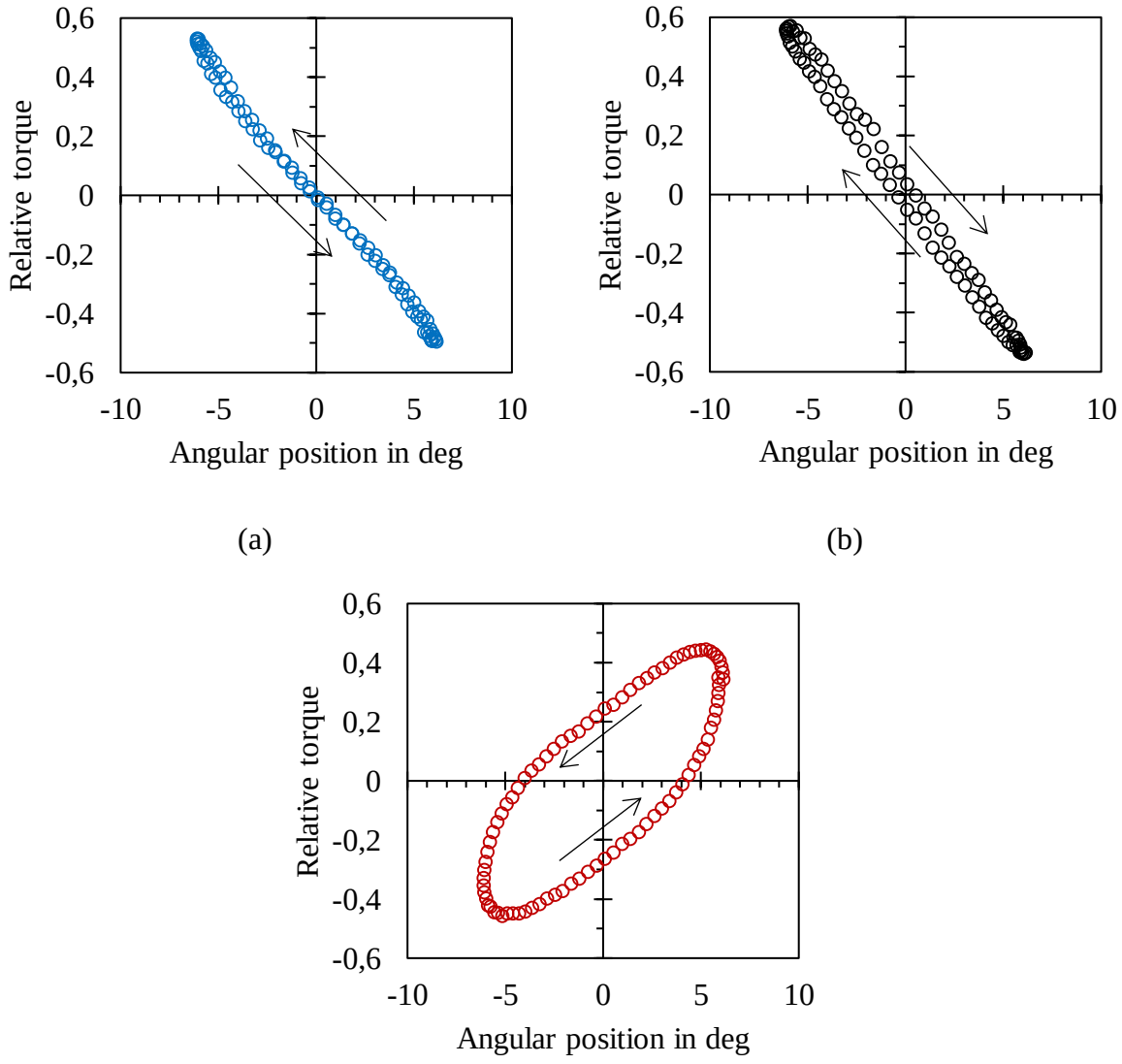

Figure 6.4: Results from three-dimensional CFD, relative torque vs angular position for (a) working planes (b) baffle (c) rear surfaces.

Figure 6.4 depicts torques acting on the selected parts of the oscillator. They are normalized by the maximal value of the total torque in the whole range of motion. Points lying in the 2nd and 4th quadrants of the plot mean that the torque is forcing the oscillator towards the neutral position. The component of torque that acts comes from the working planes (Figure 6.4a) is contained in the 2nd and 4th quadrants in its entirety and the slope increases for increasing angular position. In the case of the baffle (Figure 6.4b) the slope of the torque-position curve is constant, but hysteresis is present. As the oscillator approaches the neutral position ($\varphi = 0°$), the torque originating from the baffle pushes it further out of the neutral position. Lastly, Figure 6.4c demonstrates the relative torque acting on the back surfaces. In the initial part of motion, from $\varphi = 0°$ to $\varphi_{max}/2$, the torque forces the oscillator back into the neutral position. For the other part of motion, from $\varphi_{max}/2$ to φ_{max} and back to $\varphi = 0°$, the torque changes sign.

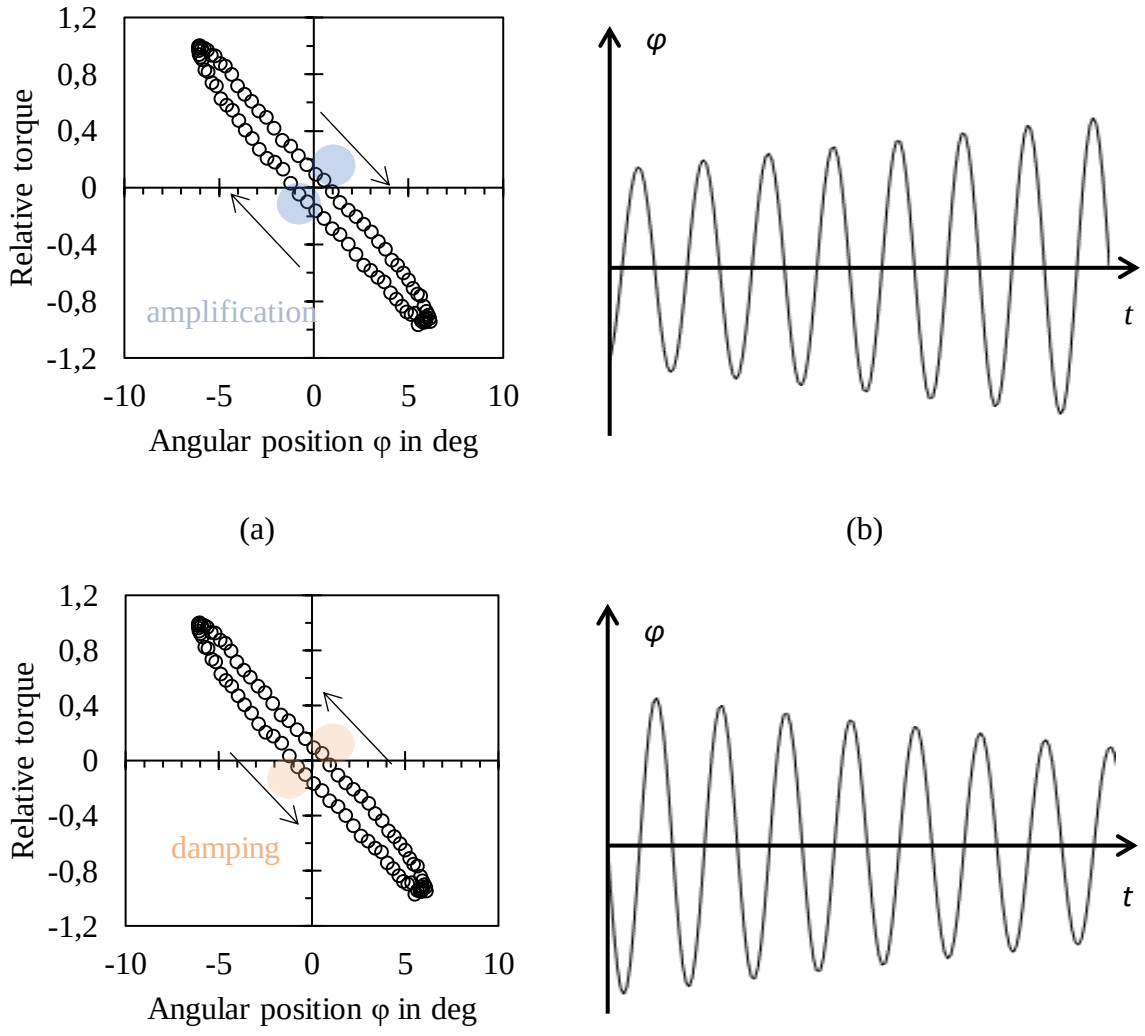

Figure 6.5: Captured variants of the total torque-position curve and their effect on oscillation amplitude. (a-b) Amplified oscillations; (c-d) damped oscillations.

This underlines the complexity of the underlying flow patterns. The presence of hysteresis emphasizes transient nature of the studied phenomena. All in all, the exact values of torque acting on the individual surfaces of the oscillator vary from cycle to cycle to such an extent, that the total torque may take shapes as shown in Figure 6.5a and c. The direction in which the oscillator moves along the torque-position loop determines if the amplitude of oscillations is increasing or decreasing. In the case of direction marked in Figure 6.5a, the amplitude of oscillations grows in time, as shown illustratively in Figure 6.5b. When the oscillation amplitude reaches a certain threshold value, the torque-position loop switches direction (Figure 6.5c) and oscillations are damped, which is demonstrated in Figure 6.5d.

In the result of these alternating damped and amplified cycles, amplitude jitter is present (Figure 6.6a) and the oscillator works in a limit-cycle in form of a “trapping region”, as shown in Figure 6.6b.

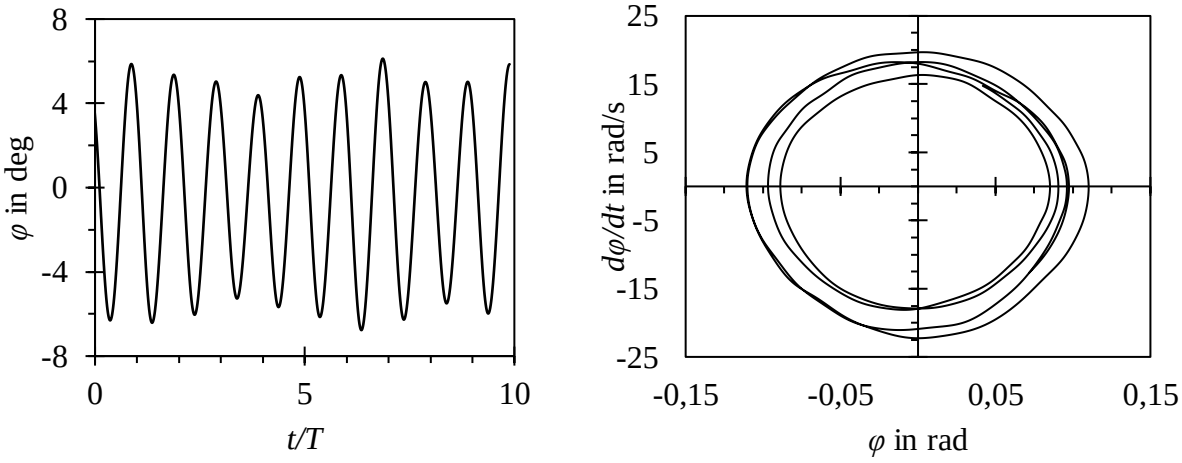

Figure 6.6: Data from three-dimensional CFD model, (a) amplitude vs time (b) phase portrait.

The numerical model developed by the author allowed studying the principle of operation of the flowmeter. It has many practical applications, one of which will be presented in the next chapter, namely improving the linearity of the calibration curve. The total torque-position curve will also be used in mathematical modelling in Chapter 7.2.2.

6.2 A method of improving calibration curve linearity

6.2.1 Introduction and methods

The nonlinearity of the calibration curve for small Reynolds numbers is commonly found for flowmeters which are susceptible to viscosity changes. In this regime, viscosity forces become comparable to inertia forces and boundary layer effects become important. Strictly speaking, the velocity profile acting on the oscillator is inconstant in the function of the flow rate – it sharpens as Reynolds number approaches the laminar regime. The sharper velocity profile has larger kinetic energy. For that reason, the calibration factor increases with reducing Reynolds number, as portrayed in Figure 6.7.

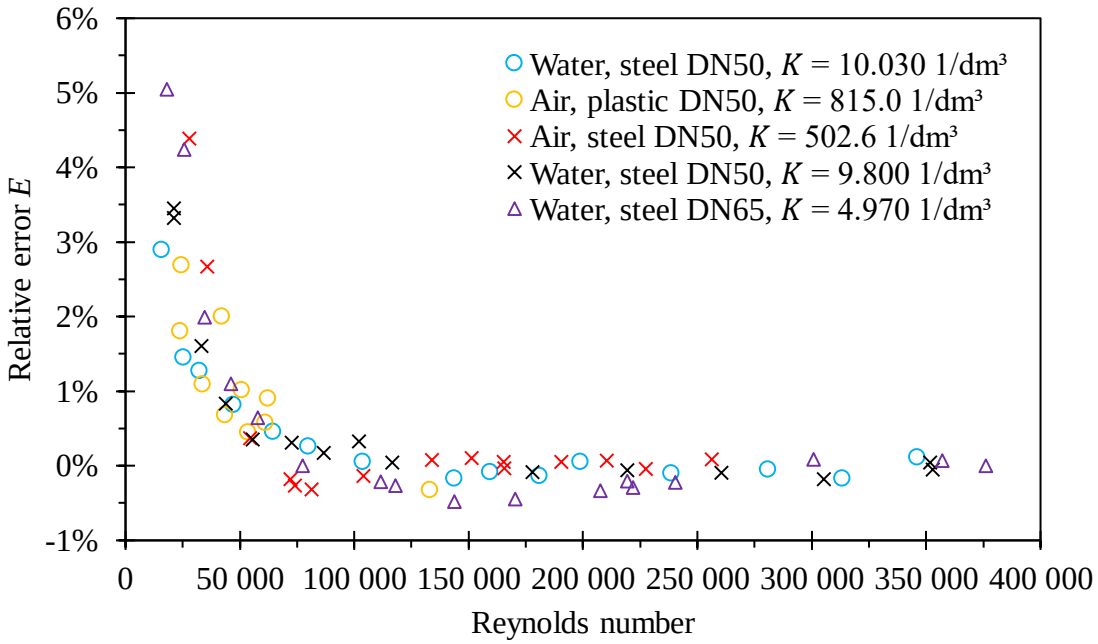

Figure 6.7: Error curves in the function of Reynolds number for various fluids, oscillator materials and nominal sizes. Same pattern can be observed.

A solution to this issue is to reduce the influence of Reynolds number on the incoming velocity profile. (Kremlewskij, 1989), who worked on turbine flowmeters, proposed installing an orifice that would disturb the incoming velocity profile. If the orifice was installed in a small distance from the impeller it would not allow a new boundary layer to form. A similar solution can be found in the previous version of ISO 5167 standard concerning orifice flowmeters (International Organization for Standardization, 1980), where an additional orifice is installed upstream to reorder the flow profile. (Turkowski, 2003c) initially reported that this method brings positive results in the case of mechanical oscillator flowmeters.

The goal of the presented study was to examine the proposed method of improving the calibration curve linearity in more detail. Various orifice bore diameters were studied. It was verified whether positive results could be also achieved using plate flow conditioners. Their purpose is to reorder the incoming flow profile to recreate a fully developed turbulent velocity profile and eddy pattern (International Organization for Standardization, 2003b). The method was verified using the three-dimensional CFD model and experiments. Coriolis coefficient C_c (Jeżowiecka-Kabsch and Szewczyk, 2001; Pospolita, 2004) was used as a measure to compare studied cases:

$$C_C = \frac{\oiint_A v_x^3 dA}{\overline{v_x}^3 A} \tag{6.1}$$

where v_x is the axial component of velocity, A is the cross-section area and $\overline{v_x}$ is the mean value of the axial velocity component.

6.2.2 Results and discussion

As shown in Table 6.1 and Figure 6.8, orifice causes the flow profile to be less uniform, which corresponds to larger values of Coriolis coefficients.

Table 6.1: Coriolis coefficient in the channel of a stream divider.

Orifice bore diameter in mm	**C_c for $Re = 3 \cdot 10^5$**
44	1,152
48	1,031
no orifice	1,027

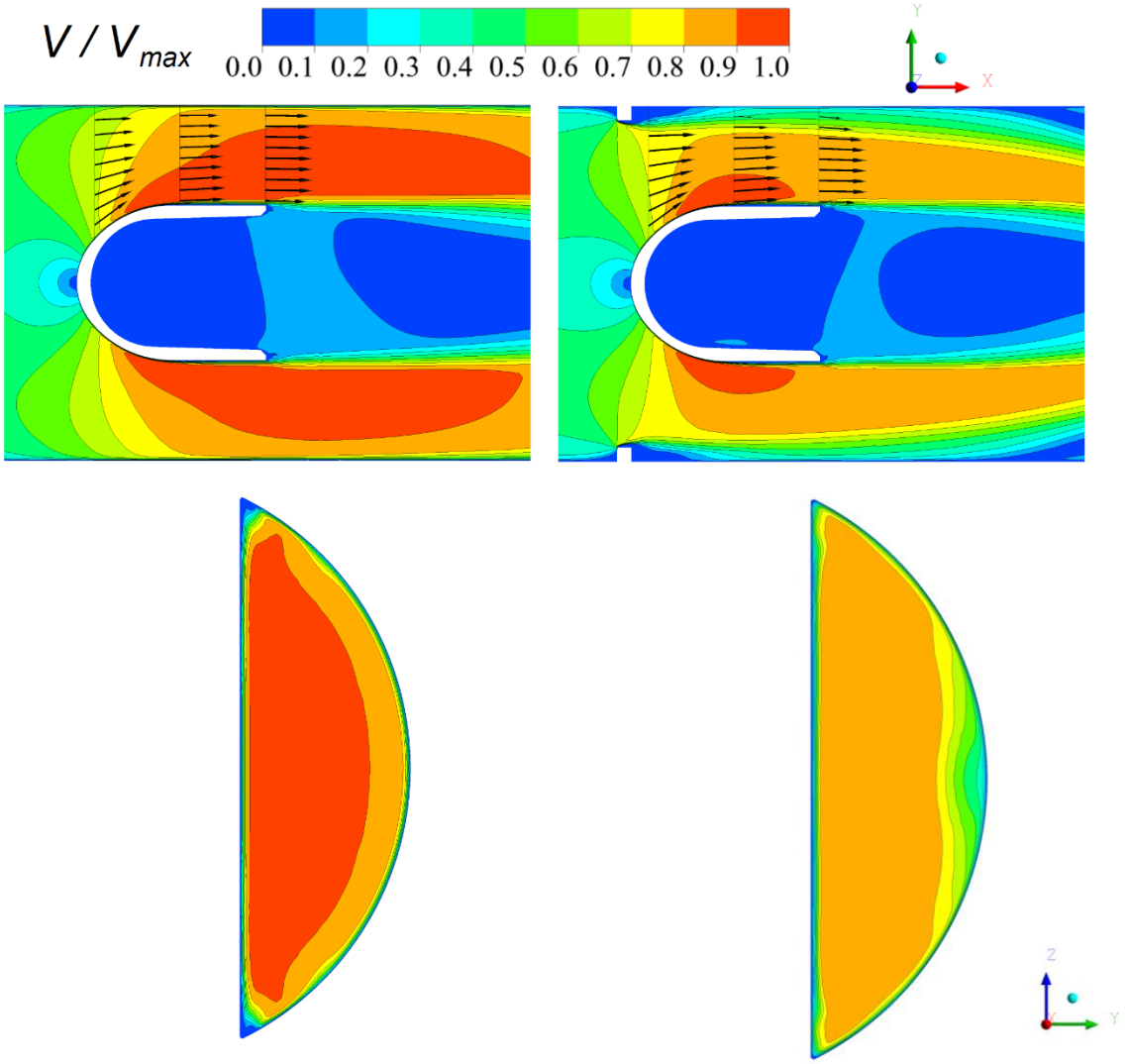

Figure 6.8: Influence of an orifice installed at the flowmeter inlet on the velocity distribution. Orifice successfully removes the inflowing boundary layer, increasing insensitivity to the Reynolds number. *Re* = 63 000; top – view of the symmetry plane, bottom – a cross-section of the channel at the rear end of the stream divider; (a) no orifice (b) *Φ*46 orifice.

It is of secondary importance whether C_c is larger or smaller. What matters is it remains constant in function of the Reynolds number. CFD simulations showed that indeed orifices reduce the influence of the inflowing boundary layer on the resultant velocity profile. This translates to the desired lower variability in the function of Reynolds number, which is shown in Figure 6.9. ΔC_c is the relative change of Coriolis coefficient between C_c for the given Reynolds number and the value of C_c for the highest studied Reynolds number equal to 300 000:

$$\Delta C_C(Re) = \frac{C_C(Re) - C_C(3 \cdot 10^5)}{C_C(3 \cdot 10^5)} \tag{6.2}$$

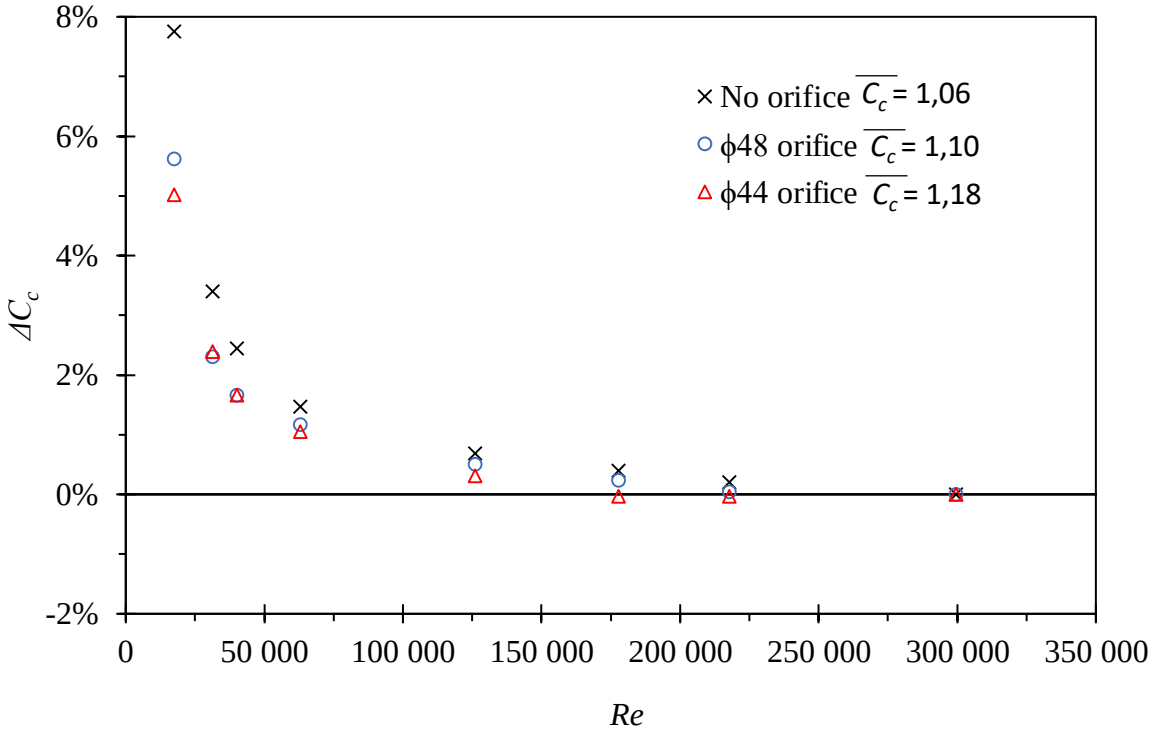

Figure 6.9: Relative change in Coriolis coefficient vs Reynolds number for various orifice bore diameters. The lower the orifice bore diameter, the smaller the variation of C_c in function of *Re*.

The differences between cases portrayed in Figure 6.9 are in the range of 0,5%. They may seem unimportant, but it must be noted that nonlinearities in the error curve are of the same order of magnitude. Experiments conducted at the water calibration stand confirmed qualitatively the above simulation results. Captured error curves are shown in Figure 6.10.

As expected, placing an orifice at the front of a flowmeter increases the value of Coriolis coefficient and increases its mean calibration constant *K*. 48 mm and 46 mm orifices increase the linearity of the calibration curve for *Re* below 100 000. No effect on the linearity is observed for higher *Re*. For 44 mm orifice oscillations were unstable and no meaningful measurements could be done. Spearman plate conditioner installed at the distance of 10*D* before the flowmeter did not affect the linearity of the calibration curve. Instead, it introduced a significant pressure drop. An additional disadvantage of plate conditioners is that their small bores are prone to sediments and foreign bodies.

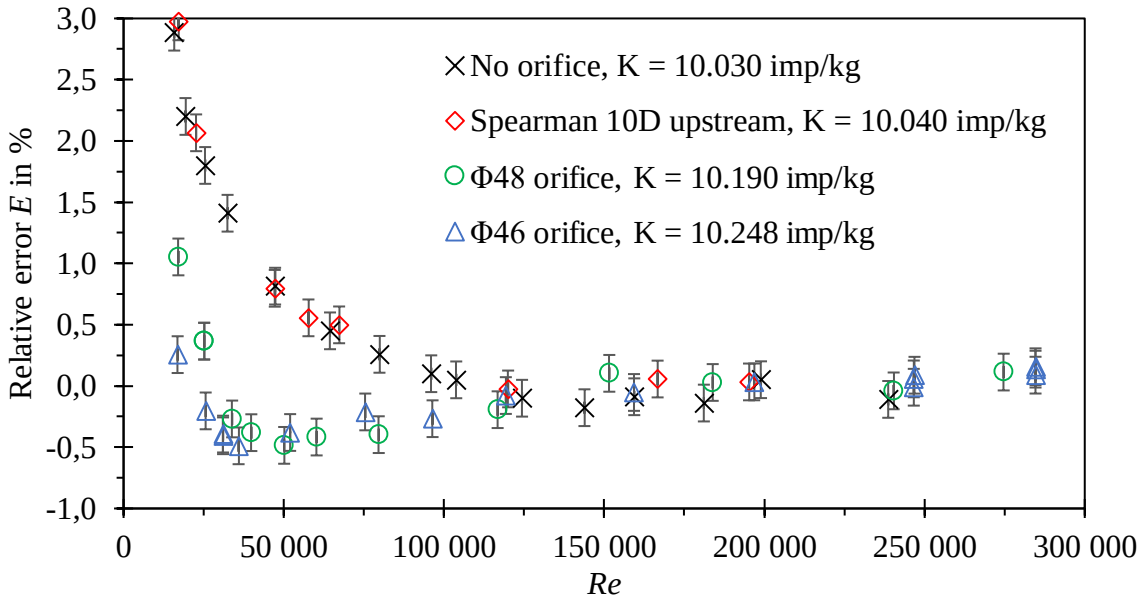

Figure 6.10: Relative error vs Reynolds number, error bars denote combined measurement uncertainty for coverage factor k = 2. A positive effect of orifices on the error curve linearity can be observed.

Table 6.2: Rangeability and pressure losses for various configurations.

Auxiliary flow element	***Re* corresponding to *E* = 0,5%**	**Rangeability***	**Pressure loss coefficient**
None	65 000	6	3,2
Spearman flow conditioner	65 000	6	6,4
Φ48 orifice	25 000	16	4,1
Φ46 orifice	15 000	26	4,5

* q_{max}/q_{min}, where q_{max} = 50 m^3/h and q_{min} is the flow rate corresponding to E = 0,5%

The price for increased linearity is increased pressure loss due to recirculation zones. Data collected in Table 6.2 compares the cost-effectiveness of various solutions. The minimum flow rate concerns nonlinearity error of 0,5%. Pressure loss coefficient ξ was determined for the assembly of a flowmeter and an element installed at the inlet using the formula:

$$\xi = \frac{2\Delta p}{\rho v^2} \tag{6.3}$$

where Δp is a pressure difference measured 18xDN upstream and 7xDN downstream the flowmeter.

6.2.3 Conclusions

The method of improving the error curve linearity was examined. Orifices of bore diameter 46 mm and 48 mm successfully reduce the influence of Reynolds number on the velocity profile. Increase in rangeability from 6:1 to 26:1 can be achieved. The cost of installing an orifice is in the form of ca. 35% increase in pressure losses.

If a bore diameter is equal to 44 mm or less, the recirculation zone grows excessively and the oscillator works in an unstable manner. Conditioning plate installed 10D upstream the flowmeter does not affect the error curve. Bringing the plate closer to the flowmeter deteriorates its performance.

The next chapter will focus on further improving the performance of the flowmeter, but this time by modifying the geometry of the oscillator.

Chapter 7

Influence of oscillator's shape on the energy of oscillations

7.1. Previous findings

This chapter aims to validate and extend previous considerations on the relation between the geometry of the oscillator and the energy of oscillations. The main points of analyses made by (Heckle, 1973; Turkowski, 2003b) will, therefore, be summarized below. Their considerations are based on the assumption that the incoming velocity profile is uniform, the flow is two-dimensional, the fluid is not compressible, the flow is steady, and that the viscous friction can be neglected. By these assumptions, the conservation of momentum law can be used to describe the force P and torque τ acting on the oscillator's working plane, as in Figure 7.1a.

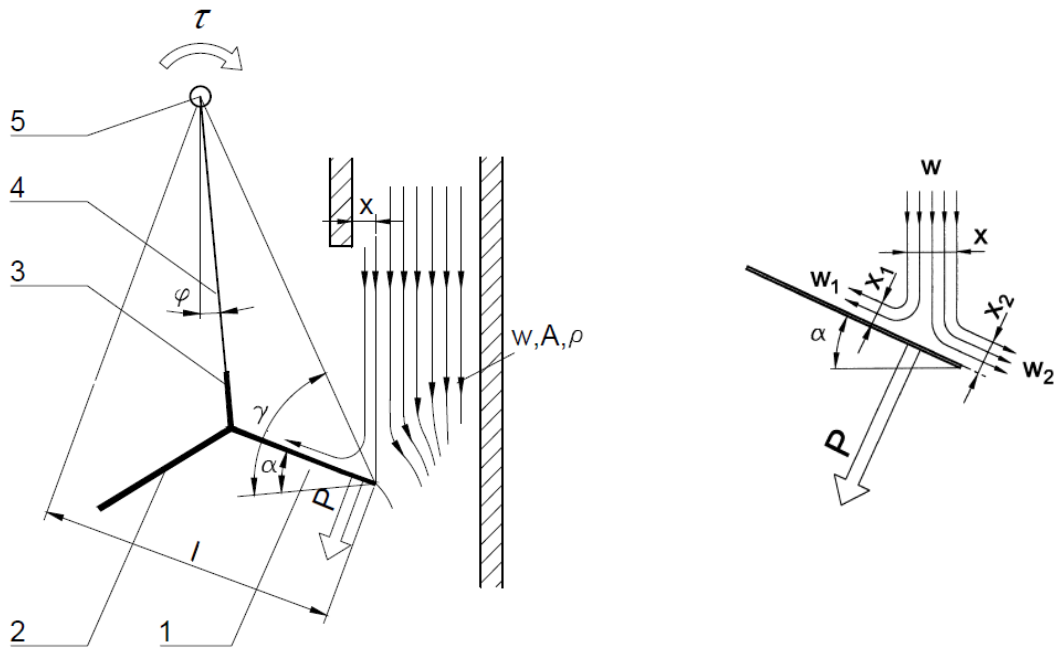

(a) (b)

Figure 7.1: (a) Sketch to determine torque acting on the working plane: 1 – working plane, 2 – hidden plane, 3 – baffle, 4 – support, 5 – bearing; (b) stream impinging on a sloped surface; both figures were adapted from (Turkowski, 2003b).

$$A = hx \tag{7.1}$$

$$l = \frac{s\cos(\gamma - \alpha)}{2\cos\gamma} \tag{7.2}$$

$$\tau = Pl = \rho A w^2 l = \rho h x w^2 \frac{s\cos(\gamma - \alpha)}{2\cos\gamma} \tag{7.3}$$

where ρ is the density, w is the mean velocity in the channel of a stream divider, l is the level arm of the force P, s is the oscillator's width, α and γ are angles describing oscillator's geometry, h is the oscillator's height, x is the depth of immersion into the stream.

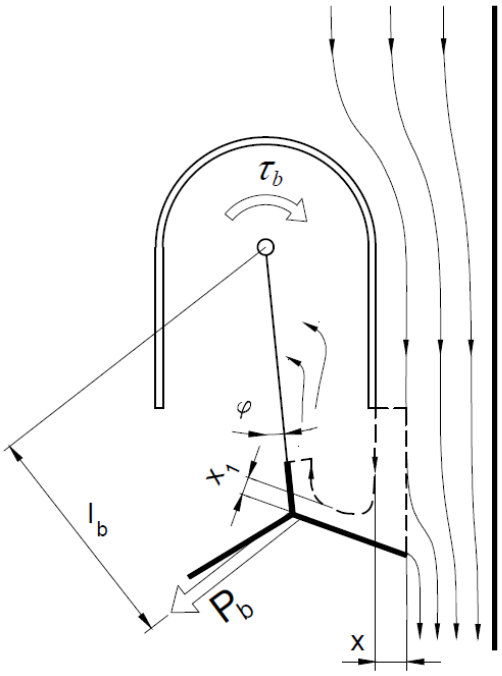

Figure 7.2: Sketch to determine torque acting on the baffle, adapted from (Turkowski, 2003b).

Assuming that the flow is two-dimensional, when the main part of the stream encounters an inclined working plane of the oscillator, it splits into two parts (Figure 7.1b). The second component of the torque acting on the oscillator results from part of the stream that impinges on a baffle (Figure 7.2). Keeping in mind the assumptions, one can write:

$$x = x_1 + x_2 \qquad \text{and} \qquad w = w_1 = w_2 \tag{7.4}$$

Furthermore:

$$x_1 = \frac{x}{2}(1-\sin\alpha) \tag{7.5}$$

Torque originating from the fluid acting on the baffle is equal to:

$$\tau_b = P_b l_b \tag{7.6}$$

$$P_b = 2\rho w^2 h \frac{x}{2}(1-\sin\alpha)\sin\left(\frac{\pi}{2}+\alpha\right) \tag{7.7}$$

$$l_b = \frac{s}{2}(tg\gamma - tg\alpha)\sin\left(\frac{\pi}{4}+\frac{\alpha}{2}\right) \tag{7.8}$$

Differentiating torques acting on the oscillator with respect to *x* gives an equivalent of the mechanical stiffness of the spring. Nondimensionalization is achieved by dividing by $\rho w^2 hs$.

$$k' = \frac{\partial\tau}{\partial x}\cdot\frac{1}{\rho w^2 hs} \qquad\qquad k'_B = \frac{\partial\tau_B}{\partial x}\cdot\frac{1}{\rho w^2 hs} \tag{7.9}$$

The criterial function for optimizing oscillator's geometry is the sum of nondimensional spring stiffness equivalents, denoted as *F* and referred to as nondimensional stiffness. It should be as large as possible, it is synonymous with maximizing the torque acting on the oscillator in its extreme positions. In other words, the slope of the total torque-position curve pictured in Figure 6.5 should be as high as possible. The graph of *F* function and its components are presented in Figure 7.5.

$$\begin{aligned} F = k' + k'_B = \frac{\cos\alpha\cos(\gamma-\alpha)}{2\cos\gamma} + \\ + \frac{1}{2}(1-\sin\alpha)(\tan\gamma-\tan\alpha)\sin\left(\frac{\pi}{4}+\frac{\alpha}{2}\right)\sin\left(\frac{\pi}{2}+\alpha\right) \end{aligned} \tag{7.10}$$

The above analysis by (Turkowski, 2003b) was followed by an experimental study using a low-pressure air test stand and a DN 200 model flowmeter that allowed for static torque

measurement. The following conclusions were drawn. First of all, the value of inclination angle α in the range of (0 – 40)° does not significantly affect F. However, experiments have shown that lower values of α result in more stable oscillations. It has been attributed to the larger role of the baffle in this range. Secondly, although theoretical considerations do not cover the length of the baffle at all, the appropriate length has been determined experimentally as 0,2D. A baffle shorter than the thickness of the split stream would result in reduced torque. A too-large baffle would introduce significant damping forces. What is more, visual observations have shown that the flow structure is far from two-dimensional, as part of the stream was deflected upwards and downwards the oscillator plane. This part of the stream did not result in an additional torque. The solution was to mount limiting planes at both edges of the oscillator. Finally, the conclusion was drawn that the value of γ should be as high as possible. Technological possibilities allowed using γ = 70° for the final design of the flowmeter.

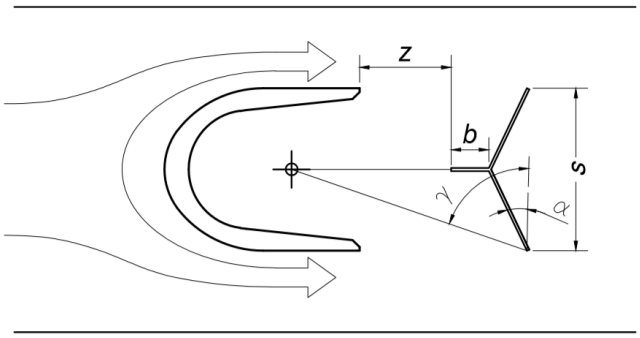

Figure 7.3: Sketch introducing oscillator dimensions.

The existing studies require an extension. Presented theoretical analyses were not validated quantitively, there were no attempts to determine nondimensional stiffness values from experimental data. The theoretical model is based on numerous assumptions, which impact will be verified. In reality, the incoming velocity profile is not uniform and it varies in function of φ. What is more, flow structures are unsteady and three-dimensional.

Previous experimental studies did not consider the distance between the rear edge of the flow divider and the oscillator z as an important factor (Figure 7.3), which will be proved otherwise. In theory, increased oscillation energy should decrease the minimum flow rate above which the oscillator operates and should increase the insensitivity to external disturbances. The suppositions that increased energy of the oscillations is beneficial for some of the metrological properties have not been validated before.

All of these aspects will be touched upon in the following chapter with the use of numerical model and experiments. First, three-dimensional simulations in steady state with an immobilized oscillator will be performed to compare with the existing analytical models. Then, transient analyses will be conducted and influence of the geometry on the nondimensional stiffness will be examined. Finally, it will be verified how the nondimensional stiffness affects performance of the flowmeter.

7.2 Parametric study

7.2.1. Static cases

The first observation that can be made with the use of the developed numerical model is the importance of limiting planes. Their impact can be observed in Figure 7.4a, where the pressure distribution over the surface of an oscillator may be considered as two-dimensional excluding the proximity of the support and limiting planes, in contrast to Figure 7.4b. The application of limiting planes increases the torque acting on the oscillator by ca. 25%. The effect was found to be greater for lower values of inclination angle α.

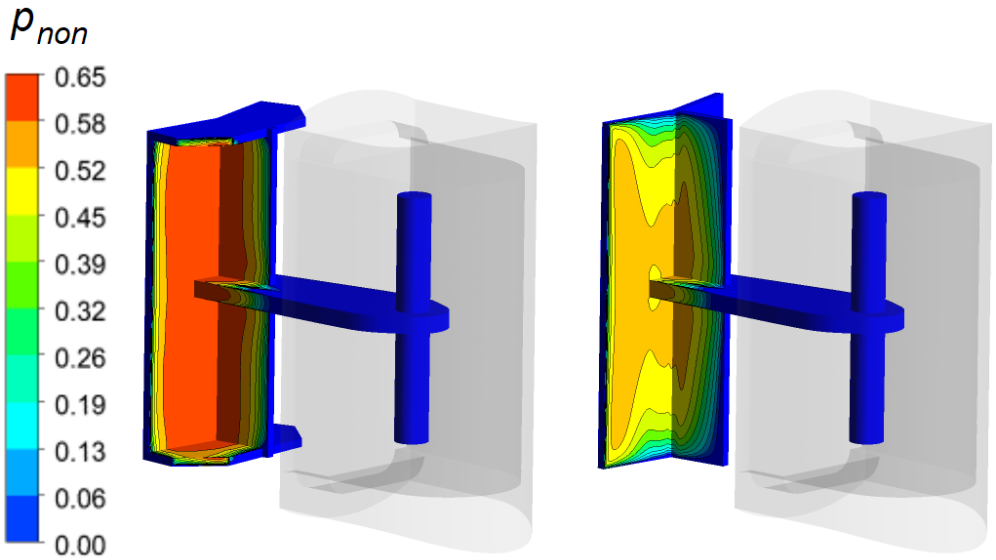

Figure 7.4: Contours of nondimensional pressure for the baseline case with (a) and without (b) the limiting planes.

Then, a comparison between a three-dimensional CFD model with an immobilized oscillator and an analytical model was conducted. Its results are presented in Figure 7.5. Both the F

function and its components agree qualitatively. However, due to the numerous assumptions of the analytical model the relative differences between the analytical model and CFD are up to 100%.

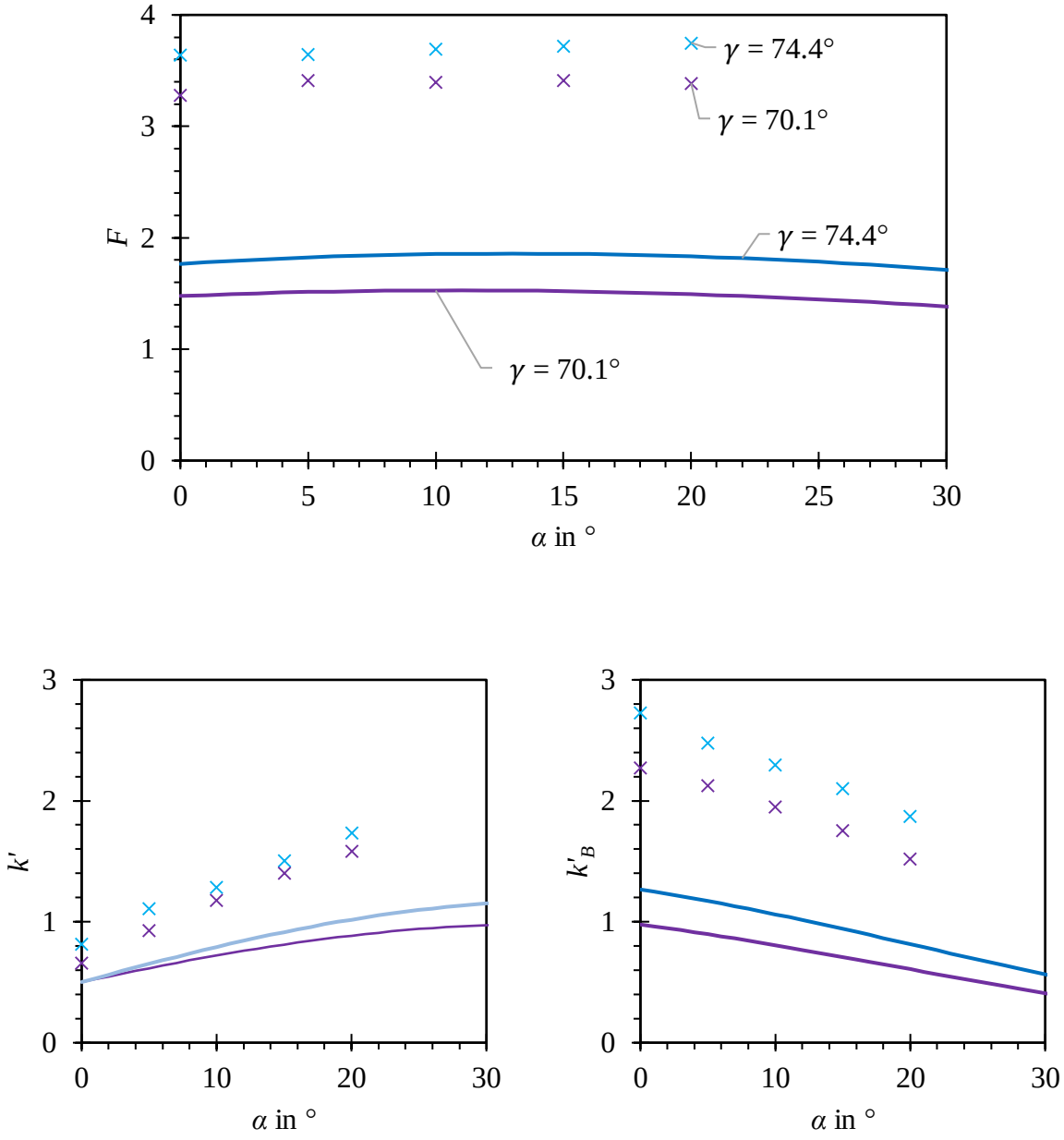

Figure 7.5: Graph of the criterial function *F* and its components, comparison of the analytical model (lines) and 3D steady-state CFD analyses (x symbols).

The reason for such a discrepancy is pictured in Figure 7.6 for the case of $\varphi = 6°$, $\gamma = 70{,}1°$, $\alpha = 10°$, $b/D = 15\%$ and $z/D = 20\%$. The largest differences in total came from the assumption of the analytical model, that only the parts of the oscillator immersed in the stream are contributing to the torque. The numerical model has shown that the contribution of the hidden sides of the baffle and working plane is significant. The part of the stream that is deflected towards the baffle accelerates and joins with the second stream, creating a low-pressure zone that attracts the oscillator and generates additional torque. Of secondary importance are contributions coming from the action of the fluid on the support, side surfaces and the effects of viscous friction, all of which are not included by the analytical model.

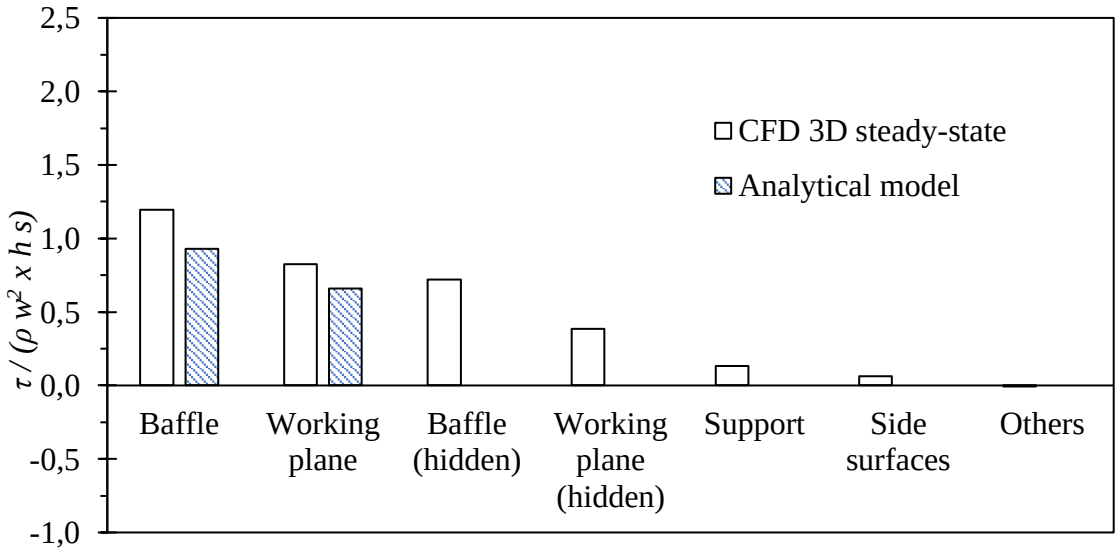

Figure 7.6: Nondimensional stiffness for various components. Group “others” includes both limiting planes and rear surfaces of the oscillator.

Nondimensional stiffness acting on the baffle and the working plane was off between CFD and the analytical model by ca. 20%. The exact values depended on the height of the baffle (Figure 7.7), which was not taken into account by the analytical model. However, three-dimensional simulations have confirmed the suppositions of the analytical model, that with increasing α the contribution of the baffle is decreasing. The effect of baffle height on k' was weak regardless of α.

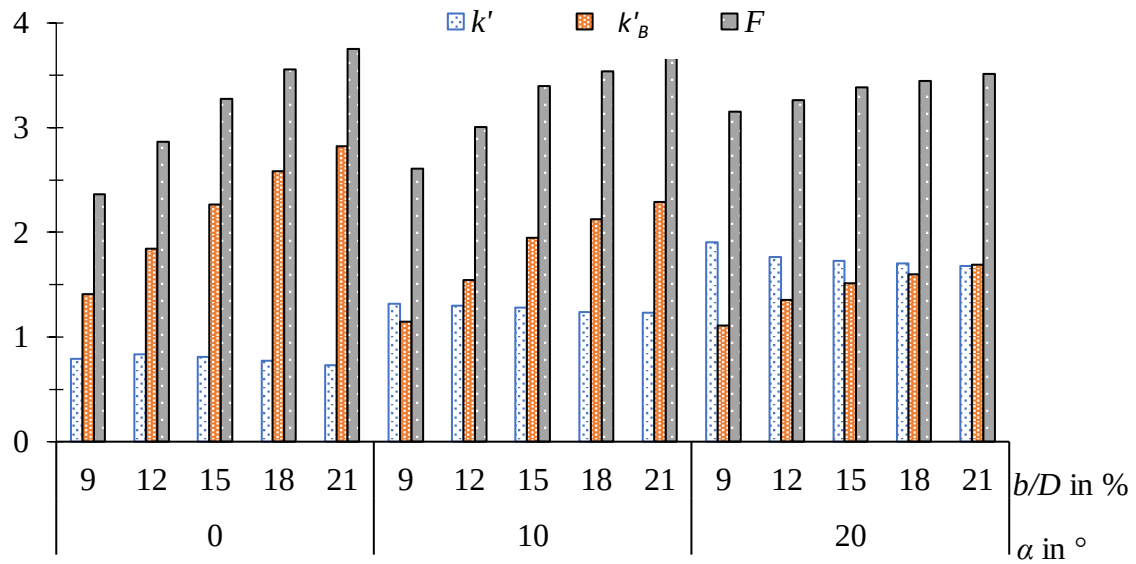

Figure 7.7: Influence of baffle height *b* and angle *α* on the nondimensional stiffness *F* and its components originating from the working plane *k'* and from the baffle *k'b*. 3D steady-state numerical model.

Back surfaces did not contribute to the stiffness only because it was a static case. In the dynamic case, as shown in Chapter 6, the contribution of the back surfaces is significant.

To sum up, the existing analytical model can only be used to qualitatively assess the influence of geometry on the energy of oscillations. The assumption that the flow impinges only on one side of the oscillator leads to errors up to 100%. In the next part of the study, the oscillator will no longer be immobilized.

7.2.2. Dynamic cases

The purpose of this study was first of all to find the optimal geometry of the oscillator and secondly to compare how existing analytical models hold against experimental data.

The following study bases on the assumption, that the current length of the stream divider is adequate. Its performance has been studied numerically. If it was shorter, it would fail to reorder the incoming flow profile and would not ensure a flat velocity distribution, increasing the susceptibility of the flowmeter to the inlet profile disturbances. If it was longer, a larger boundary layer would develop on its wall. As a result, the negative effect of Reynolds number on the linearity of the calibration curve would be increased.

Therefore with stream divider dimensions kept constant, a number of experiments were conducted for 3D-printed oscillators with α = [10°; 20°; 40°] , *b/D* = [9%; 12%; 15%; 18%;

21%], γ = [65°; 71°; 75°]. Three stream dividers were manufactured, which allowed specifying different location of the rotation axis. 43 cases were studied in total. Figure 7.8 shows exemplary modifications to the geometry. It can be noticed that z is a function of all the other parameters.

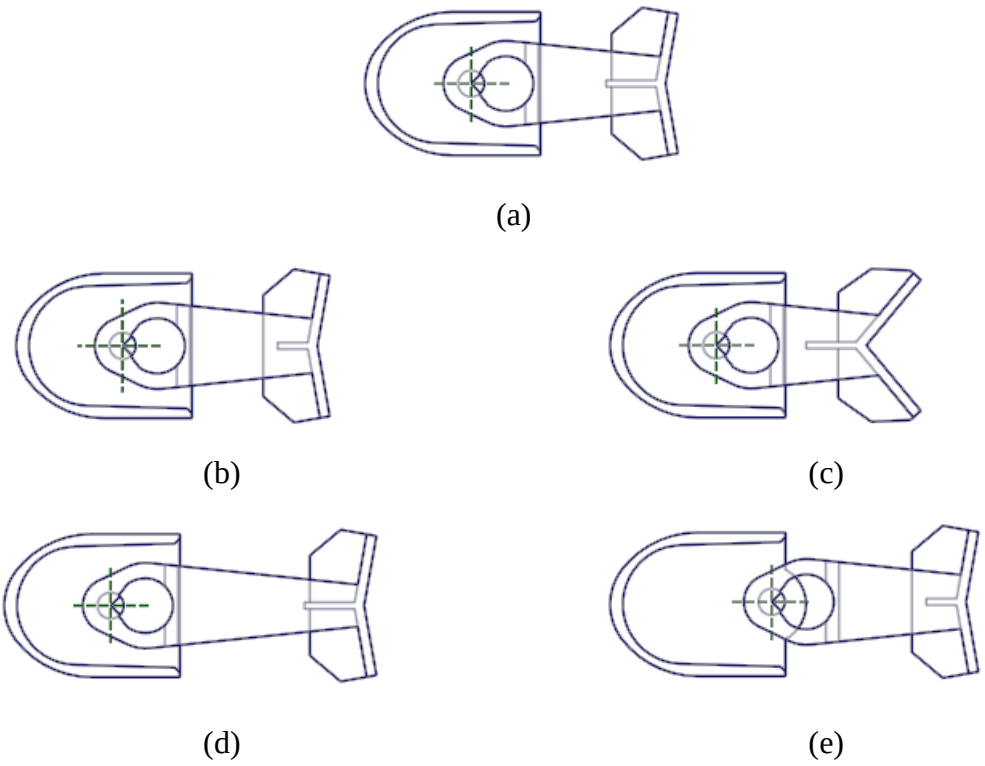

Figure 7.8: Introduced modifications to geometry. (a) Baseline case; (b) modified baffle height *b;* (c) modified angle *α;* (d) modified angle *γ;* (e) shifted rotation axis.

The moment of inertia I_o of each of the oscillators was determined and their frequency of oscillations for similar Reynolds number was captured. Then, the mechanical equivalent spring stiffness with respect to angle C_φ was calculated as:

$$C_\varphi = \left(2\pi f\right)^2 \cdot I_{tot} = \left(2\pi f\right)^2 \cdot I_o \left(1 + r\rho\right) \tag{7.11}$$

where I_{tot} is the total moment of inertia, which is the sum of the moment of inertia of the oscillator and the moment of inertia of the fluid that moves with the oscillator. Parameter r has the unit of m^3/kg and it describes the apparent mass of the oscillating fluid. Its value depends

on the oscillator geometry and it can be obtained by calibration with two fluids of different density. It will be discussed in detail in Chapter 9.1.

Under the assumption that torque τ acting on the oscillator varies linearly with the angular position of the oscillator φ, the following equation is valid:

$$\tau = C_{\varphi} \cdot \varphi \tag{7.12}$$

This assumption was demonstrated in the previous chapter to be reasonable. The total torque-position relationship was linear with a small hysteresis.

Nondimensional stiffness at the extreme depth of immersion of the oscillator into the stream x was then calculated as:

$$F = \frac{\tau}{\rho w^2 x h s} \tag{7.13}$$

The objective of the study was to determine the influence of geometry on the F function. It would be a tedious task to determine parameter r for each of the oscillators. For that reason, the experiments were conducted with air, at the bell prover calibration stand. This way because of relatively low density of air, $r\rho << 1$ and the influence of apparent mass could have been neglected without introducing significant error.

Figure 7.9 shows the influence of z/D on the nondimensional stiffness with other parameters kept constant. Clearly, a certain distance from the stream divider is required, approximately $z/D > 12\%$. If the distance is shorter than the threshold value, a lesser quantity of fluid exerts a torque on the baffle. Although the upper threshold of z/D was not found in the studied range, it is certainly limited by the stability of the flow profile conditioned by the stream divider. Figure 7.10 pictures axial velocity distributions in the symmetry plane at various distances downstream the stream divider.

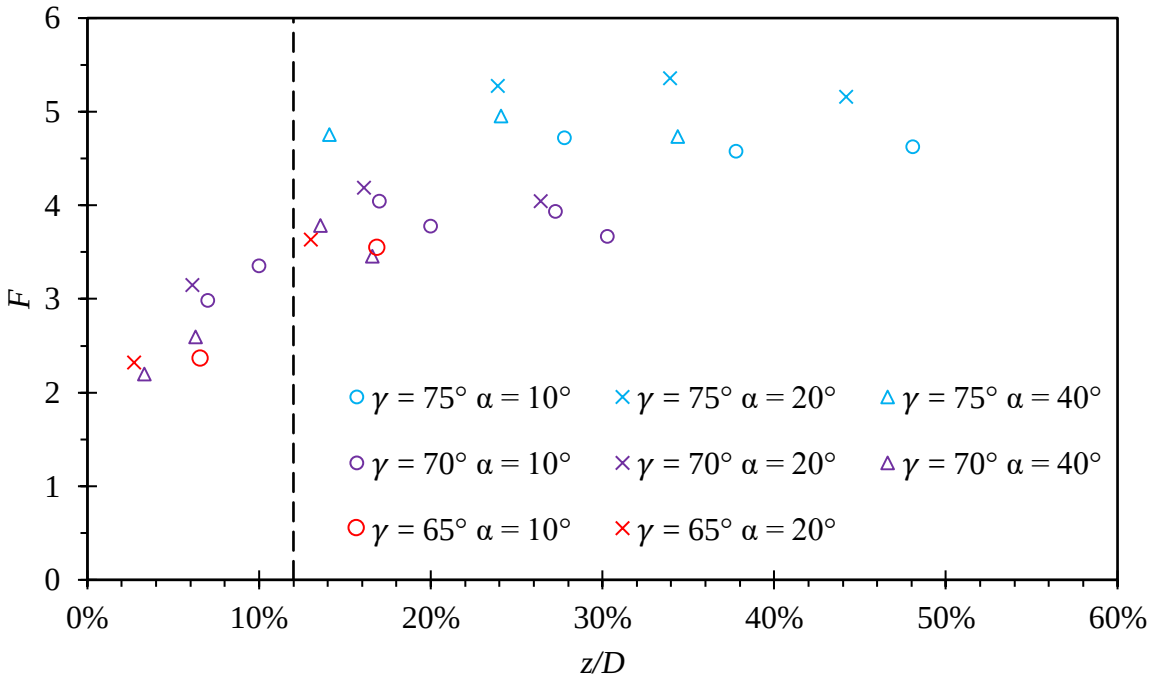

Figure 7.9: Nondimensional stiffness vs distance from the stream divider, *b/D* = 15%. The dashed line marks the threshold *z/D* value, above which no correlation between *F* and *z/D* was observed.

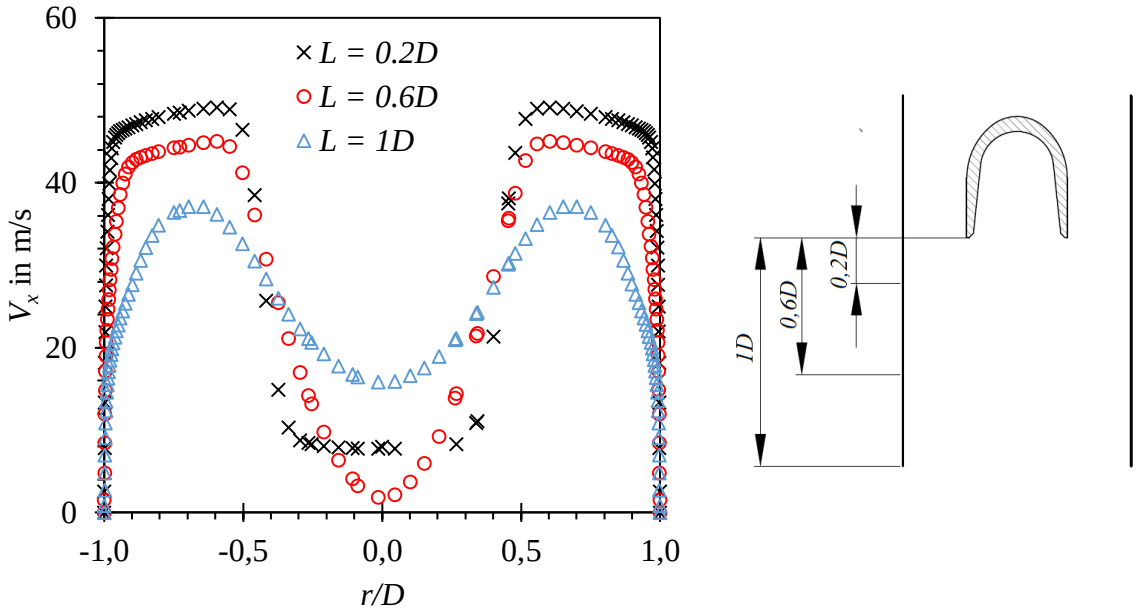

Figure 7.10: Axial velocity distribution in the symmetry plane at the distance *L* behind the flow divider. CFD, simulation for air inflowing at *Re* = 70 000.

The effect of α and γ, which is shown in Figure 7.11, is qualitatively comparable to predictions of the analytical model (Turkowski, 2003c) and of steady-state CFD simulations. Although the dynamic flow structure is decidedly more complex than described by the theoretical model, most of the conclusions remain valid. The difference between nondimensional stiffnesses F measured for plastic and steel oscillators of the same geometry was within the measurement uncertainty. It was an expected result, as F depends only on the geometry, not on the mass properties of the oscillator.

The obtained results suggest that the support should be as long as possible, as increasing γ has the largest influence over F. The upper threshold is set by bearings, which may skew if the oscillator would be too long, and in the result - too heavy. The conducted study drew attention also to the other limitation, which is the stability of the flow profile conditioned by the stream divider. In that case, it is not recommended to increase the value of γ above 75°, even with lightweight 3D-printed oscillators.

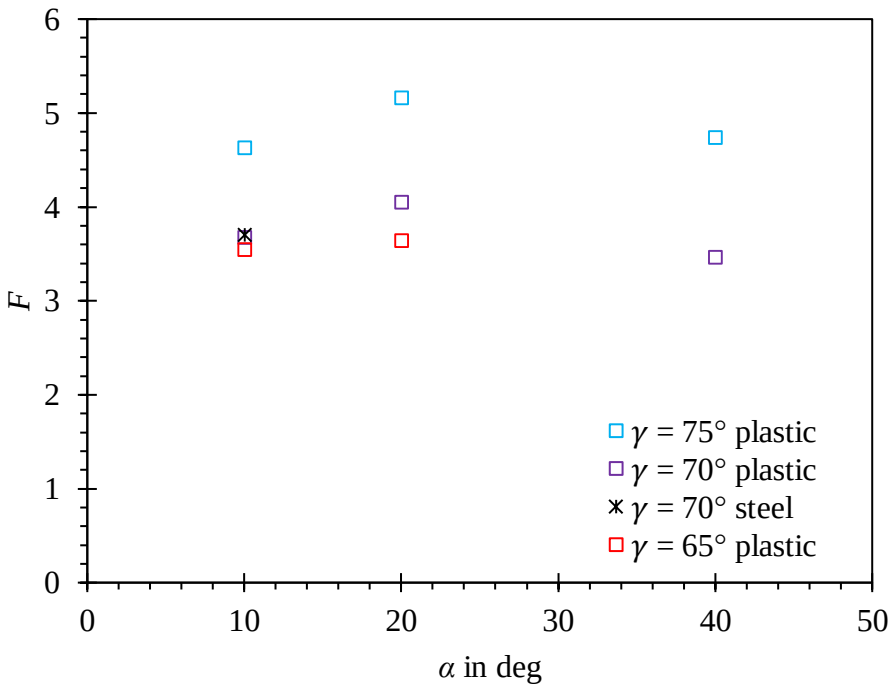

Figure 7.11: Experimentally obtained values of nondimensional stiffness F in the function of angles α, γ for baffle height $b = 0{,}15D$.

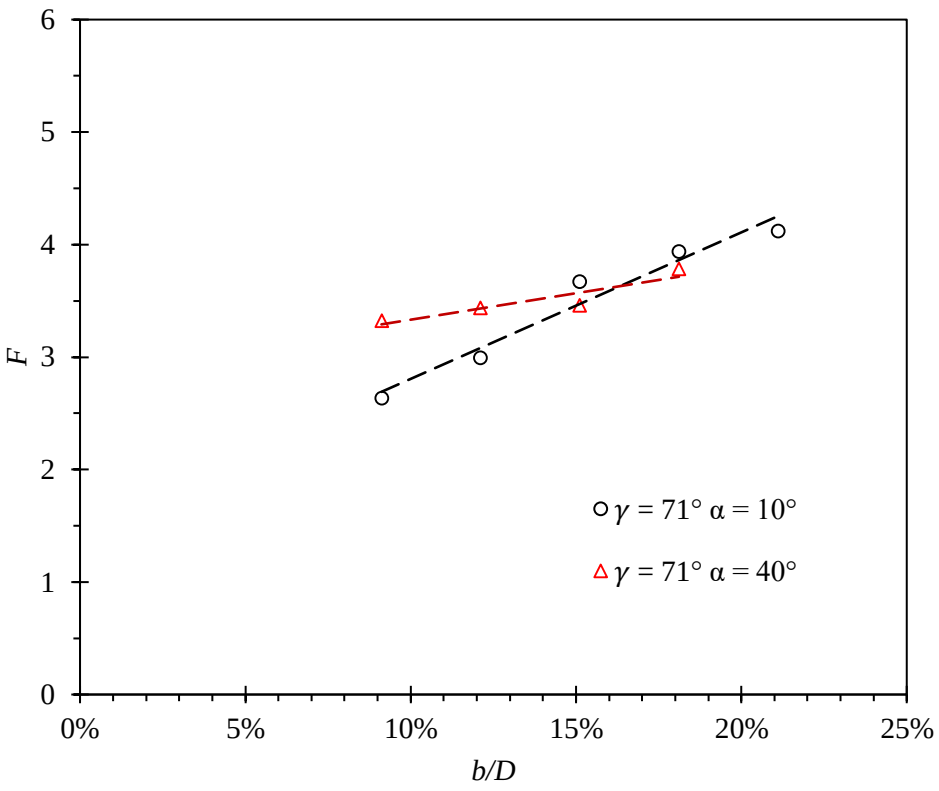

Figure 7.12: Nondimensional stiffness vs baffle height. The influence of baffle height is smaller for increasing α.

Steady-state analyses demonstrated that the baffle should be as long as possible, but a certain required distance *z/D* has to be maintained. In transient operation, the baffle introduces damping of the oscillator's motion. The amount of damping depends among others on the baffle height and the density of the fluid. In the case of air, damping forces were small enough so that *F* grew with baffle height in the whole studied range (Figure 7.12). Because (Turkowski, 2003c) discovered that increasing *b/D* above 20% resulted in unstable oscillations, oscillators with higher baffles were not studied. In accordance with a static numerical model, the influence of baffle height was smaller for larger α values.

The study presented above concerned modifying dimensions of the oscillator. One more study has been conducted where modifications where more prominent. The motivation was that the analysis of forces acting on the oscillator presented in Chapter 6.1 showed that the main damping torque component originates from the back surface. If the damping torque was reduced, then the nondimensional stiffness would increase, which is desirable. The concept is shown in Figure 7.13a. After modifications, the back surface forms a circular arc which center is aligned with the rotation axis. In that case, pressure distribution on the back surface does not

introduce torque about the rotation axis. This potentially increases the derivative of the total torque with respect to the angular position, which would mean higher stiffness of "fluidic springs" and larger energy of oscillations. Two-dimensional numerical analysis has shown that the modification worked as expected. The torque originating from back surfaces dropped almost to zero and only a small component from the viscous forces remained Figure 7.13b. The total torque in the extreme positions of the oscillator was twice as large as in the baseline case (Figure 7.13c), which was a desired result.

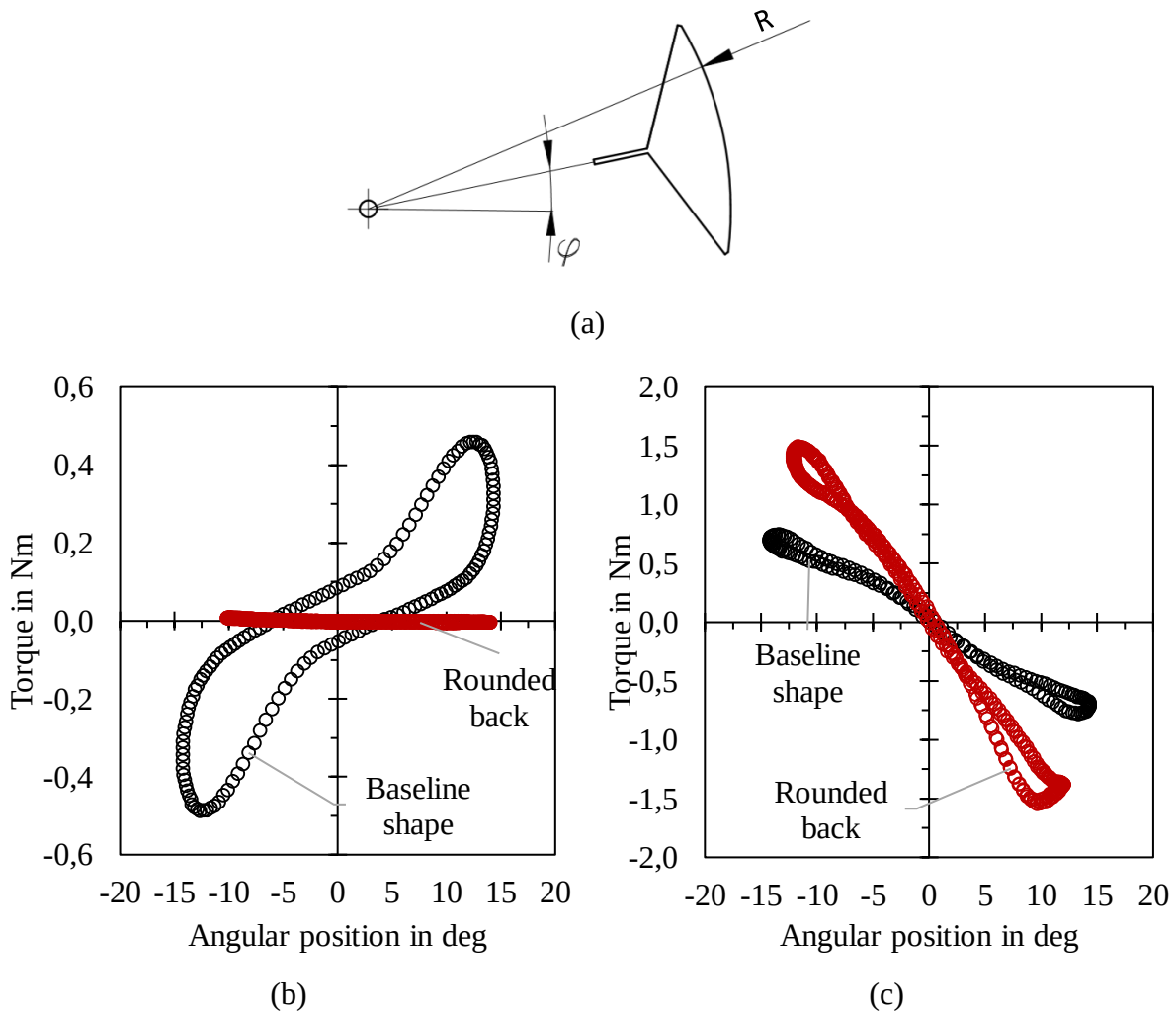

Figure 7.13: (a) Oscillator with a rounded back surface to reduce the damping torque generated by pressure forces; (b) torque acting on the back surface of the oscillator vs angular position for one oscillation cycle, two-dimensional CFD model; (c) total torque vs angular position for one oscillation cycle, two-dimensional CFD model.

A prototype oscillator of such a shape was manufactured. However, an experimental study has shown that without the damping action of the back surface the oscillation amplitude grew extensively and the oscillator was hitting pipe walls. This had a largely negative effect on the metrological properties.

To sum up, existing analytical models, steady-state analyses with an immobilized oscillator and fully transient analyses all show the same geometry modification directions when it comes to maximizing the nondimensional stiffness. The exact values of the nondimensional stiffness can only be obtained with transient analyses. The analytical model leads to errors of up to 100% and steady-state CFD leads to errors of up to 30%.

It was confirmed that the angle γ has the decisive impact over the energy of oscillations. The unique finding of this chapter is the previously unnoted role of the distance z on the nondimensional stiffness, which is one of the factors that limits the value of angle γ.

It was also found that if the nondimensional stiffness is too large, then the amplitude of oscillations may rise to such an extent that the oscillator is hitting the pipe walls. It impacts the performance of the flowmeter negatively.

Now the important question arises whether increasing the nondimensional stiffness is justified. The following chapter verified if metrological and operational properties could benefit from increased nondimensional stiffness.

7.3 The positive effects of increased energy of the oscillations

The hypothesis is that geometries that correspond to larger nondimensional stiffness F are less susceptible to external disturbances. The first example studies the flowmeter in a vertical configuration, flow upwards. In such an installation attitude, torque from the gravitational force τ_g decreases the torque from the fluid action. Assuming small angles φ, the torque from gravity equals:

$$\tau_g = mg\varphi x_{CG} \tag{7.14}$$

where m is oscillator's mass, g is the gravitational acceleration and x_{CG} is the distance between the oscillator's center of gravity and its axis of rotation (Figure 7.14). Let us differentiate τ_g by φ and introduce it in into the simplified equation describing oscillation frequency:

$$f_{ver} = \frac{1}{2\pi}\sqrt{\frac{C_\varphi - mgx_{CG}}{I_o(1+r\rho)}} \tag{7.15}$$

The shift in the frequency of oscillations caused by the modified flowmeter attitude can be expressed by the formula:

$$\frac{f_{ver}}{f_{hor}} = \sqrt{\frac{C_\varphi - mgx_{CG}}{C_\varphi}} \tag{7.16}$$

where f_{ver} and f_{hor} are frequencies for the vertical and horizontal case, respectively.

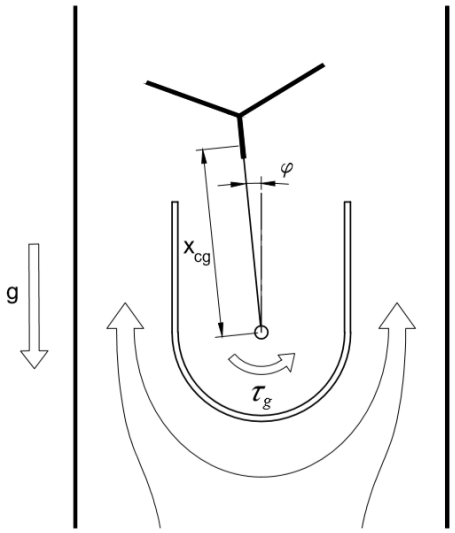

Figure 7.14: Torque resulting from the gravitational force in the case of a vertical attitude of the flowmeter, flow upwards.

While the equivalent spring stiffness C_φ is proportional to the square of the volumetric flow rate, the effect of gravity is independent of the flow rate. For that reason, gravity effects are important only up to a certain flow rate. Indeed, (Turkowski, 2003b) showed on the example of DN 65 flowmeter, that in the range of large flow rates, the flow can be vertical or horizontal without affecting performance. This work focused on small flow rates, where the influence of installation of the flowmeters was noticeable.

The study was conducted for two oscillators, which parameters are collected in Table 7.1. Their error curve was at first measured in a standard, horizontal configuration. Then, flowmeters were installed in a vertical configuration, flow upwards, and error curves were measured once again.

Table 7.1: Parameters of oscillators selected for the study of the influence of external disturbances.

γ in deg	α in deg	b/D	z/D	F	I_o in kg·m^2	m in g	x_{CG} in mm	mgx_{CG} in Nm
75	20	0,15	0,44	5,16	$3{,}72\cdot10^{-6}$	4,11	38,84	$1{,}6\cdot10^{-3}$
65	10	0,15	0,07	2,36	$1{,}28\cdot10^{-6}$	3,78	15,77	$5{,}9\cdot10^{-4}$

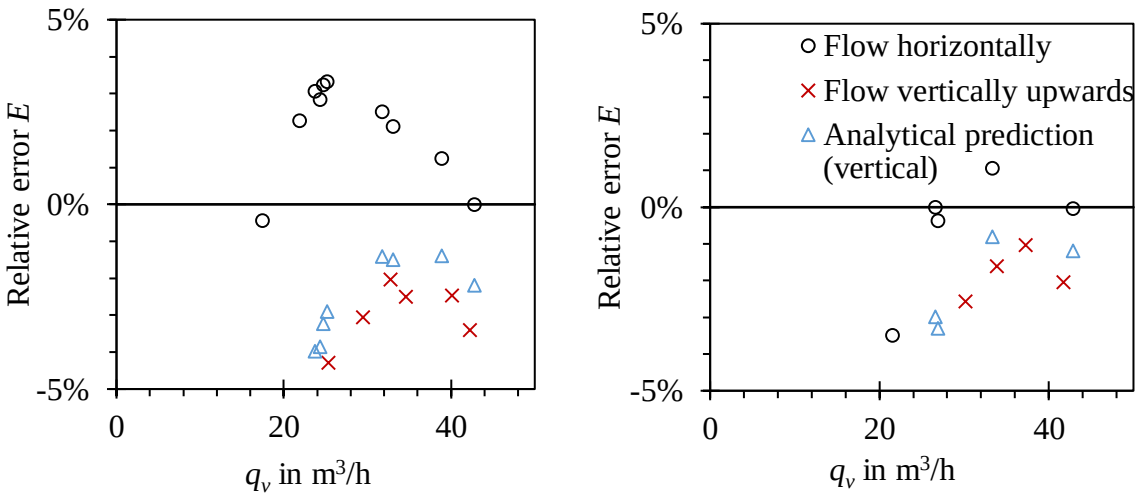

Figure 7.15: Error curves for low flow rates, influence of the flowmeter attitude. (a) F = 5,15 oscillator; (b) F = 2,36 oscillator.

Figure 7.15 presents the measured data together with an analytical prediction calculated from eq. (7.16). The results show that the model is qualitatively correct. At first, it may be counterintuitive that the shift of the error curve for the F = 5,16 was higher than for the oscillator with F = 2,36. It comes from the fact that the F = 2,36 oscillator was shorter and lighter to such an extent, that the ratio of torques due to gravity (1,6 : 0,59 ≈ 2,7) exceeded the ratio of F (5,16 : 2,36 ≈ 2,2).

This means that even though the oscillator has a higher nondimensional stiffness, it still may be more susceptible to installation attitude, as the torque from gravity depends on mass properties. Because the analytical prediction agrees with the obtained results, one can assume that if two oscillator of similar mass but different F were compared, then the oscillator with higher F would be less susceptible to the installation attitude.

The second example considers a disturbance source that does not scale with mass properties, i.e. bearing friction for a horizontally-mounted flowmeter.

Bearing friction limits the threshold volumetric flow rate, above which the oscillator starts to operate in a limit cycle. An experiment was conducted at the bell prover calibration stand, where multiple oscillators of various F values but with the same bearings were tested in a horizontal configuration. Results show that the threshold volumetric flow rate depends approximately linearly on F (Figure 7.16).

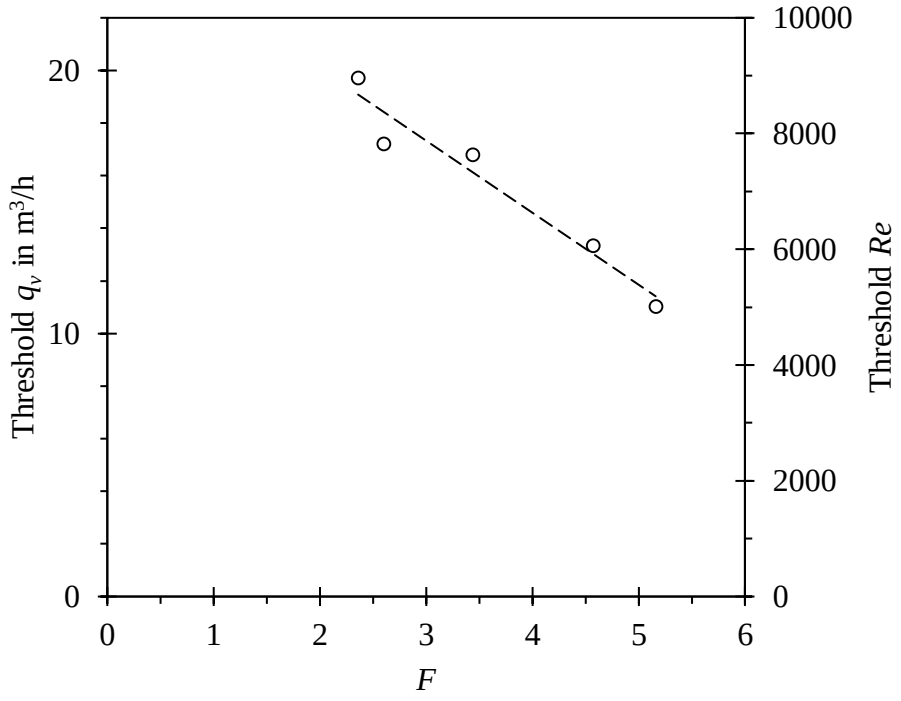

Figure 7.16: Threshold volumetric flow rate and its equivalent Reynolds number vs nondimensional stiffness.

Experiments confirmed that maximizing the nondimensional stiffness F is justified. They lower the threshold flow rate and it can be assumed that they reduce the influence of bearing wear. With the oscillators of higher F it may be possible to apply other bearing types than knife-edge, with further desirable properties, but larger frictional torques. The next subchapter of the thesis presents data that allows selecting proper bearings and proposes a methodology that can be utilized for durability tests.

7.4 Bearing wear

7.4.1. Introduction

The mechanical oscillator flowmeter utilizes knife-edge bearings, which provide the smallest friction torques of all the available options.

The durability of the oscillator bearings is the weak point of the flowmeter. The bearing material should be on the one hand resistant to corrosion and on the other hand resistant to wear. Meeting both conditions is problematic, e.g. austenitic steel is resistant to corrosion but has a rather low hardness. Today there are numerous methods of surface hardening available, such as cold hardening, dispersion hardening, carburizing, ion implementation or ceramics coating.

The other factor is the nominal shape of the bearing. At the early stages of the manufacturing process in the ’90s, bearing components were made as sharp as possible. As a result, the wear rate was fast and shifts in the error curve of ca. 1,5% were experienced. On the other hand, increasing radiuses caused increased friction and caused extensive bearing looseness, which finally caused jamming of the oscillator in extreme angular positions. Therefore it was a compromise between the stability of the error curve and increased friction combined with occasional jamming.

Based on the findings in the thesis, two solutions to mitigate the negative effects of increased radiuses of bearing components are proposed.

First of all, as the linear oscillation amplitude x/D is constant regardless of the support length, increasing the support length (increasing γ) reduces the angular amplitude of motion. In effect, this reduces the probability of jamming, which occurs only for large angles, above 10°.

Secondly, an oscillator with large nondimensional stiffness F is less sensitive to increased bearing friction.

To investigate the effectiveness of fillet radiuses, different materials, surface treatment and hardening methods, an objective and repeatable durability test must be prepared. Ideally, the flowmeter would be installed in the pipeline where flow conditions are monitored and controlled. Measurement of metrological characteristics and dimensions of bearing elements would be done before and after a set working period. However, such a method would be costly. If the flowmeter was installed in a real industrial installation, then there would be little control over flow conditions and potential overloads.

Instead, a test bench was prepared which allows for controlled testing of various flowmeter designs. Actual durability tests were not a subject of the presented study, as manufacturing possibilities were limited.

7.4.2. Constructed test stand

The author set up a test bench shown in Figure 7.17. The oscillator together with the flow divider is mounted in a grip. DC motor forces movement of the oscillator. Axial and lateral forces are provided by three appropriately selected springs.

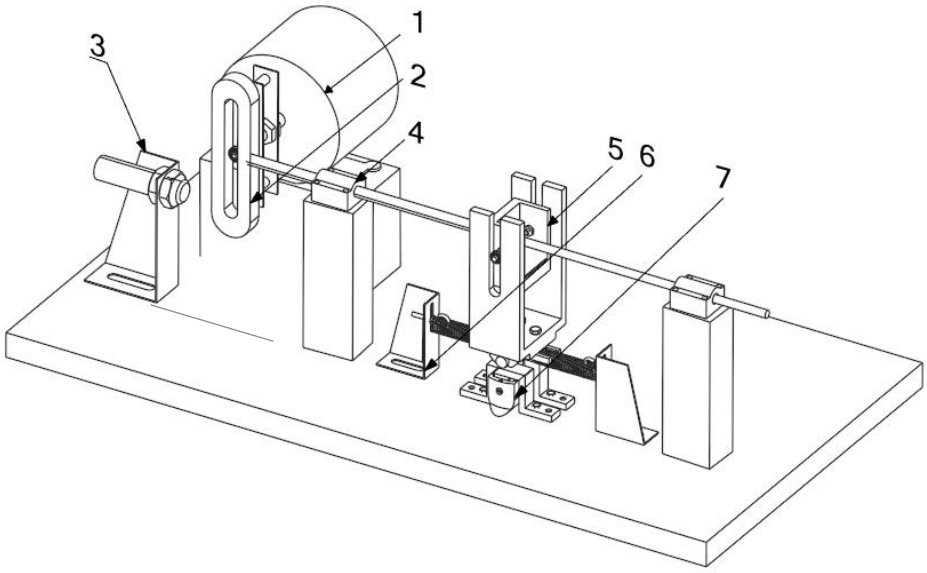

Figure 7.17: Schematic drawing of a test stand for bearing durability tests. 1 – DC motor, 2 – regulation of oscillation amplitude, 3 – inductive sensor to count the number of cycles, 4 – linear bearing, 5 – the grip of the main spring, 6 – grips of auxiliary springs, 7 – oscillator with a stream divider mounted in a grip.

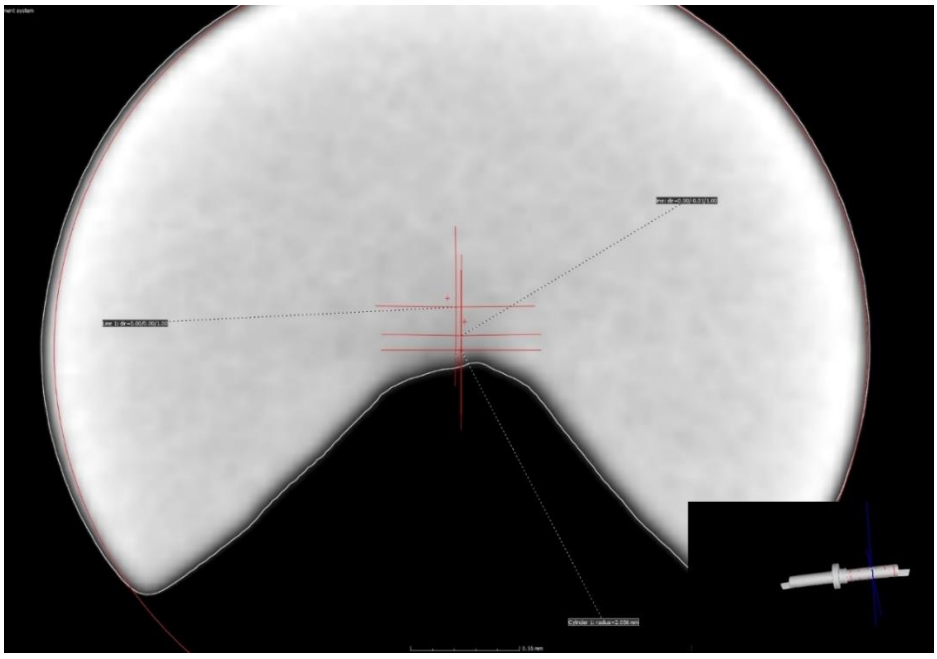

Figure 7.18: Computed tomography results – a pan of the knife-edge bearing.

The constructed stand allows setting a controlled number of cycles with selected amplitude and spring load. Spring selection is based on the loads obtained from the CFD model, which are cited in the next subchapter. Because the oscillator does not have to be dismantled from the stream divider for the study, installation effects do not apply and it is possible to capture the influence of bearing wear on the error curve accurately.

The idea is that the error curve of the flowmeter is first captured on a precise calibration stand and then captured again after undergoing a set number of cycles on the durability test stand. Such a study is planned to be conducted by the author in the future. It was verified that computed tomography allows capturing bearing geometry in detail (Figure 7.18) and can be used to give even more information on the bearing wear.

7.4.3. Quantification of forces acting on the oscillator

The durability study would not be possible without the knowledge of forces acting on the oscillator. CFD analysis has shown that force in the direction of the flow F_x exhibits small variation throughout the larger part of the motion and it drops as the extreme angular positions are reached (Figure 7.19a). This may be counterintuitive, one would think that in the neutral position the axial force should be the smallest as the oscillator is hidden behind the stream divider. In reality, the stream lines bend and the flow impinges on the oscillator even when it is in the neutral position (Figure 6.3). In the extreme positions the flow velocity impinging on the oscillator is reduced (Figure 6.2), which explains the character of $F_x(\varphi)$ relationship.

Force in the perpendicular direction F_y changes linearly in the function of the angular position.

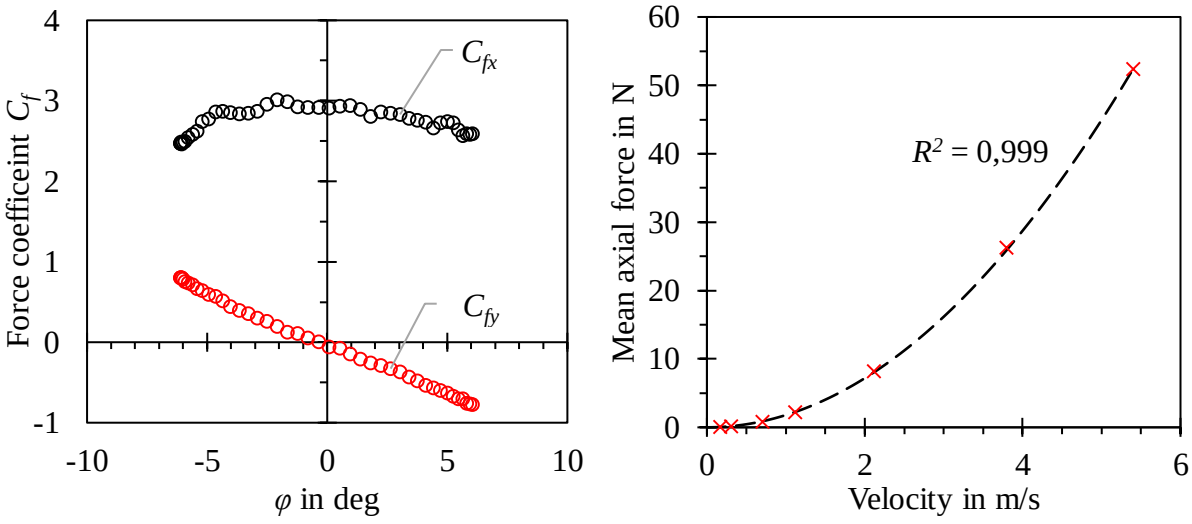

(a) (b)

Figure 7.19: (a) Force coefficient acting on the oscillator vs position; (b) mean axial force vs fluid velocity, simulation results for water (red marks) and the fit from eq. (7.17) for $\overline{c_{fx}}$ = 2,792 (black dashed line).

To estimate forces acting on the oscillator for the durability studies, an approximate equation for the mean axial force was introduced. It is given by the formula:

$$\overline{F_x} \approx \overline{c_{fx}} \cdot hs \cdot \frac{\rho v^2}{2} \tag{7.17}$$

where $\overline{c_{fx}}$ is the mean value of the axial force coefficient from the oscillation cycle, h is the oscillator's height, s is the oscillator's width, ρ is the density of the fluid and v is the fluid velocity.

It was verified that the equation is valid for various velocities. The equation (7.17) is plotted against simulation data in Figure 7.19b. The relative difference between the simulation data and the approximating curve is below 2% for velocities larger than 1 m/s.

7.4.4. Summary

The collected data and the constructed test stand will allow conducting future studies on the durability of bearings. It was not in scope of the present work, as it requires a huge investment in manufacturing equipment.

Chapter 8

Installation constraints

8.1 Inlet flow disturbance effects

8.1.1 Introduction

Ideally, the flow profile is defined by Reynolds number and the condition of the inside wall of the piping described by its roughness. In industrial applications, a velocity profile is often disturbed by such elements as elbows, valves, expanders or reducers. A straight pipe of a certain length is then required for the flow profile to be restored by the mixing action of the moving fluid. During calibration at test stands efforts are made to ensure that the incoming velocity profile is fully developed. Deviation from calibration conditions results in a measurement error, which value depends on disturbance type, flowmeter type and the length of straight pipe upstream and downstream of the flowmeter. Usually, required lengths exceed an available installation space. Recommendations on straight pipe lengths for various flowmeter types are mostly a result of extensive experiments (Yeh, 1991; Morrison, Deotte and Beam, 1992; Carlander and Delsing, 2000; Pochwała, Kabaciński and Pospolita, 2012; Pochwala and Pospolita, 2016), although in some cases analytical models can be introduced (Dobrowolski and Kabza, 1992). This topic has also been successfully investigated with the use of CFD, e.g. for swirl V-cone flowmeters (Singh, Singh and Seshadri, 2009) and ultrasonic flowmeters (Hilgenstock and Ernst, 1996; Zhao and Peng, 2014).

Axisymmetric deformations generated by low-angle expanders and reducers are the least problematic. They result in extending or flattening of the velocity profile, respectively. Asymmetric deformations, shown in Figure 8.1a, c and d, are harder to eliminate. They are introduced by bends, tee junctions, and quickly expanding pipes. Finally, two bends in perpendicular planes introduce a swirling motion (Figure 8.1e), which does not fully decay even after straight pipe length L/D = 45. In industrial applications, the situation is even worse, as disturbances are generated by multiple elements successively. In such cases, the resultant velocity profile is hard to predict. Individual types of flowmeters are insensitive to the velocity profile, e.g. Coriolis flowmeters. Unfortunately, this is not the case for mechanical oscillator flowmeters - their performance depends on the inlet flow profile.

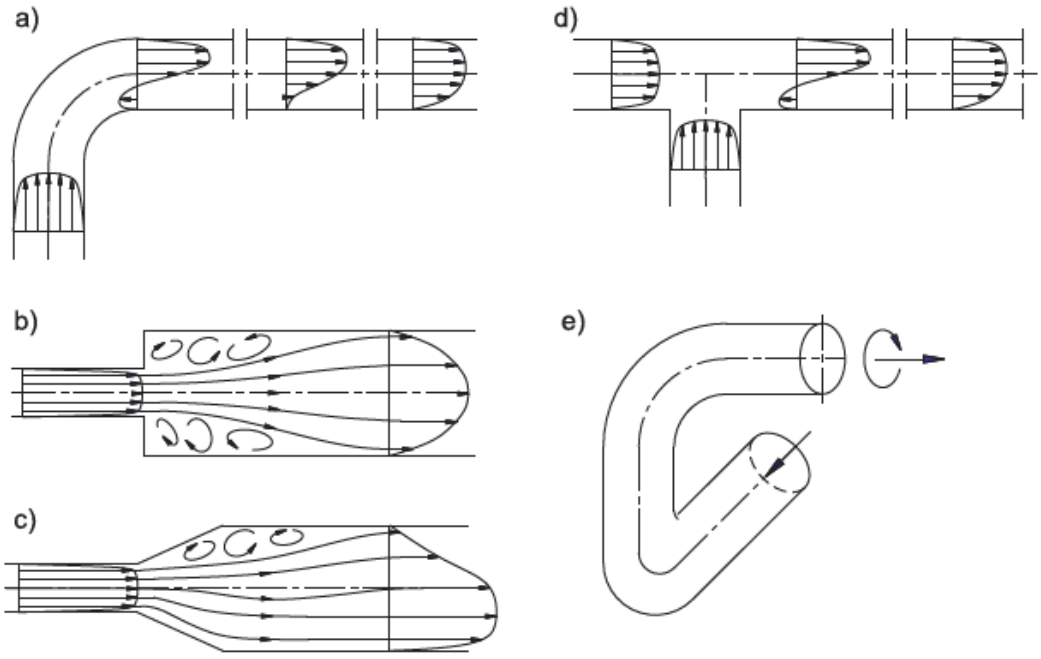

Figure 8.1: The effect of various fittings on velocity profile. (a) Single 90° bend; (b) sharp-edged pipe expansion; (c) quickly expanding pipe; (d) tee junction; (e) two bends in perpendicular planes (Turkowski, 1987a).

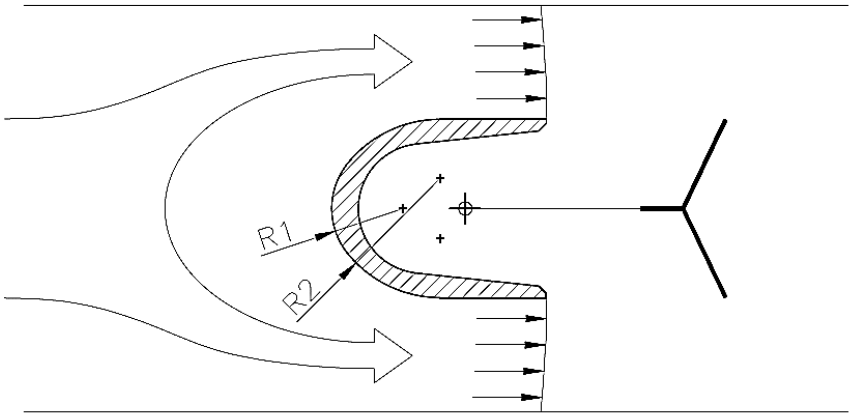

Figure 8.2: Stream divider of the studied mechanical oscillator flowmeter.

The susceptibility of mechanical oscillator flowmeter to inlet profile disturbances depends mostly on the shape of the stream divider. In the studied case its shape is described by two arcs, where a smaller radius blends into a larger (Figure 8.2), similarly as in normalized ISA nozzle (International Organization for Standardization, 2003c).

The only available data in the topic of required straight lengths concerning mechanical oscillator flowmeters was an initial study presented by (Turkowski, 2003b). It was conducted for DN50 flowmeter with the shape of the stream divider as in Figure 8.2. The study was limited to disturbances in the form of a butterfly valve, a ball valve, a DN65/50 reducing pipe, and a swirl generated by an immobilized turbine. One of the conclusions was that piping downstream the flowmeter is of lesser importance and a 3*D* outlet section is sufficient. In the case of the upstream section, recommendations were given for disturbances divided into three categories shown in Table 8.1. They concern the distance *L* between a disturbance and a flowmeter, marked in Figure 8.3.

Table 8.1: Installation recommendations stated in (Turkowski, 2003b).

No.	Category	Examples	Recommendation
1	Symmetrically oriented disturbances	Expanding pipe, single bend, valve	10*D*
2	Asymmetrically oriented disturbances	Valve, single bend	15*D*
3	Disturbances introducing swirl	Two elbows in perpendicular planes	20*D*

Some of the elements may be installed twofold, as shown in Figure 8.3. In a way that the asymmetry of the flow introduces a difference in flow rates between channels of the stream divider, or in a way that flow rate between channels of the stream divider remains equal. If the elbow is oriented in the perpendicular plane to the stream divider and therefore the symmetry between channels is disrupted, longer inlet straight runs of at least 15*D* are recommended.

Present recommendations are general, but they are extrapolated from a small data set. Therefore they should be used with caution and ideally they should be extended. What is more, the existing studies were limited to inlet pipe lengths of 12*D*. Finally, disturbances generating swirl were only studied on the example of an immobilized turbine with an average blade incidence angle of 45° with piping upstream the flowmeter up to just 11*D*. Disturbances in form of two elbows in perpendicular planes, which are commonly found in the industry, generate a swirl of much smaller angle in the range of (10 – 20)° (Merzkirch *et al.*, 2005).

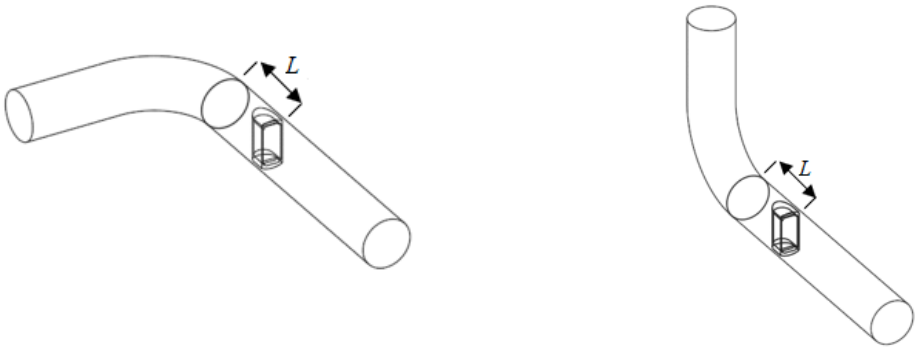

(a) (b)

Figure 8.3: An example of asymmetrically (a) and symmetrically (b) oriented disturbance relative to the stream divider.

The literature review underlines the complexity of the issue, which has not been adequately resolved for mechanical oscillator flowmeters. The goal of the work presented in this chapter was to extend the study to a larger number of disturbances. Additionally, the usefulness of CFD for that application was studied and the possibility of reducing the required inlet runs by flow straighteners was verified.

8.1.2. Methods

The experiments were conducted at the low-pressure air calibration stand described in Chapter 4.3. First, a baseline error curve and a calibration constant K_b were determined for a DN50 flowmeter with the inlet pipe length of 45*D*. Next, disturbances were introduced upstream of the flowmeter and resultant calibration constants K_i were captured. Comparisons between cases were made for similar values of Reynolds number of ca. 70 000:

$$E_{inst} = \frac{K_i - K_b}{K_b} \tag{8.1}$$

Installation errors E_{inst} were considered insignificant if they were in limits of 95% confidence interval, which was calculated basing on the calibration stand measurement uncertainty increased by the repeatability of the flowmeter. The applied methodology and criterion for the significance of installation errors are the same as in the case of the development of standards for orifices (Studzinski *et al.*, 1997).

All of the elbows had a ratio of radius to diameter R/D = 1,5. Following piping sets were studied:

1) One 90° elbow, oriented symmetrically to the stream divider
2) One 90° elbow, oriented asymmetrically to the stream divider
3) Two 90° elbows in perpendicular planes
4) Two 90° elbows in a single plane oriented symmetrically to the stream divider
5) Two 90° elbows in a single plane oriented asymmetrically to the stream divider

Steady-state CFD simulations were conducted for disturbances 1–3. Velocity profiles generated by disturbances were obtained in separate simulations (Figure 8.4) and then set at the inlet of a domain that included the geometry of a stream divider (Figure 8.5). The oscillator was not included to reduce the computational expense. It was verified that its presence does not affect the observed quantities. The applied computational mesh was of the same structure and had the same characteristic element size (h = 0,7 mm) as the mesh selected in the mesh independence study in Chapter 5.4.

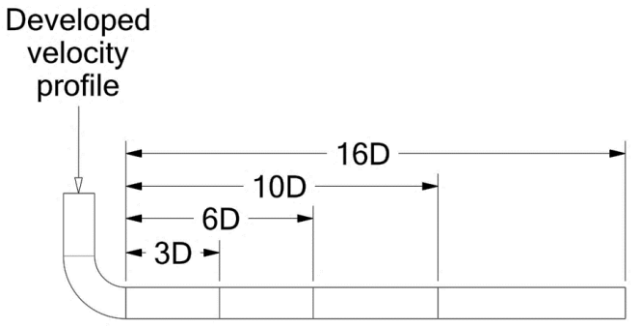

Figure 8.4: Computational domain on the example of a single elbow. Velocity profiles were captured at x = [0, 3, 6, 10, 16]D.

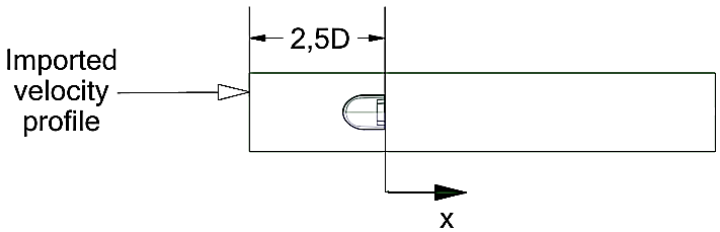

Figure 8.5: Computational domain of the stream divider.

The main goal of numerical analyses was to capture and evaluate velocity distributions in the plane located at the rear edge of the stream divider (x = 0 in Figure 8.5), and then to relate

them to installation errors. Parameters chosen for evaluation were Coriolis coefficient C_c, flatness parameter C_f and momentum of flatness parameter C_{fm}, which were proven to be sensitive to the studied type of disturbances (Turkowski and Szufleński, 2013):

$$C_f = \frac{\iint_A \left(v_x^{\,2} - v_{xref}^{\,2} \right) dA}{\overline{v_x}^{\,2} A} \tag{8.2}$$

$$C_{fm} = \frac{\iint_A \left(v_x^{\,2} - v_{xref}^{\,2} \right) r dA}{\overline{v_x}^{\,2} \pi R^3} \tag{8.3}$$

where $v_{x\,ref}$ is the reference velocity profile obtained for the case with no disturbances present. To evaluate swirling flows a swirl number S_n (Miau *et al.*, 2002) together with swirl angle S_a (SAE, 2017) were used:

$$S_n = \frac{\iint_A v_x v_\Theta r^2 dA}{R \iint_A v_x^{\,2} r dA} \tag{8.4}$$

$$S_a = \tan^{-1}\left(\frac{V_\theta}{V_z} \right) \tag{8.5}$$

8.1.3. Results and discussion

According to the collected data, if one would ignore deformations of the inlet velocity profile, installation errors up to 5% would be introduced. In the case of elbows oriented symmetrically to the stream divider (Figure 8.7), the installation errors are insignificant if the inlet pipe length is greater than 12,5*D*. The same conclusion is reached for elbows in the same plane oriented asymmetrically to the stream divider (Figure 8.10). The influence of swirl introduced by two elbows in different planes leads to significant installation errors if the inlet pipe length is shorter than 18,5*D* (Figure 8.10).

CFD simulations confirmed how effective the current stream divider's shape is in reordering the velocity profile. Installation errors decay quickly, just after 5,5*D* of pipe length none of them exceeds 1,5%. This is because flow development in channels follows a large contraction. Axial velocity contours demonstrate almost flat velocity profiles in the plane at the rear edge of the stream divider (Figure 8.12, Figure 8.14), regardless of disturbance proximity.

For that reason values of Coriolis coefficients at the rear edge of the stream divider are the same regardless of disturbance source proximity, as shown in Figure 8.6.

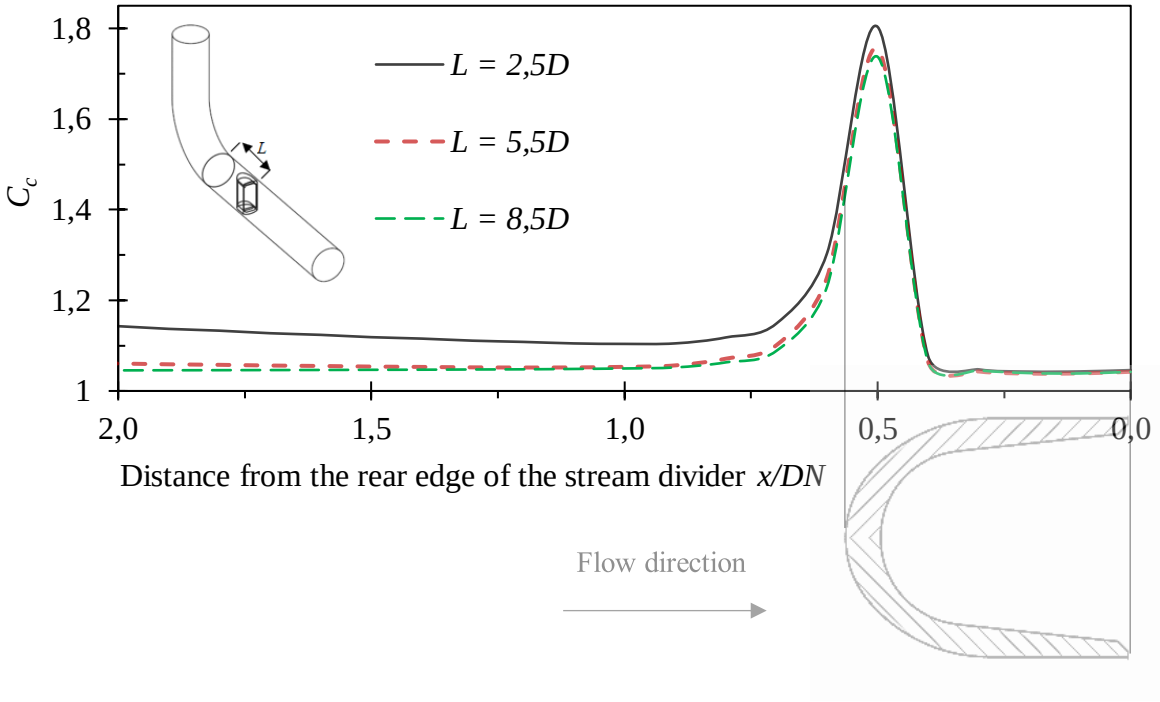

Figure 8.6: Coriolis coefficient vs distance from the rear edge of the stream divider for various upstream pipe lengths. Influence of a single 90° elbow oriented symmetrically to the stream divider. Same values of Coriolis coefficient at $x/DN = 0$ for all series are observed.

Parameters C_f and C_{fm} compare the studied case to the baseline case and therefore their sensitivity is higher. The values of C_f in the function of upstream pipe length shown in Figure 8.8 correspond to installation errors presented in Figure 8.7 well.

At the rear edge of the stream divider, additional radial and circumferential velocity components appear (Figure 8.13, Figure 8.15). Flow structures introduced by disturbances fade out quickly in function of the inlet pipe length L.

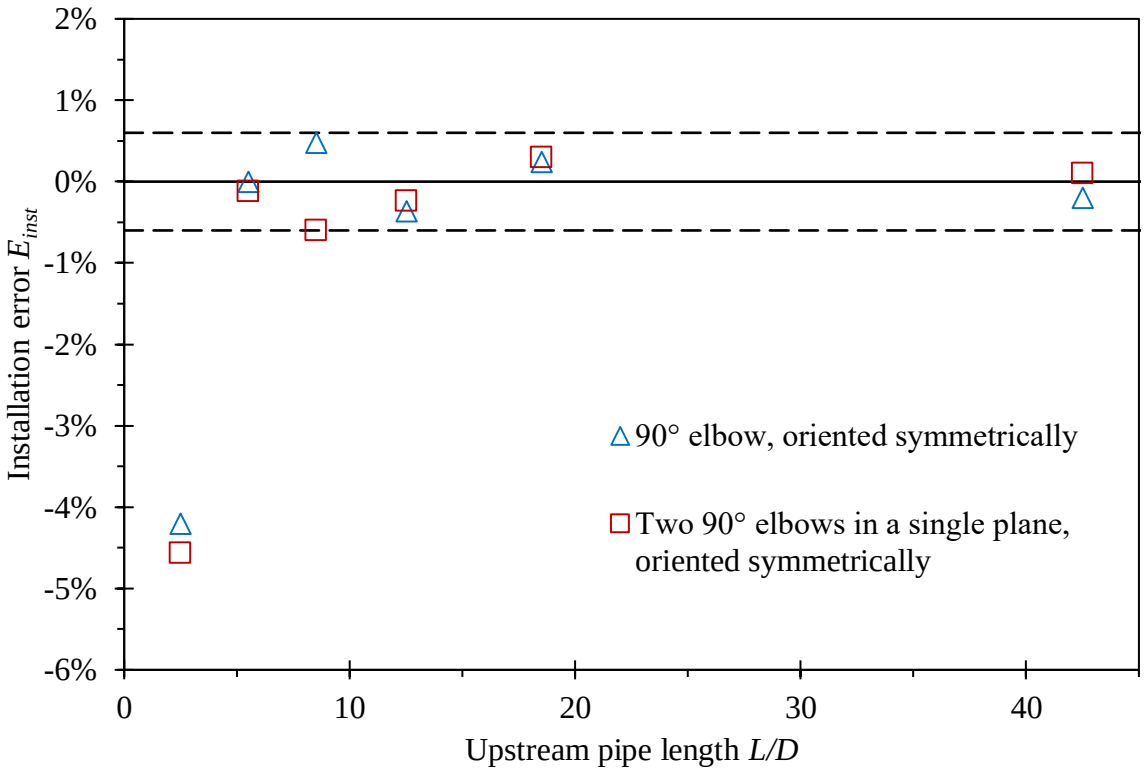

Figure 8.7: Installation errors vs inlet pipe length for symmetrically oriented disturbances. Grey dashed lines denote the sum of flowmeter repeatability and the uncertainty of the measurement stand (*k = 2)*.

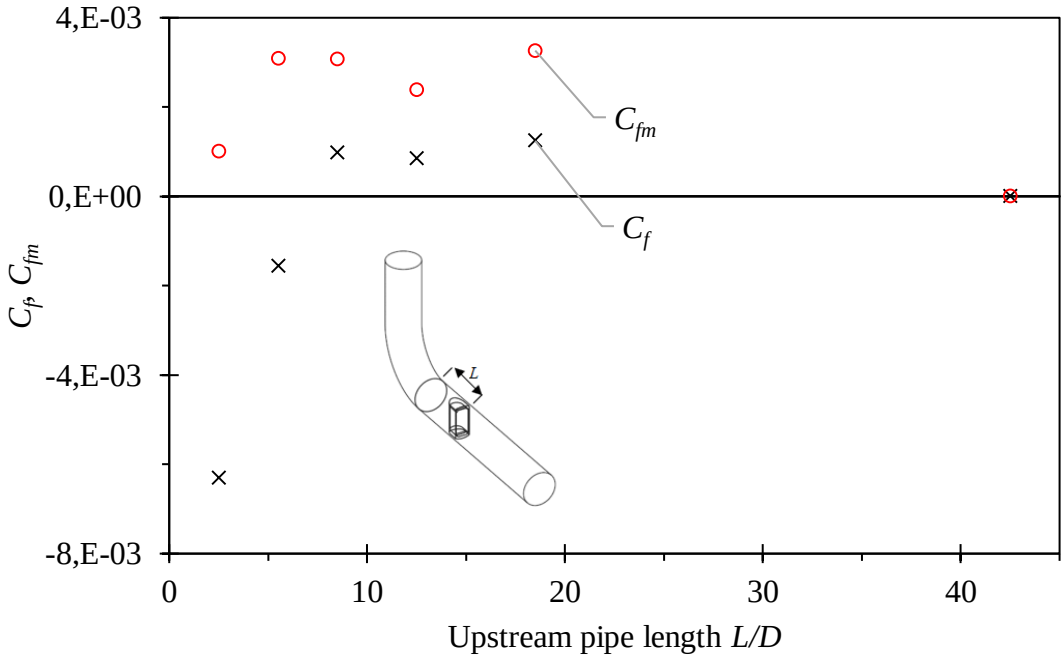

Figure 8.8: Flatness parameter and momentum of flatness parameter measured in the plane at the rear edge of the stream divider vs pipe length after a single 90° elbow oriented symmetrically.

In the case of disturbances introducing swirl, the effects are noted even with the inlet pipe of length 12,5*D*, as shown in Figure 8.9. Two elbows generated swirl angle of 10°, which decreases down to (1 – 2)° at the rear edge of the stream divider.

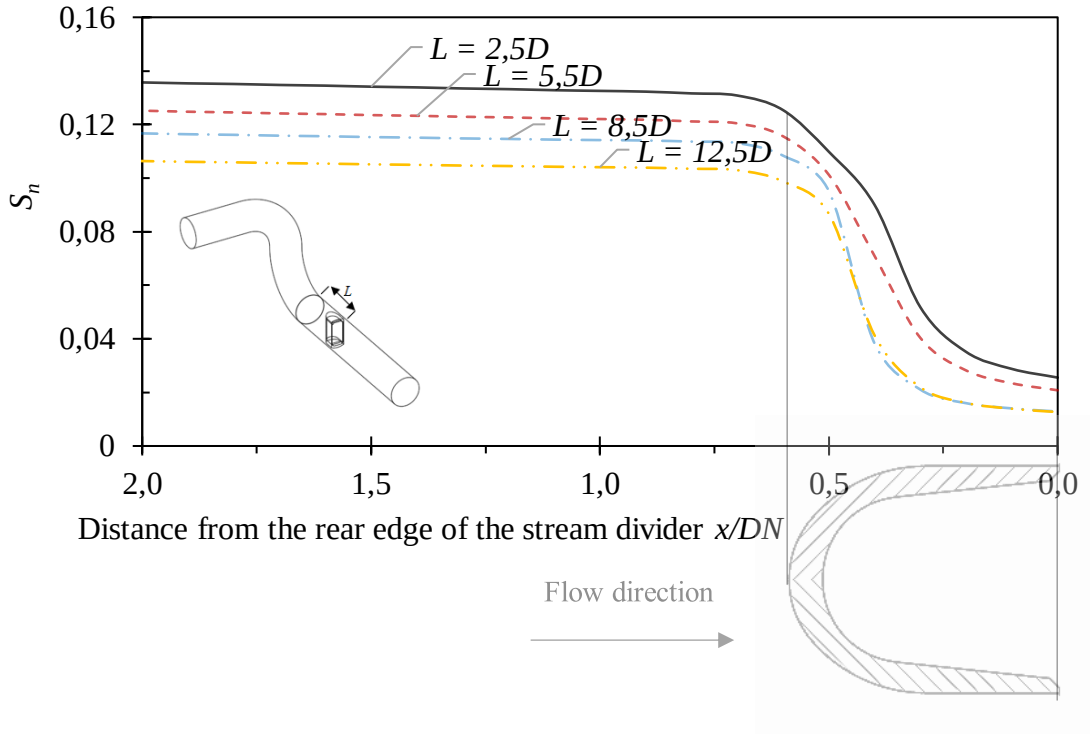

Figure 8.9: Influence of two 90° elbows in perpendicular planes. Swirl number coefficient vs distance from the rear edge of the stream divider for various upstream pipe lengths.

Table 8.2: Influence of a single 90° elbow oriented asymmetrically on the ratio of flow rates between channels of the stream divider.

Inlet pipe length *x*/*D*	The relative difference in mass flow rates
2,5	1,4%
5,5	0,1%
8,5	0,0%
∞	0,0%

Asymmetrically oriented elbows introduce relative differences in mass flow rates between channels of a stream divider (Table 8.2), which fade out for inlet pipe lengths larger than 2,5*D*. This is in agreement with captured installation errors. A correlation between the installation

error and parameters C_f, C_{fm} may be observed on Figure 8.10 and Figure 8.11. In this case both the parameters correspond well to captured errors.

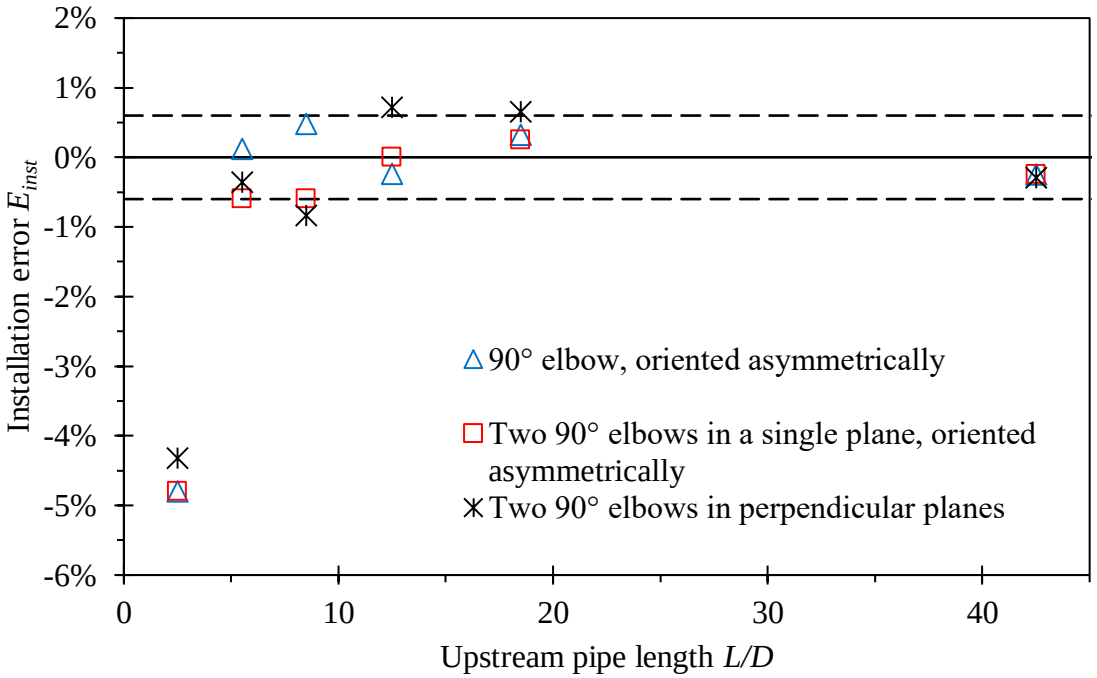

Figure 8.10: Installation errors vs inlet pipe length for asymmetrically oriented disturbances and disturbances introducing swirl. Grey dashed lines denote the sum of flowmeter repeatability and the uncertainty of the measurement stand (*k = 2)*.

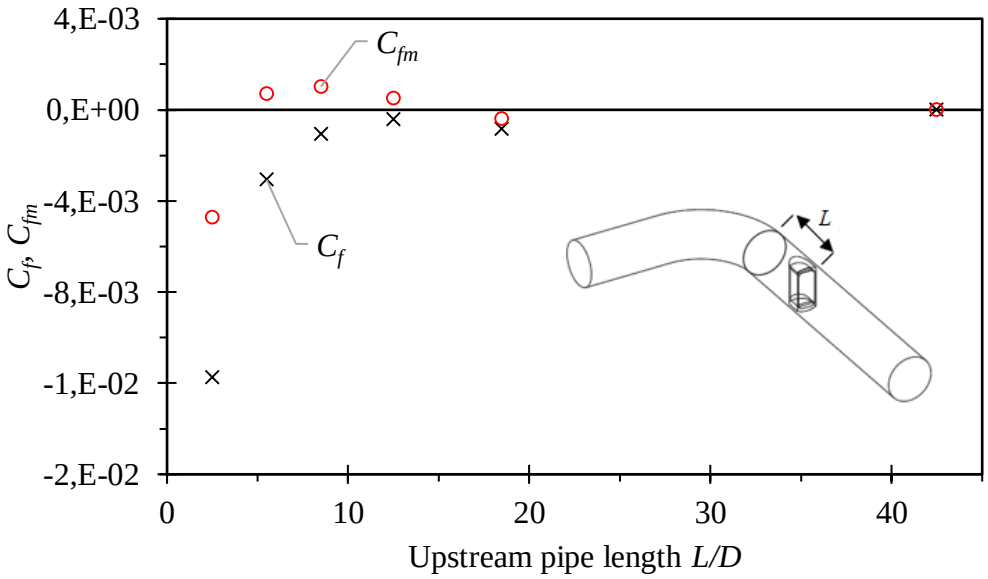

Figure 8.11: Flatness parameter and momentum of flatness parameter measured in the plane at the rear edge of the stream divider vs pipe length after a single 90° elbow oriented asymmetrically.

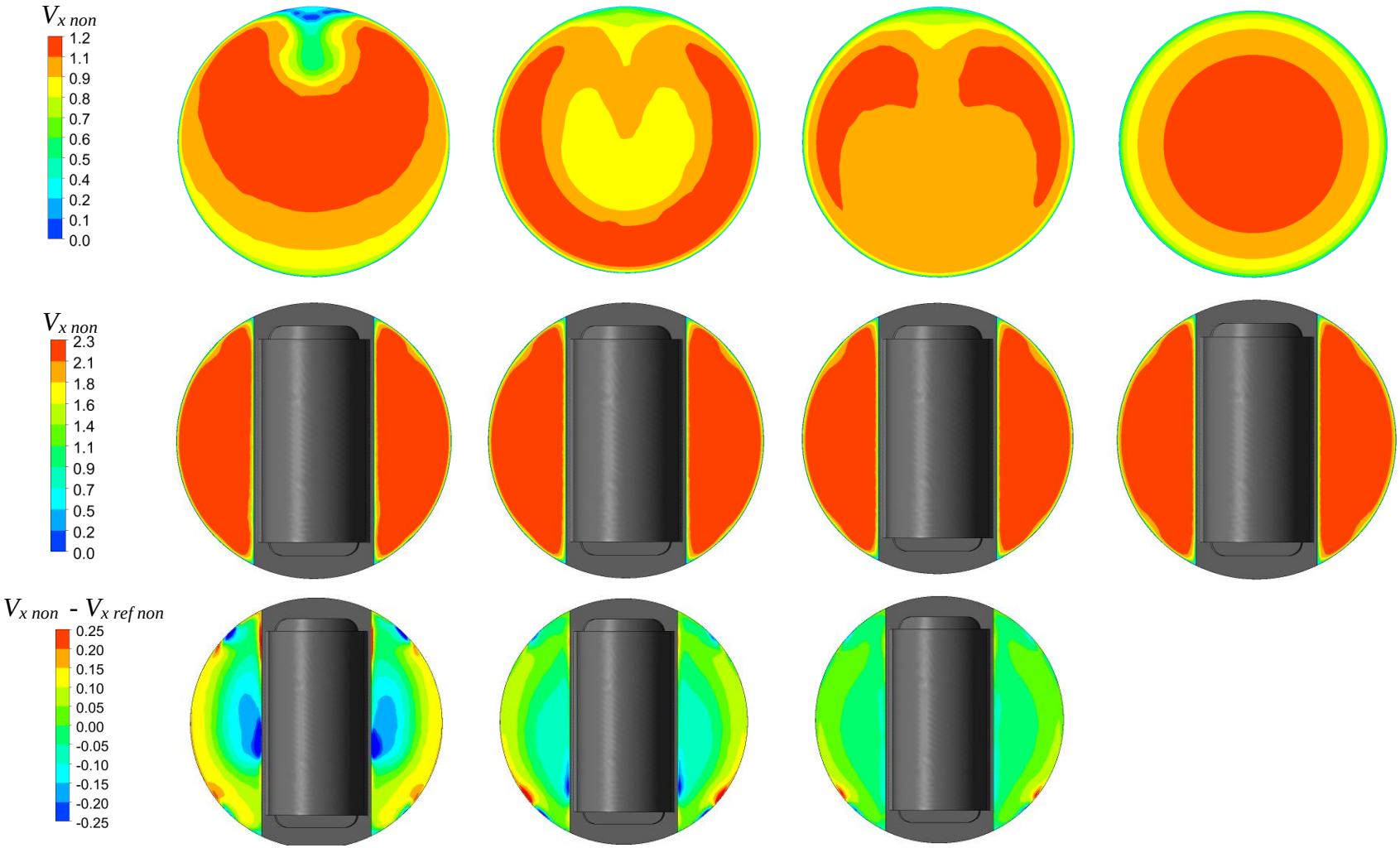

Figure 8.12: Influence of a single 90° elbow oriented symmetrically, axial velocity contours. Top row – plane at distance L downstream the elbow. The second and third rows – plane at the rear edge of the stream divider.

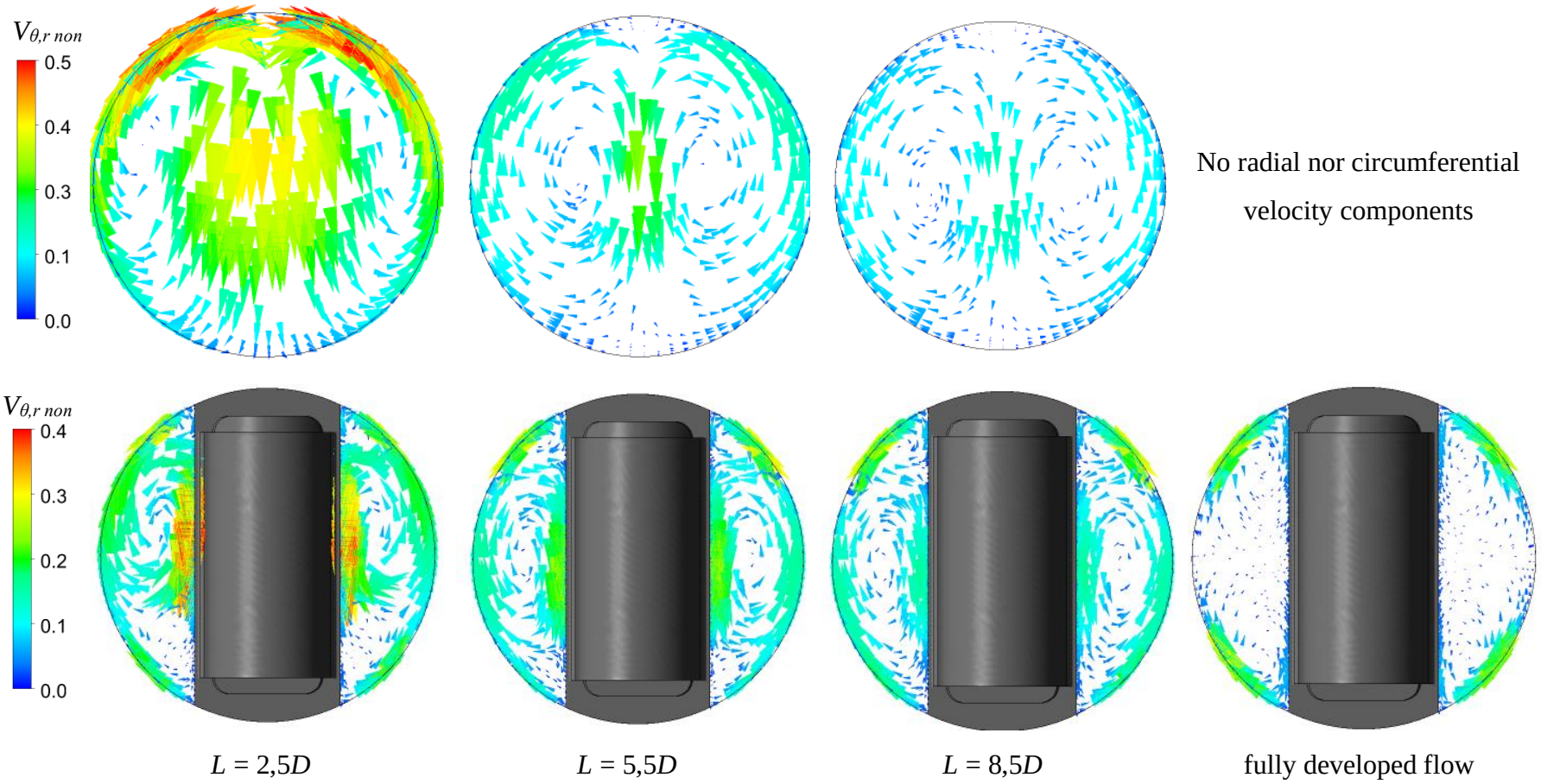

Figure 8.13: Influence of a single 90° elbow oriented symmetrically, radial and circumferential velocity vectors. Top row – plane at distance L downstream the elbow. Bottom row - plane at the rear edge of the stream divider.

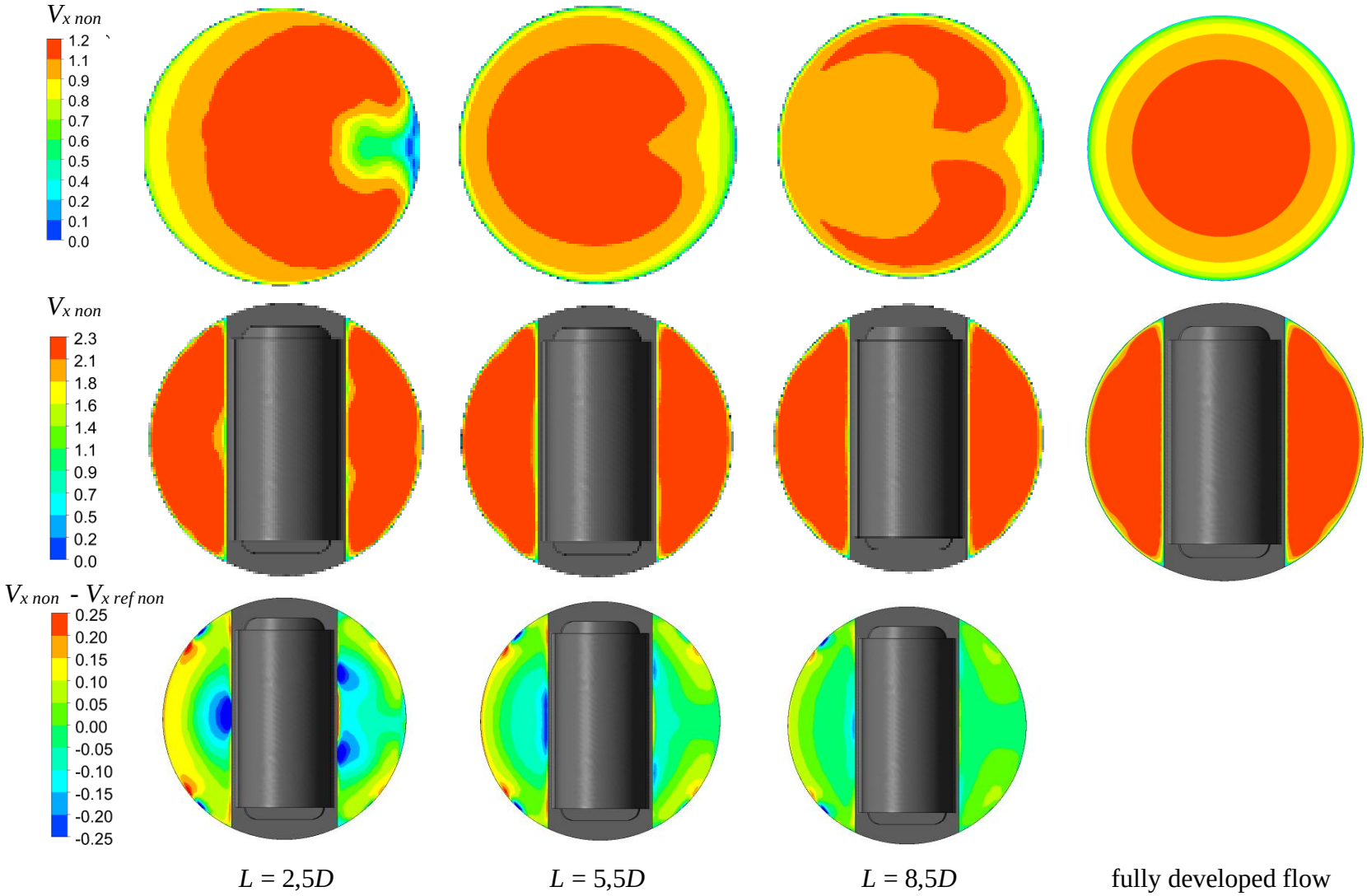

Figure 8.14: Influence of a single 90° elbow oriented asymmetrically, axial velocity contours. Top row – plane at distance L downstream the elbow. The second and third rows - plane at the rear edge of the stream divider.

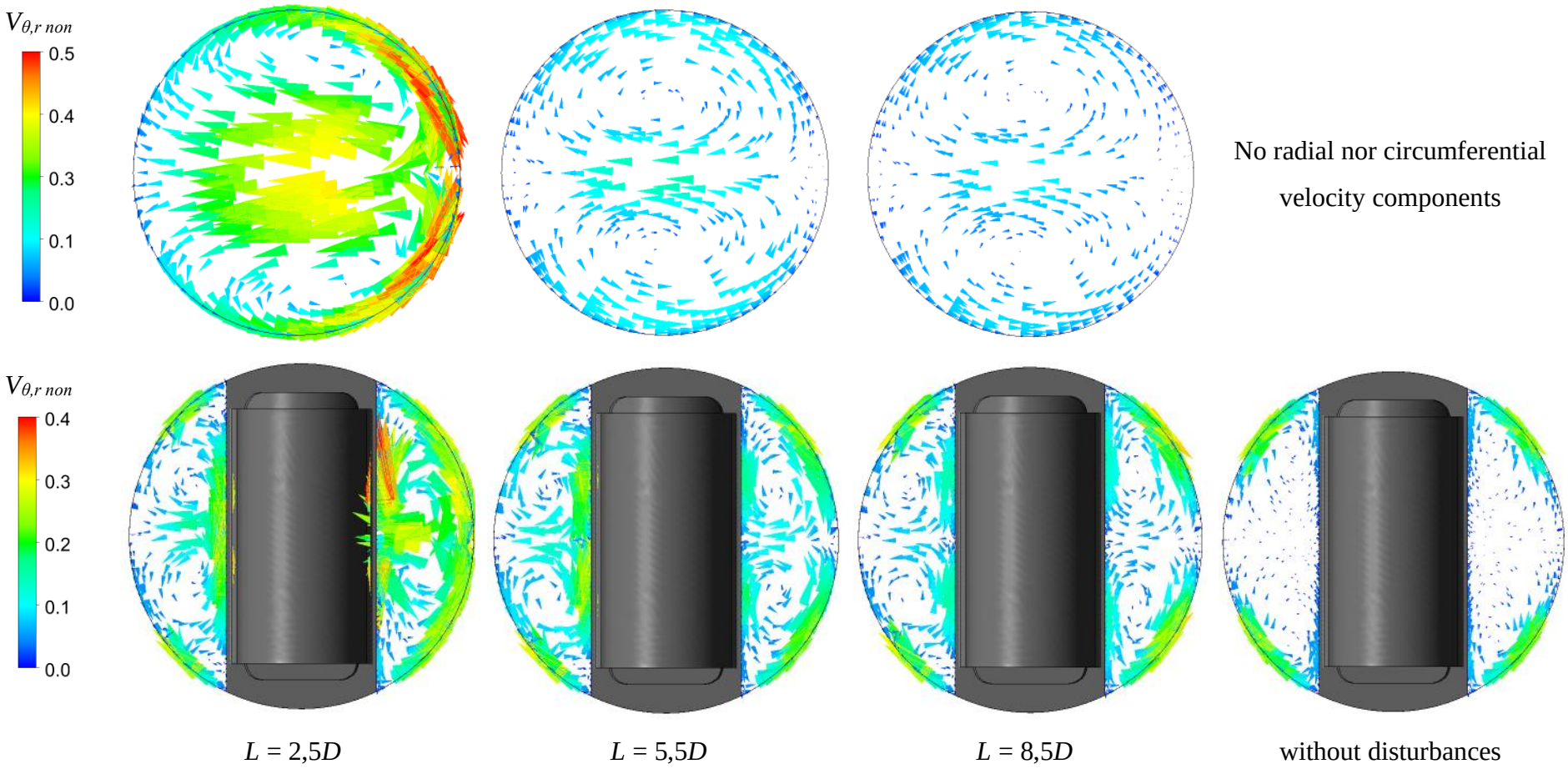

Figure 8.15: Influence of a single 90° elbow oriented asymmetrically, radial and circumferential velocity vectors. Top row – plane at distance L downstream the elbow. Bottom row - plane at the rear edge of the stream divider.

The possibility of reordering a profile by Zanker flow conditioner was also studied. Unfortunately, a certain length between a flow conditioner and a flowmeter is required, usually larger than 10*D*. Meanwhile, installation errors at $L > 10D$ were below the measurement uncertainty, even without a flow conditioner. No significant shift in calibration constant was captured in presence of flow conditioner. As a result, using the current calibration stand there was no prospect in verification if shortening the required inlet straight runs for studied fittings is possible.

8.1.4. Conclusions

The stream divider in its current form is highly effective in reordering the flow profile. The conducted experimental study has verified that previous recommendations on inlet pipe lengths may be relaxed. Installation errors are low and decay quickly in comparison with other flowmeter types (Table 8.3). Such data is of great value, because usually the installation space in industrial conditions is limited.

Table 8.3: Comparison of required straight lengths between flowmeters and fittings.

Disturbance	Orifice flowmeters, $\beta = 0.5$ (International Organization for Standardization, 2007)	Vortex flowmeters (Spitzer, 2001)	Mechanical oscillator flowmeters (current study)
Single 90° bend	22	20	12,5
Two 90° bends in the same plane	18	25	12,5
Two 90° bends in perpendicular planes	44	40	18,5

Steady-state CFD modelling allowed examining the problem in detail. It was shown that such CFD analyses may be performed for other fittings such as tee junctions, non-typical bends, valves or their combinations. Flatness parameter C_f and a swirl number S_n are potentially suitable for evaluation if a velocity profile would introduce additional errors. The conducted

study did not confirm the possibility of installation errors reduction with the use of flow conditioners.

8.2 Performance in the presence of pulsatile flow

8.2.1. Introduction

Pulsatile flow is a specific type of unsteady flow, where a periodical time-varying oscillation is superimposed on a steady component of flow. The most common parameters used to describe pulsatile flows are the dimensionless frequency of pulsation, dimensionless pulsation parameter and pulsation amplitude (Özdinç Çarpinlioğlu and Yaşar Gündoğdu, 2001). Dimensionless frequency of pulsation is calculated as:

$$\omega' = \frac{R^2 \omega}{4\nu} \tag{8.6}$$

where R is pipe radius, ω is the angular frequency of pulsation and υ is kinematic viscosity. Dimensionless pulsation parameter $\sqrt{\omega'}$ influences the flow structure. For $\sqrt{\omega'}$ < 1,32 flow structure is quasi-steady, $\sqrt{\omega'}$ > 28 is inertia dominant region and in-between lies the intermediate region.

Pulsation amplitude A_p is calculated as:

$$A_p = \frac{v'_{rms}}{\overline{v}} \tag{8.7}$$

where v'_{rms} is the root mean square of the variable component of velocity and $\overline{v}$ is the mean velocity. In industrial conditions, pulsation amplitude reaches values from several percent up to more than 100% of mean velocity. Pulsation frequency ranges from fractions of Hz up to hundreds of Hz. During calibration at test stands efforts are made to ensure that no pulsations are present. Meanwhile, in industrial applications pulsations are common, therefore large errors may be introduced.

Overview of pulsatile flow influence on turbine, orifice and vortex flowmeters is given in (Mottram, 1992; Cheesewright, Clark and Bisset, 1999). Possible errors for specific amplitude thresholds have been found for the most of flowmeter types (International Organization for Standardization, 2018). Construction of a test stand presented in this chapter was motivated by a review of the current state of knowledge in this field, as topics that require further

investigation were found. Up till now, mechanical oscillator flowmeters have been studied only in a limited scope of dimensionless pulsation parameter range. (Turkowski, 2003b) studied the influence of pulsatile flow on a DN200 model of a mechanical oscillator flowmeter. Similarly to vortex flowmeters, the lock-in phenomenon has been observed. In the presence of pulsations oscillation frequency no longer corresponds to the actual flow rate, but synchronizes with flow pulsation frequency. Let the pulsation frequency be denoted as f_p and the frequency of the oscillator in steady flow be denoted as f_{os}. Just like in the case of vortex flowmeters (Hebrard, Malard and Strzelecki, 1992), lock-in was captured at $f_p \approx f_{os}$ and was even more distinct at $f_p \approx 2f_{os}$. No measurements were done for higher pulsation frequencies. Dimensionless pulsation parameter held value between 39 and 97, which corresponds to the inertia dominant region.

The work presented in this chapter extended the studied range of parameters by frequencies up to $f_p = 5f_{os}$ and by the intermediate regime of dimensionless pulsation parameter $\sqrt{\omega'}$. The study has been conducted on a DN50 mechanical oscillator flowmeter. The relation between velocity and angular position of the oscillator in lock-in has been studied and possible errors for specific amplitude thresholds were determined.

8.2.2. Test stand

A common pulsator type is a rotating flap (Turkowski, 2003b; Goltsman *et al.*, 2019), which has a disadvantage of introducing additional unwanted disturbance to flow. In presented work, the pulsatile flow is generated by means of a Scotch yoke reciprocating piston mechanism driven by a DC motor (Szudarek, Turkowski and Twaróg, 2019). A similar design has also been described in (Çarpinlioğlu and Gündoğdu, 2001). In the case of the applied design flow rate is a function of piston position in cylinder x_o:

$$q_v = \overline{q_v} + q'_v(t) = \overline{q_v} + \frac{dV(t)}{dt} = \overline{q_v} + Ax_0\omega\cos(\omega t) \tag{8.8}$$

where dV is volume displaced by the piston and A is the piston's cross-sectional area. The amplitude of time-varying oscillation $q'_v(t)$ superimposed on the mean volumetric flow rate $\bar{q}_v$ is a function of pulsation frequency ω. The design allows adjusting the amplitude of piston movement in the range of x_o = (10 – 33) mm to obtain desired pulsation amplitude. Pulsation frequency can be set in range f_p = (1 – 20) Hz by adjusting DC motor supply voltage. The diagram of the test stand is presented in Figure 8.16.

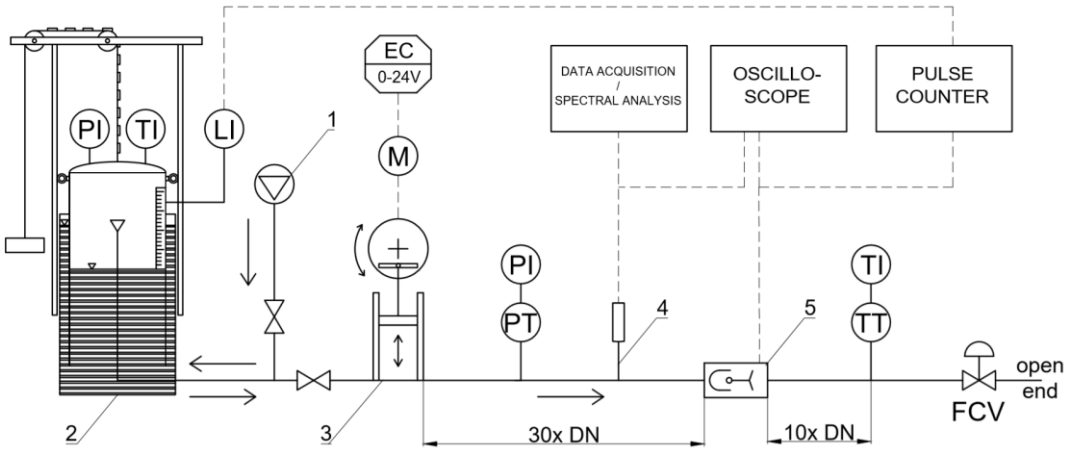

Figure 8.16: Test stand diagram, 1 – fan, 2 – bell prover, 3 – flow pulsator, 4 – constant temperature anemometer, 5 – mechanical oscillator flowmeter, EC – regulated power supply, FCV – flow control valve, LI – level indicator, M – DC motor, PI – pressure indicator, PT – pressure transmitter, TI – temperature indicator, TT – temperature transmitter. Dashed lines denote electrical connections.

The fluid was air at atmospheric pressure. Bell prover calibrated with CFVNs (Wildner *et al.*, 2018, 2019) was used as a reference meter of the displaced volume of air V_b with expanded relative uncertainty $U_{95}(V_b)$ = 0,17%. The pulse output of a mechanical oscillator flowmeter was connected to a counter which is triggered by flags mounted to the bell prover to ensure synchronized measurement. Gauge pressure and temperature were measured both at bell prover (p_b, T_b) and flowmeter (p_u, T_u) locations to calculate the volumetric flow rate in operating conditions that was flowing through the flowmeter q_v:

$$q_v = \frac{V_b}{t} \cdot \frac{(p_a + p_b)T_u}{(p_a + p_u)T_b} \tag{8.9}$$

where t is measurement time and p_a is atmospheric pressure measured with a mercury barometer.

Theoretical considerations on pulsation amplitude and resultant eq. (8.8) is greatly simplified, therefore it could not be used to determine pulsation parameters accurately. Instead, pulsation parameters were obtained by means of spectral analysis of a signal registered by a constant temperature anemometer (CTA). In the study, the probe was positioned on the pipeline axis. The device used was a single-probe Dantec Dynamics 55P16 connected to MiniCTA 54T30 amplifier package. The connection between amplifier and PC was realized by National

Instruments Hi-Speed USB CARRIER USB-9162. The sampling frequency was equal to 1 kHz. The number of samples was adjusted for each pulsation frequency to acquire ca. 200 cycles per measurement. Signals from the flowmeter and CTA were also directed to a digital oscilloscope Siglent SDS 1074 CFL to capture their interrelation.

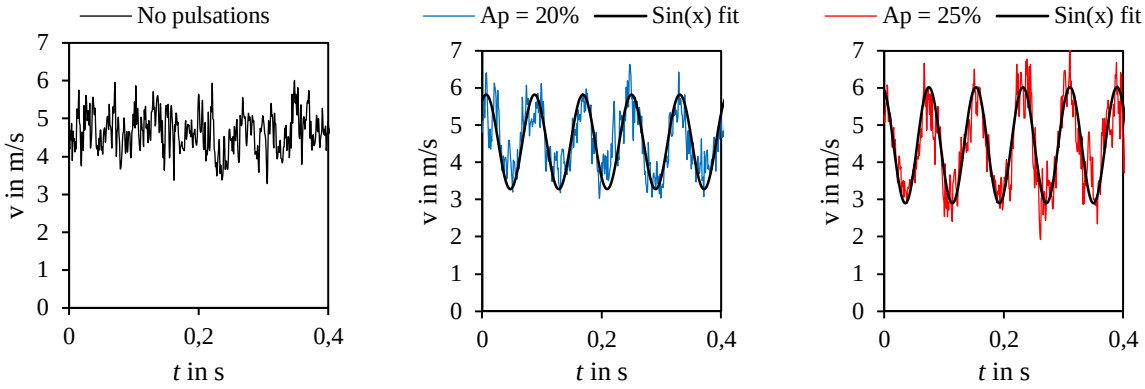

(a)

(b)

(c)

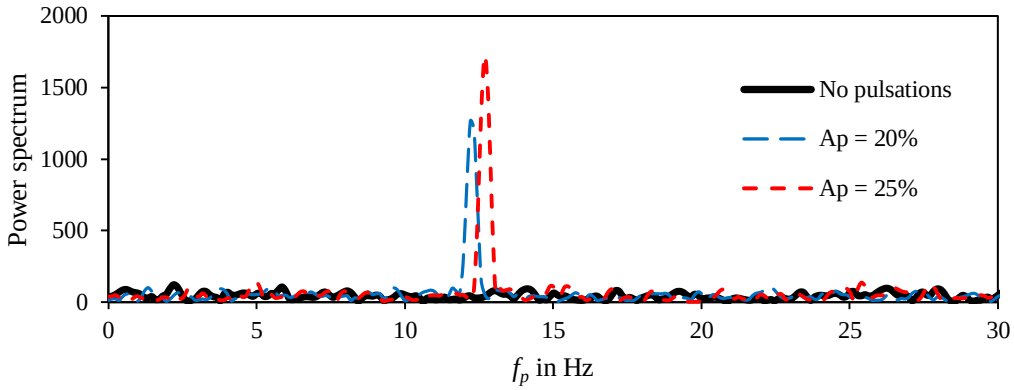

(d)

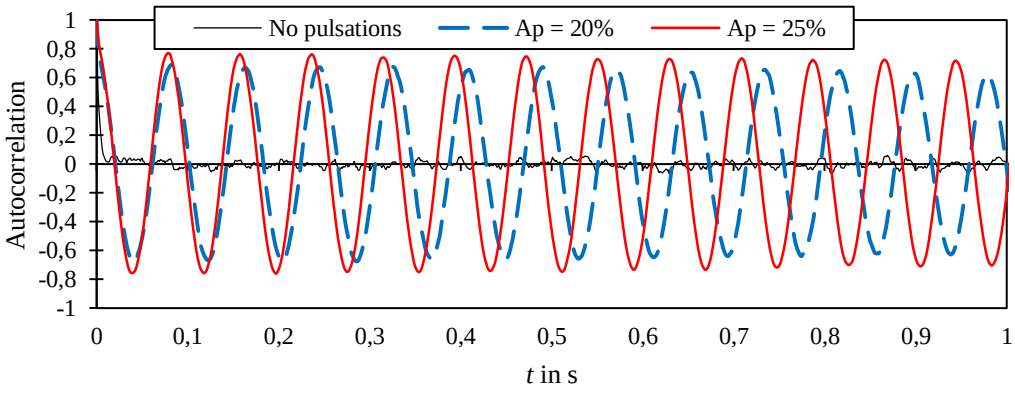

(e)

Figure 8.17: Velocity registered by CTA. (a) for flow without pulsations; (b) with pulsations, amplitude 20%; (c) with pulsations, amplitude 25%; (d) power spectrum plot; (e) autocorrelation plot.

The spectral analysis of exemplary data from CTA is shown in Figure 8.17. The amplitude of turbulence shown in Figure 8.17a is 10%. As expected, pulsations are of sinusoidal character (Figure 8.17b-c). Steep single peaks are visible on the power spectrum plot (Figure 8.17d). The difference between pulsatile and statistically steady flows can be observed in the autocorrelation plot (Figure 8.17e). In the case of pulsatile flow, the autocorrelation plot is periodic, whereas for turbulent flow it decays to zero.

8.2.3. Results and discussion

The constructed test stand allowed extending the studied range of parameters by frequencies up to $f_p = 5f_{os}$ and by the intermediate regime of dimensionless pulsation parameter $\sqrt{\omega'}$. A list of parameters covered in the study is summarized in Table 8.4.

Table 8.4: Parameter range covered in the study.

Parameter	**Range**
Volumetric flow rate q_v	(22 – 45) m^3/h
Time-averaged Reynolds number Re_{ta}	11 000 – 23 000
Pulsation frequency f_p	(2 – 17) Hz
Pulsation amplitude A_p	(13 – 30)%
Dimensionless pulsation parameter $\sqrt{\omega'}$	11,4 – 34,3

At first, the error curve of the flowmeter was captured for ideal flow conditions, without pulsations. In the ideal flow conditions, the standard deviation of measured oscillator frequency did not exceed 0,5% at any flow rate. Then, flow pulsations were introduced. For a constant volumetric flow rate, shifts in flowmeter signal frequency in the function of pulsation frequency were observed. In the preliminary study, the pulsation amplitude has not been held constant and ranged between (13 – 30)%. The influence of pulsatile flow on flowmeter readings for various flow rates is shown in Figure 8.18. Ideally, there would be no correlation between pulsation frequency and oscillator frequency and all the points would fall on horizontal lines. No significant correlation is observed for $f_p < 0{,}5f_{os}$. Lock-in is more distinct for pulsation frequencies approaching the first harmonic of oscillator frequency in steady-state than for its fundamental frequency, which is in compliance with previous works. For frequencies above $2f_{os}$, metering errors up to 15% are found. However, oscillator frequency does not synchronize with pulsation frequency for subsequent harmonics.

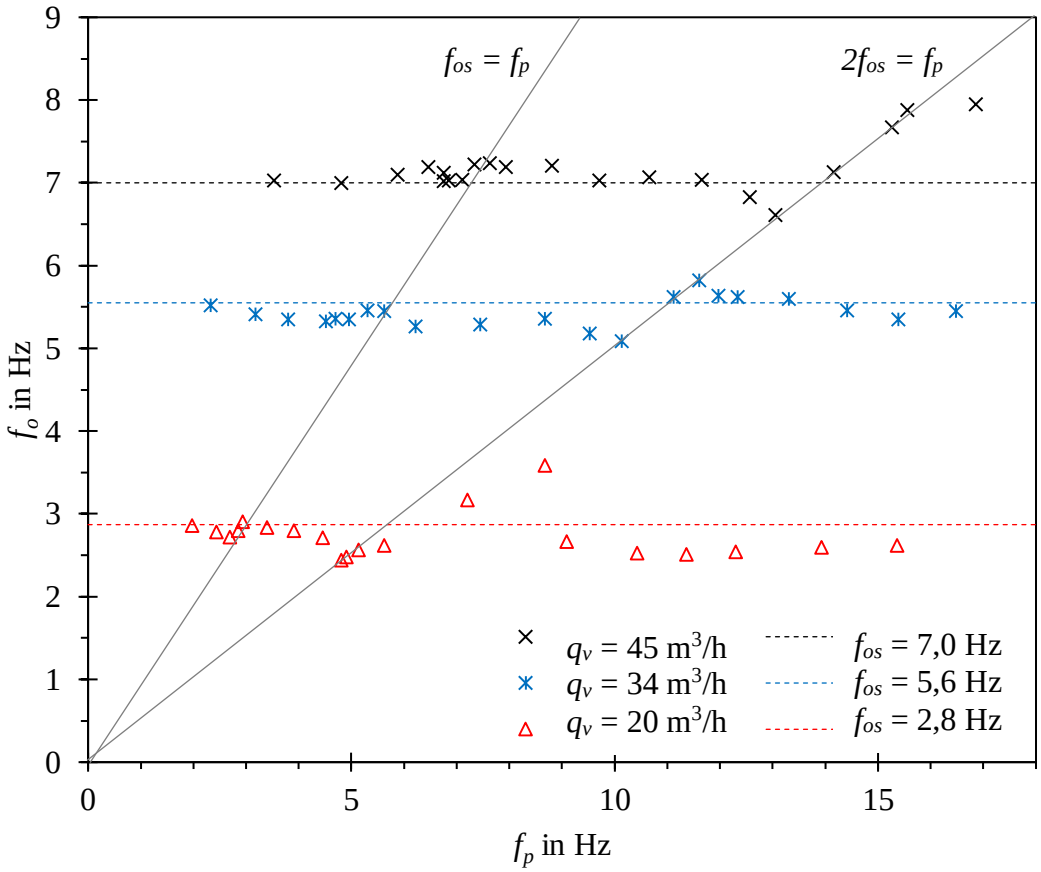

Figure 8.18: Influence of pulsatile flow on oscillator frequency for various flow rates. Solid lines denote oscillator frequency in steady flow conditions.

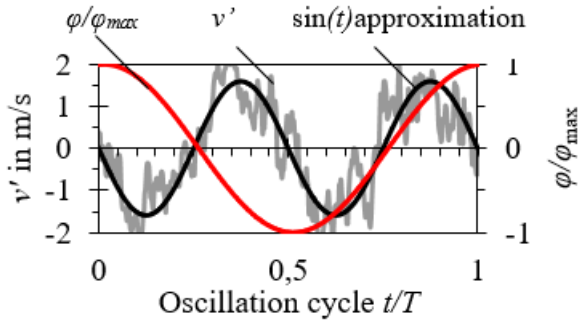

Figure 8.19: Relation between velocity and angular position of the oscillator in a lock-in at $f_p = 2f_{os}$.

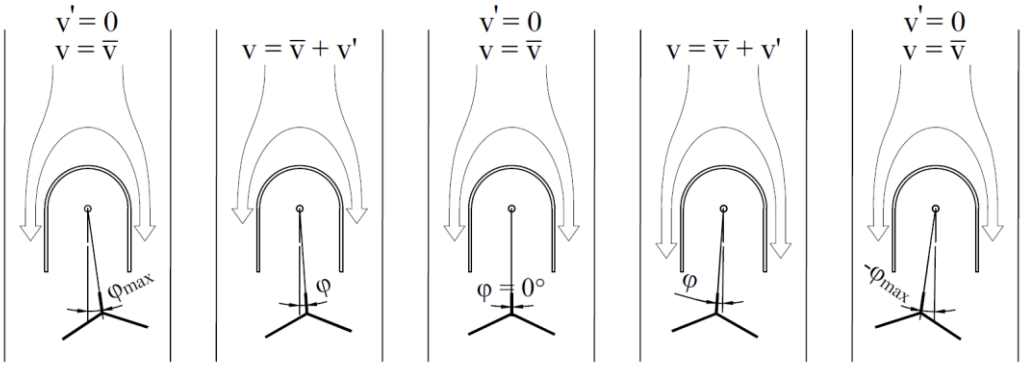

Figure 8.20: Illustration of relation between velocity and angular position of the oscillator in a lock-in at $f_p = 2f_{os}$.

The relation between velocity and angular position of the oscillator in lock-in is shown in Figure 8.19 and Figure 8.20. The observation is that in lock-in state the oscillator synchronizes with the pulsation in such a manner that at neutral and extreme positions of the oscillator the variable component of velocity is equal to zero.

The following test studied the influence of pulsation amplitude on measurement errors. The volumetric flow rate was held at a constant value of 33,7 m^3/h, which allowed avoiding the influence of Reynolds number on the lock-in range. The study was performed for three amplitudes: 15%, 20% and 25%, results are shown in Figure 8.21. Relative error E was calculated as:

$$E = \frac{f_O - f_{OS}}{f_{OS}} \tag{8.10}$$

where f_o is oscillator frequency in the presence of pulsatile flow.

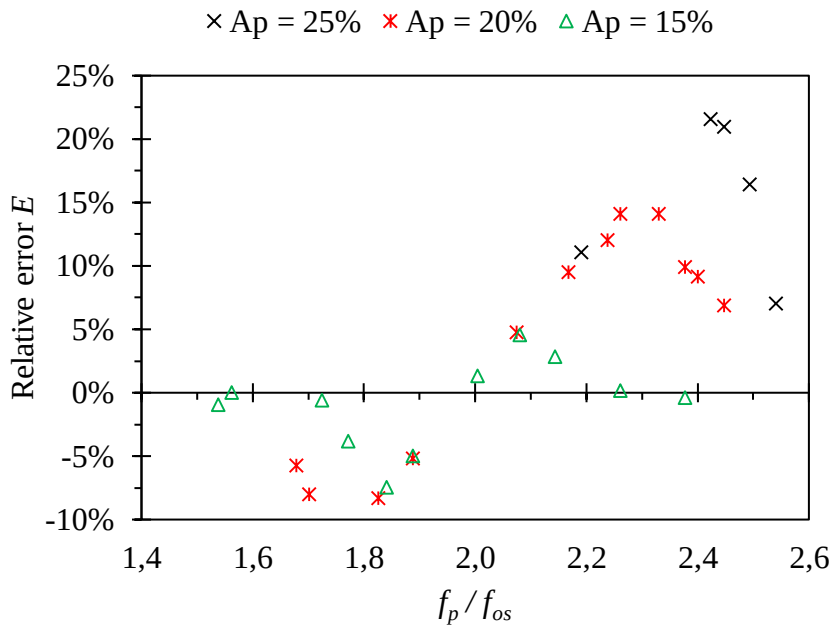

Figure 8.21: Influence of pulsation amplitude on the relative error.

Higher pulsation amplitudes not only cause higher maximal relative errors, but also larger lock-in frequency range. In the range where lock-in occurs for all the studied amplitudes (1,9 < fp/fos < 2,1) error values do not depend on pulsation amplitude.

8.2.4. Conclusions

Mechanical oscillator flowmeters, similarly to vortex flowmeters or any oscillatory flowmeters are prone to frequency lock-in. It occurs for $f_p \approx f_{os}$ and to a higher extent for $f_p \approx 2f_{os}$. Possible errors for specific amplitude thresholds have been determined. The application of a mechanical oscillator flowmeter is not recommended if the pulsation frequency in the installation is in the lock-in range.

For frequency ratios $f_p/f_{os} <$ 0,5 no pulsation influence has been observed. To take advantage of this fact one can move outside lock-in range by increasing oscillator working frequency. This can be achieved by lowering its moment of inertia or by installing a flowmeter of smaller diameter. For frequency ratios $f_p > 3f_o$ constant offset errors were captured, but no frequency lock-in.

Table 8.5: Errors due to pulsatile flow for various flowmeters types.

Flowmeter type	Orifice			Turbine		
Pulsation amplitude	0,1	0,2	0,5	0,1	0,25	0,5
Absolute value of relative error (%)	0,7	2,2	8	0,7	4,5	15

In the future, it would be worthwhile to examine the influence of pulsatile flow outside the lock-in range. It would allow comparing the performance of mechanical oscillator flowmeters with other flowmeter types, e.g. against data from (International Organization for Standardization, 2018) presented in Table 8.5. Such a study requires constructing a pulsator capable of generating pulsations of higher frequencies, e.g. based on a membrane (Svete *et al.*, 2012).

8.3 Influence of pipe wall roughness

8.3.1. Introduction

In industrial conditions, the roughness of the inside surface of the pipe wall is almost an uncontrollable parameter. It influences the velocity profile, which is flatter in smooth pipes than in rough pipes. Its effect may be secondary or even insignificant in many applications, such as turbine flowmeters (Van der Kam and Dam, 1993). In contrast, wall roughness has been identified as having a large influence on orifice flowmeters (International Organization for Standardization, 2003b) and vortex flowmeters (Mottram, 1991). In the case of vortex flowmeters roughness causes an increase of local velocity at the bluff body and an increase in vorticity.

In the field of flow metrology, roughness is commonly described with *Ra* parameter (International Organization for Standardization, 2003b; Adamczak, 2008). Older studies tended to use roughness height ε which can be approximated by πRa (Turkowski, 2018). Neither of the parameters is flawless, as surfaces with the same *Ra* value but different roughness structures may influence the velocity profile differently. A common practice is to state the maximum permitted roughness for a given flowmeter type. Recommendations for orifice flowmeters are presented in Table 8.6.

Table 8.6: Maximum permitted roughness in the function of Reynolds number for orifice flowmeters with $\beta \geq 0{,}65$ (International Organization for Standardization, 2003b).

Reynolds number	10^4 *Ra/D*
10^4	4,2
10^6	0,8
10^8	0,3

Currently, no study has been conducted on the influence of roughness on mechanical oscillator flowmeters, which was a motivation for the work presented in this chapter.

8.3.2. Methods

The experiments were conducted at the low-pressure air calibration stand described in the Chapter 4.3. First, a baseline error curve has been determined using a smooth pipe. To study the effect of surface roughness, a 24-grit sandpaper was fitted to the inner wall of the pipe upstream of the flowmeter (Figure 8.22a). Such a methodology has been successfully applied

in other studies of this kind (Tomasik, Turkowski and Zagozdzon, 2008). The sandpaper, however, introduces a slight step-change in diameter just before the flowmeter (1,8 mm ≈ 0,04*D*). Therefore it was considered worthwhile to study the effect of a step-change in diameter first (Figure 8.22b). Measurement of characteristics for smooth inlet pipes of diameters equal to 46 mm and 54 mm (0,08*D*) was done.

As shown in Figure 8.23, *Ra* of the sandpaper was estimated as 68 μm ($14 \cdot 10^4$ *Ra/D*) by extrapolation of the measurement data given in (Tomasik and Turkowski, 2007).

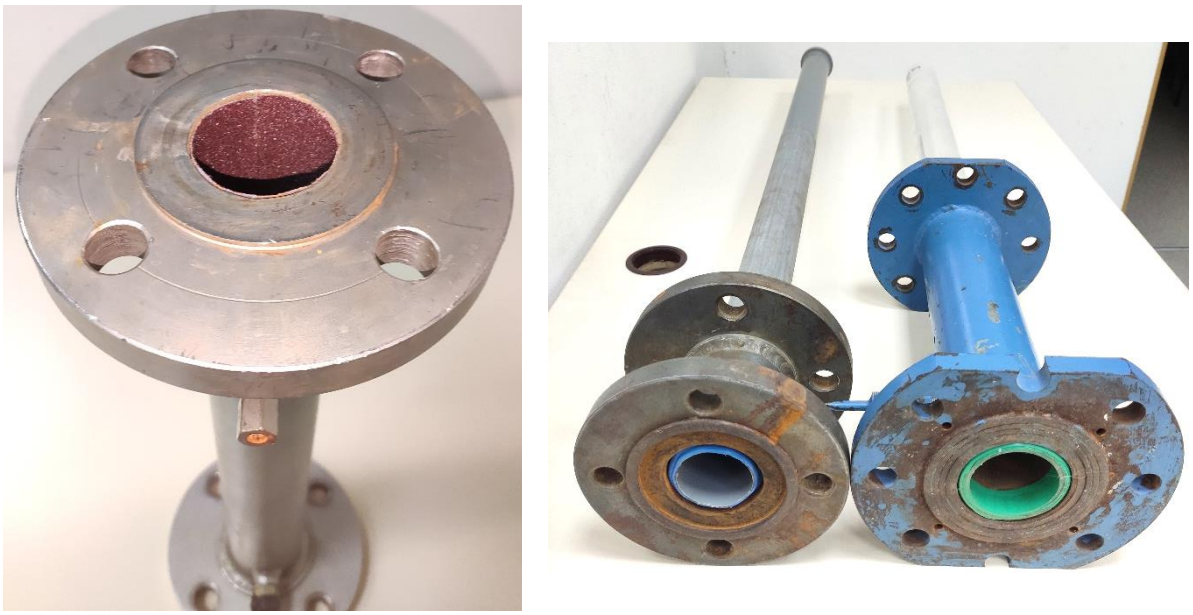

(a) (b)

Figure 8.22: (a) Pipe lined with a sandpaper, D = 48,2 mm; (b) pipe fitted with a D = 46 mm PVC tube (left) and a D = 54 mm plexiglass tube (right), both of length 20D.

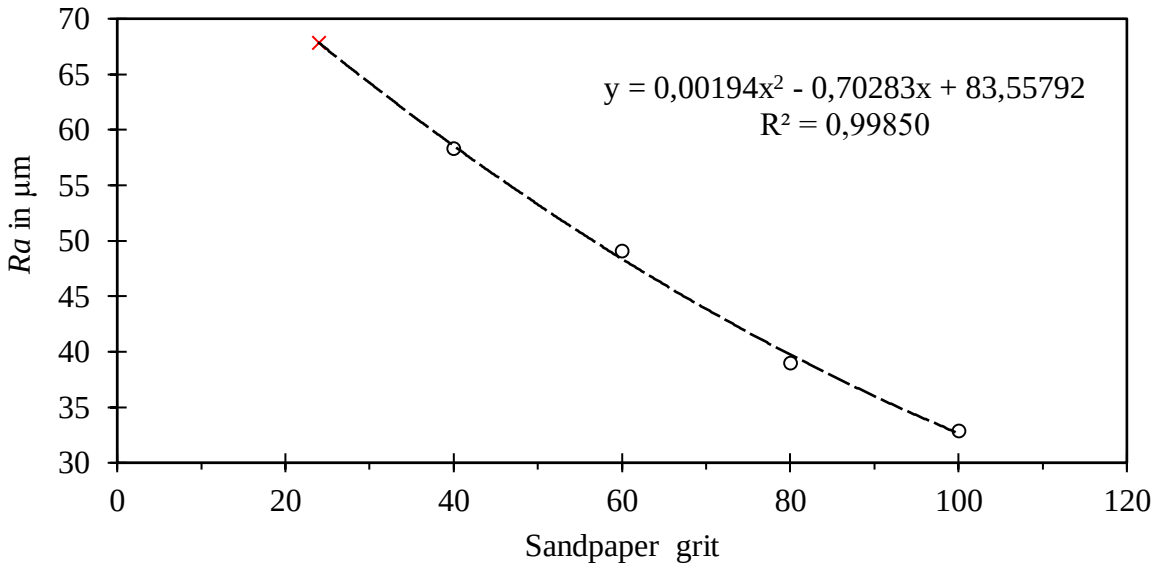

Figure 8.23: *Ra* vs sandpaper grit, extrapolated value is marked with *X*.

8.3.3. Results and discussion

Eight-percent step-change in diameter before the flowmeter only slightly influences the measurement characteristics (Figure 8.24). In the latter part of the study, it was assumed that the reduction of diameter caused by the thickness of sandpaper (1,8 mm or 0,036*D*) does not affect the measurement.

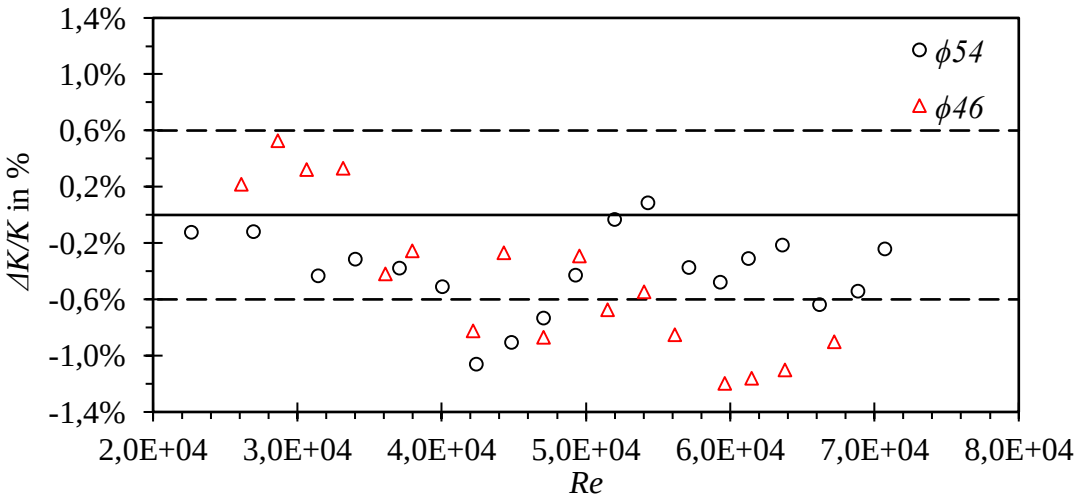

Figure 8.24: Shift in the error curve caused by step-change in diameter vs Reynolds number, dashed lines denote the uncertainty of the calibration stand increased by the repeatability of the flowmeter.

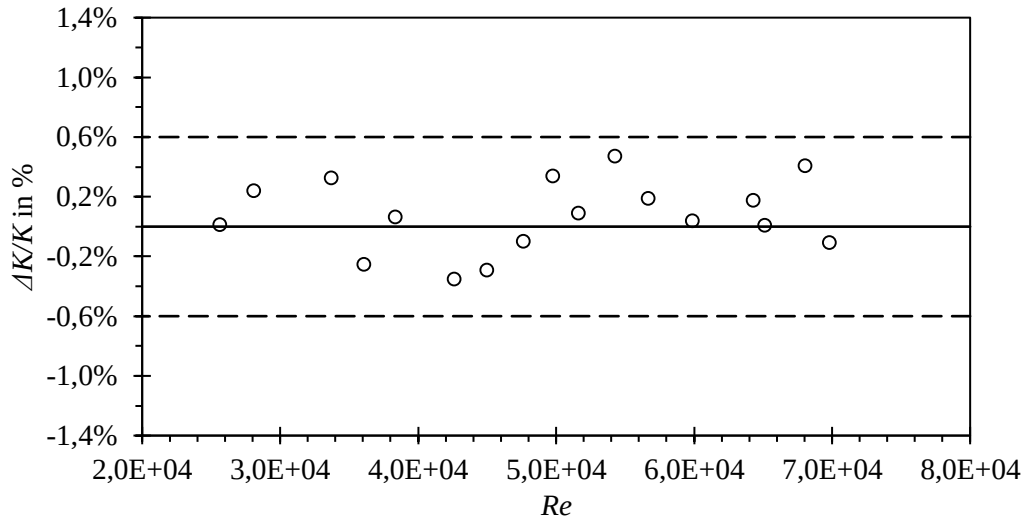

Figure 8.25: Shift in the error curve caused by increased surface roughness of $14 \cdot 10^4$ *Ra/D* vs Reynolds number, dashed lines denote the uncertainty of the calibration stand increased by the repeatability of the flowmeter.

Even for such a high value of roughness as $14 \cdot 10^4$ *Ra/D*, the influence of roughness portrayed in Figure 8.25 is below the uncertainty of the measurement. No visible trend was captured and it was interpreted as a systematic error. For that reason, the study was not continued with sandpapers of smaller grits.

8.3.4. Conclusions

The study uncovered that 0,08*D* step-change in diameter results in a small, but noticeable shift in the error curve.

The influence of inlet pipe roughness is insignificant even for $14 \cdot 10^4$ *Ra/D* in the range of *Re* = (25 000 – 70 000). Most probably the stream divider reorders the flow profile to such an extent, that it removes subtle effects of roughness.

Chapter 9

Experiments in cryogenic conditions

9.1 Influence of density and temperature on calibration constant

9.1.1. Introduction

In the following chapter the results of experiments conducted in cryogenic conditions are presented. They were an opportunity to verify existing equations that describe the influence of density and temperature on calibration constant. The current state of knowledge will be summarized first. The following considerations originate from (Heckle, 1973; Turkowski, 2003b).

Density influences not only the torque originating from the action of the fluid impinging on the oscillator, but also affects the damping action of the fluid and the total moment of inertia of the oscillator. A certain mass of fluid moves with the oscillator because of adhesion and viscous friction. The total moment of inertia is, therefore, a sum of moments of inertia of the oscillator and the added mass of fluid.

$$I = I_o + I_f \tag{9.1}$$

In the case of the oscillator, the moment of inertia I_o can be easily determined from its dimensions and material density. The moment of inertia of the adhering fluid is harder to estimate. Flow elements oscillate with variable amplitude, depending on the distance from the oscillator and the oscillator's shape. Instead, an equivalent moment of inertia of a rigid body that would produce the same effect I_f is considered.

Let us consider the simplified formula for the oscillation frequency (Turkowski, 2003b):

$$f = \frac{l_0 q_m}{2\pi A}\sqrt{\frac{h\psi(\alpha,\gamma)}{2\rho I}} \tag{9.2}$$

where f is the frequency, q_m is mass flow rate, ρ is the density of the measured fluid, I is the total moment of inertia, ψ is a trigonometric function depending on the geometry of the oscillator, and A, α, γ are parameters describing geometry.

Let coefficient *r* denote the ratio of moment of inertia of the adhering fluid for a unit density to the moment of inertia of an oscillator. The unit of *r* is m^3/kg.

$$r = \frac{I_{f(\rho=1)}}{I_o} \tag{9.3}$$

Then the formula (9.2) may be written as:

$$f = \frac{l_0 q_m}{2\pi A}\sqrt{\frac{h\psi(\alpha,\gamma)}{2I_o(1+r\rho)}} \tag{9.4}$$

and the calibration constant for the fluid of density ρ_1 takes the form:

$$K_{m1} = j\sqrt{\frac{1}{\rho_1(1+r\rho_1)}} \tag{9.5}$$

where constant *j* groups dimensions of the flowmeter. The approximate character of formulas (9.4) and (9.5) excludes the possibility of determining the calibration constant analytically. Instead, calibration constants and the value of *r* coefficient are determined experimentally, by performing calibrations with two fluids of different densities:

$$K_{m1} = j\sqrt{\frac{1}{\rho_1(1+r\rho_1)}} \qquad K_{m2} = j\sqrt{\frac{1}{\rho_2(1+r\rho_2)}} \tag{9.6}$$

solving (9.6) for *r* one obtains:

$$r = \frac{K_{m1}^2\rho_1 - K_{m2}^2\rho_2}{K_{m2}^2\rho_2^2 - K_{m1}^2\rho_1^2} \tag{9.7}$$

In such a case it is not required to know the exact dimensions of a flowmeter to determine the value of *r* coefficient. Its uncertainty depends only on the combined uncertainties of densities and calibration constants.

The same methodology has been applied for the oscillators in the shape of hollow prisms (Heckle, 1973), as well in the geometry that is of interest in this thesis (Turkowski, 2004). Turkowski determined values of *r* for DN50, DN65 and DN100 basing on calibration data for water ($\rho \approx 998$ kg/m^3) and liquid sulphur ($\rho \approx 1618$ kg/m^3). The dimensional analysis allowed extrapolating the data for all the other manufactured nominal diameters.

Moving to the influence of temperature on the calibration constant - it is a common practice among manufacturers of Coriolis flowmeters to determine calibration constant for water in room temperature and 70°C and then extrapolate the data even down to cryogenic temperatures. The question is whether a similar procedure is applicable in the case of mechanical oscillator flowmeters. (Turkowski, 2004) developed an empirical formula for the influence of temperature based on the eq. (9.4) and the assumption that the pipe and each element of the flowmeter undergoes linear thermal expansion. The resultant temperature correction coefficient is:

$$K_{m,T} = K_m \cdot k_T \qquad k_T = [1 + \lambda_T (T_x - T_r)]^{-3/2} \tag{9.8}$$

where T_r is the reference temperature, T_x is the actual temperature, λ_T is the linear thermal expansion coefficient, K_m is mass calibration constant and $K_{m,T}$ is the calibration constant after correction for temperature. The above formula was verified by Turkowski with the use of room temperature and 120°C water, which corresponded to correction in the range of 0,27%. Unfortunately, the resultant shift in the error curve was of the same order of magnitude as measurement uncertainty. Therefore the equations are not perceived as validated but on the other hand the collected data did not give basis to reject the formula.

The work presented in this chapter aims to extend the study on the influence of density and temperature on the calibration constant. The shortcoming of the study conducted by Turkowski was that only two fluids were used to determine the value of *r*, therefore results were not validated. The experimental study covers water, liquid nitrogen and LNG, which have substantially different densities.

9.1.2. Materials and methods

Although the target application is LNG, the preliminary study in cryogenic conditions was conducted on liquid nitrogen. It is not flammable and therefore it does not require expensive ATEX-certified equipment. This is a common practice in the case of new designs dedicated to LNG measurement (Hogendoorn, Boer and Danen, 2007). The goal of the study was to verify

if the mechanical oscillator flowmeter maintains its metrological parameters, i.e. linearity of the characteristics and repeatability in cryogenic conditions. Additionally, electronics that are a part of the flowmeter had to be protected against low temperatures. The tests have shown if measures that were taken were sufficient. The boiling point temperature is lower for liquid nitrogen than LNG, which poses even a greater challenge for electronic parts. After successful tests on liquid nitrogen, a calibration using LNG was done by the author.

The experiments using liquid nitrogen took place on the premises of Vein company in Pszczyna. The study was conducted for the mass flow rate range that can be expected during the process of LNG unloading, i.e. (6 – 16) t/h. Both the flowmeter under test and the reference meter "SMOK" were installed in a closed-loop with a tank truck (Figure 9.1). A cryogenic pump forced the flow of liquid nitrogen. The reference meter was a Coriolis flowmeter that was calibrated in cryogenic conditions, together with its temperature and pressure transmitters (Ciemnołońska and Rosłonek, 2018).

Figure 9.1: Mobile calibration stand "SMOK" (WysokieNapiecie.pl, 2018).

The mass measured by Coriolis flowmeter was compared directly with the number of pulses generated by the oscillator to determine calibration constant in pulses/kg. Synchronization

between both counters was performed manually by the operator. Similarly to the low-pressure air calibration stand, the uncertainty of synchronization was reduced by extending measurement time.

In the case of LNG, all of the equipment in the hazard zone had to be ATEX-certified, as LNG is extremely flammable. Hazard zone 2 concerned the area of ca. (15 – 25) m around the LNG line, which meant that both the preamplifier of the coil signal and the temperature sensor and transmitter had to be certified. The rest of the equipment were installed in the safe zone 30 m away from the site, past circuit separators.

Calibration with the use of LNG took place at a local regasification plant during the routine process of unloading a tank truck. Once again, the reference was PGNiG "SMOK" system, based on Coriolis flowmeter. The tank truck was equipped with a vaporizer, which was used to heat part of the load and increase the pressure of LNG in the truck. The pressure difference between the tank truck and the storage tank forced the flow, no cryogenic pump was present.

Two operators, one standing in the hazard zone, one in the safe zone, synchronized counters of both flowmeters. The mass measured by Coriolis flowmeter was used in combination with the number of pulses from the mechanical oscillator flowmeter to determine the error curve. Due to the nature of the process, once it was started there was no possibility to stop the flow, dismantle the pipe and swap the oscillators. For that reason, only one oscillator was selected for calibration. During the process of unloading the truck, it was possible to choke the flow to capture the error curve in range (3,3 – 8) t/h.

A comparison of selected parameters of fluids used in the study is presented in Table 9.1, basing on data from (Grevendonk, Herreman and De Bock, 1970). A significant difference in density between fluids can be noted. The viscosity of cryogenic fluids is one order of magnitude lower than the viscosity of water.

Table 9.1: Parameters of fluids used in the study, densities correspond to the pressure of 6 bar abs.

Parameter	**Water**	**Liquid nitrogen**	**Liquefied natural gas**
Density	998 kg/m^3	718 kg/m^3	422 kg/m^3
Viscosity	1 cP	0,1 cP	0,1 cP
Temperature	20°C	-178°C	-150°C

The influence of the thermal expansion of the pipe and flowmeter components was estimated using the material data presented in (Skibina *et al.*, 1985). As the linear thermal expansion coefficient for austenitic steel varies substantially in the function of temperature, the temperature correction coefficient was calculated from the formula:

$$k_T = [1 + \int_{T_r}^{T_x} \lambda_T(T) dT)]^{-3/2} \tag{9.9}$$

9.1.3. Results and discussion

For temperatures T_x = 97,15 K and T_r = 273,15 K the temperature correction coefficient k_T equals 1,004. This translates to 0,4% shift in the error curve, which is a minor value. In comparison, the influence of the density difference between water and liquid nitrogen causes a 30% shift in the error curve. Nevertheless, the correction for temperature was included even though it could not have been validated.

Table 9.2: Obtained values of *r* coefficients.

Fluids	K_{m1} **in 1/kg**	K_{m2} **in 1/kg**	k_T	***r* in dm³/kg**	$U_{95}(r)$ **in dm³/kg**
water – liquid nitrogen	10,081	13,146	1,004	1,71	0,22
water – LNG	10,081	16,868	1,003	0,35	0,22

The values of *r* coefficient obtained in the experimental study are collected in Table 9.2. The differences between coefficients obtained for subsequent pairs of fluids are larger than the measurement uncertainty. It is possible that the value of *r* is not constant in function of density and an additional study in this topic is necessary.

As for now, it is recommended to calibrate the flowmeter with a fluid of the same density as in the target application. If the average *r* equal to 0,60 dm³/kg was assumed to determine calibration constants for cryogenic fluids only basing on calibration using water, an error of 4% would be introduced.

9.2 Performance in cryogenic conditions

The study has shown that the flowmeter operates properly in cryogenic conditions. The output signal from the coil was stable. Figure 9.2 depicts the flowmeter during the measurement of

liquid nitrogen. The effectiveness of the radiators that protect the preamplifier of the coil signal (blue box) is visible, as frost does not extend above the first radiator.

Figure 9.2: Mechanical oscillator flowmeter during the measurement of liquid nitrogen.

Characteristics of two oscillators were captured and in both cases nonlinearities did not exceed 0,5%, which is demonstrated in Figure 9.3. Repeatability during the measurement of liquid nitrogen was comparable to the case of the measurement of water. For each mass flow rate, the spread of results was smaller than 0,4%. The legal requirements which specify MPE of 1,5% were therefore fulfilled.

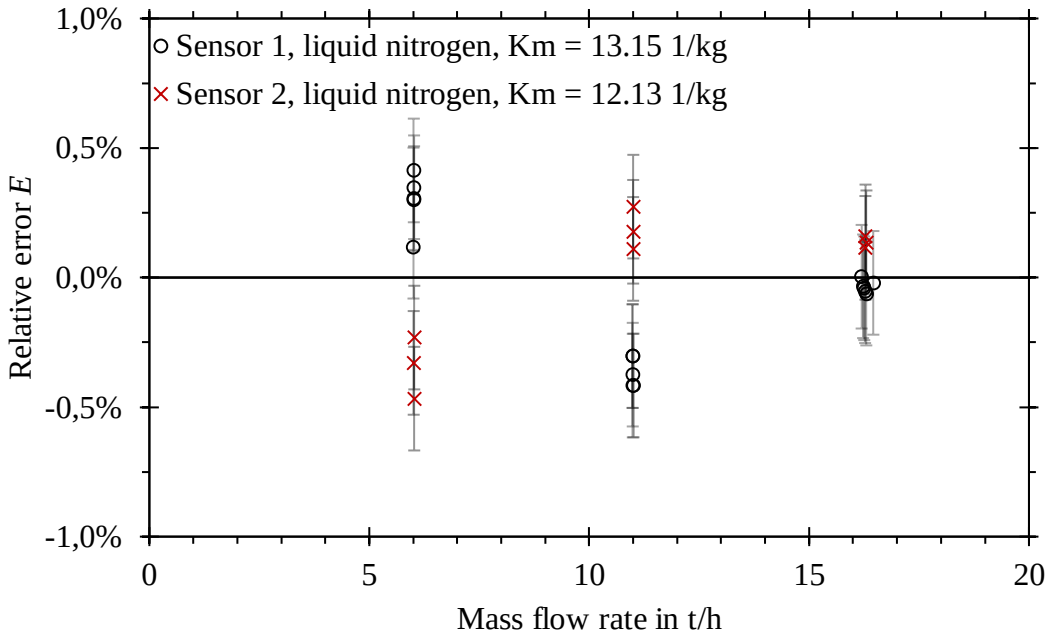

Figure 9.3: Error curves for the measurement of liquid nitrogen. Error bars denote expanded uncertainty for $k = 2$.

It was also verified that the application of a Hall sensor instead of a coil for capturing the oscillation signal in cryogenic conditions is possible (Figure 9.4). Differences between coil and Hall sensors were within the measurement uncertainty limits.

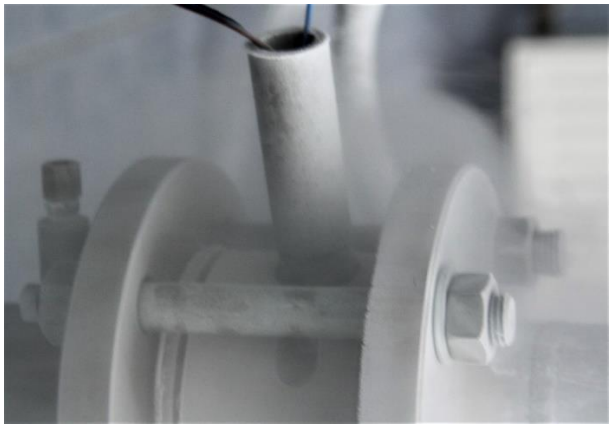

Figure 9.4: Hall sensor mounted in the flowmeter body.

In the case of LNG, 30 measurements were made in total. The standard deviation of obtained results was 0,25% and the spread of results was equal to 1,04%, which is well below the MPEs stated by legal requirements. The error curve is demonstrated in Figure 9.5.

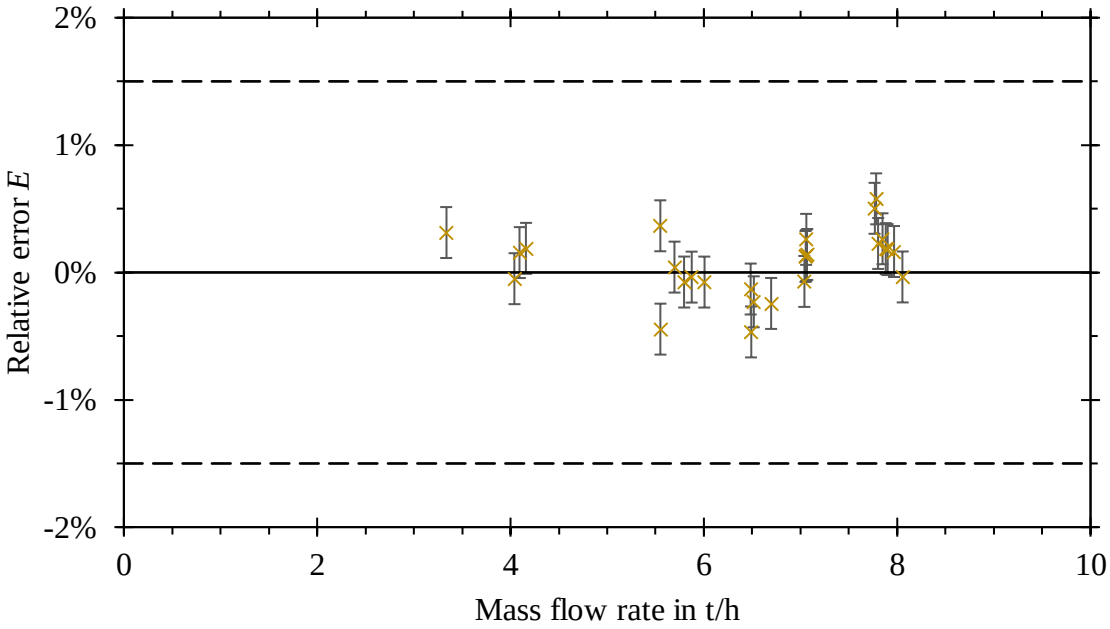

Figure 9.5: Error curve for the measurement of liquefied natural gas. Error bars denote expanded uncertainty for $k = 2$ and dashed lines denote the legal requirements.

Figure 9.6 and Figure 9.7 collect error curves for water and cryogenic fluids. Below $Re \approx 100\,000$ positive errors are found. Because of the low viscosity of the cryogenic fluids, both for the case of liquid nitrogen and LNG the Reynolds number was above 200 000, even though the mass flow rate range was lower in comparison to water calibration. This is favorable for LNG applications, as nonlinearities in this *Re* range are smaller.

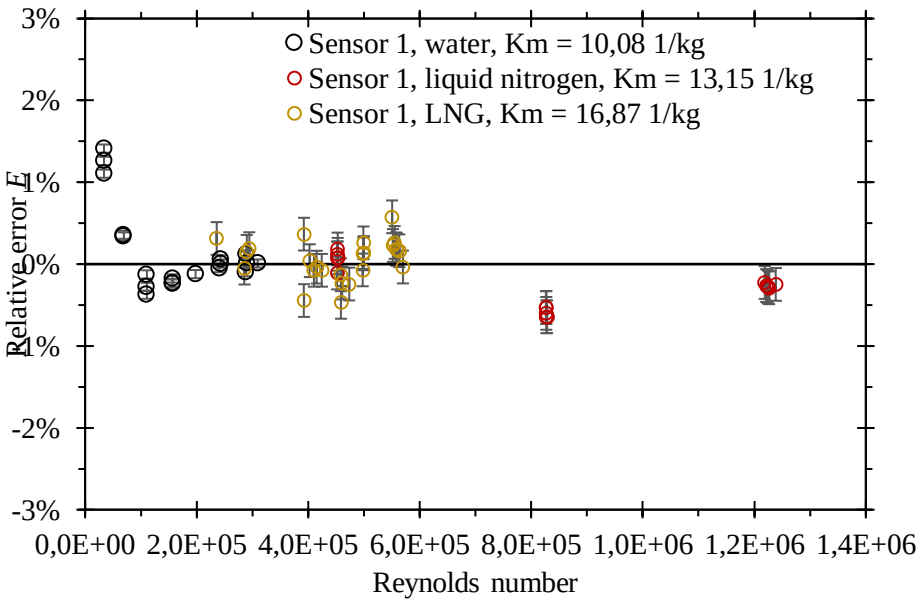

Figure 9.6: Error curves for various fluids, sensor 1. Error bars denote expanded uncertainty for $k = 2$.

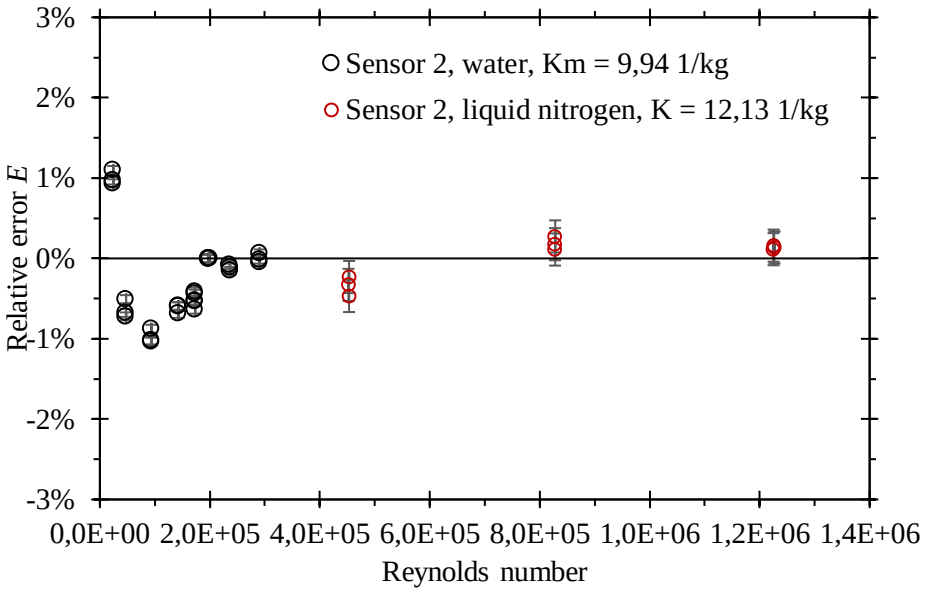

Figure 9.7: Error curves for various fluids, sensor 2. Error bars denote expanded uncertainty for $k = 2$.

In the case of unloading the LNG tanker truck, the truck was supplied with an evaporator instead of a pump. For that reason besides the liquid phase, a gas phase was flowing at the end of the unloading process. An increase in temperature and a decrease in density was noted (Figure 9.8). In such conditions, the error of the mechanical oscillator flowmeter exceeded 1,5% as it is not intended for multiphase flow measurement.

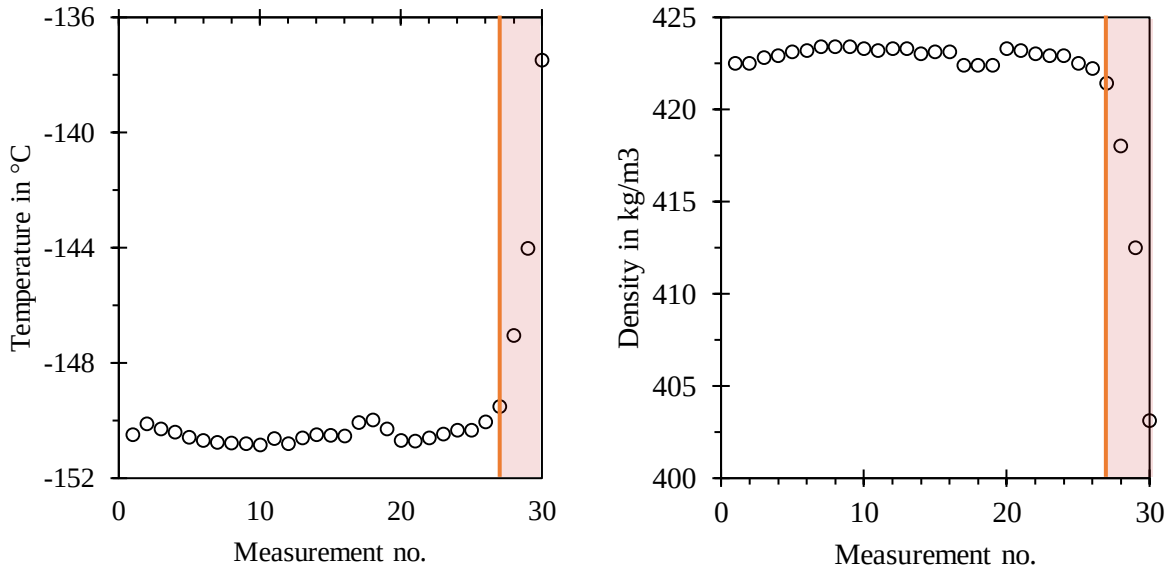

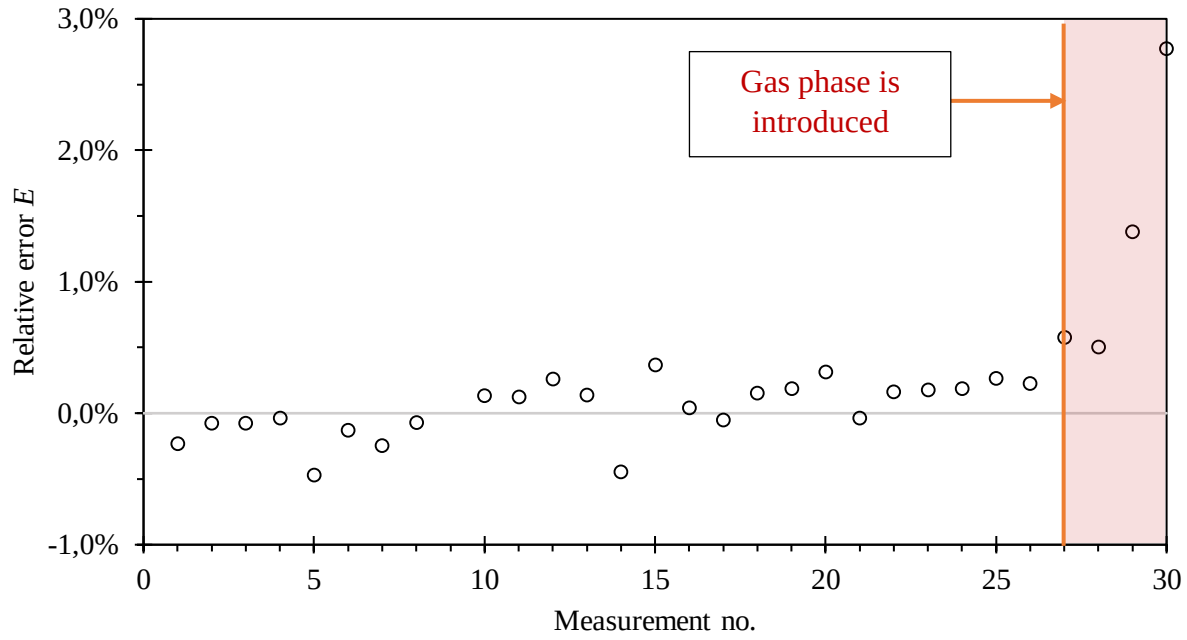

Figure 9.8: Temperature, density and relative mass measurement error by mechanical oscillator flowmeter for subsequent measurements. The effects of multiphase flow at the end of the truck unloading are visible.

Fortunately, this is not a real issue. At present, the entire load of the tanker truck is delivered to a single customer. The transferred mass of LNG is determined by weighing the truck twice, when it is full and empty. If flowmeters were introduced, then the load would be split among smaller customers and no gas phase would be present to disturb the measurement.

In summary, basing on the experimental results, the potential of the flowmeter was ultimately confirmed. The author came to a conclusion that the application range of mechanical oscillator flowmeter may be extended to cryogenic fluids. In terms of metrological properties, the studied prototype meets the legal requirements for LNG measurement.

The experiments posed a significant organizational effort and they were possible thanks to cooperation with PGNiG and PSG companies. At the time of writing the thesis, PGNiG has stated interest in investing in this measurement method for the measurement of LNG at local regasification plants in Poland so the work presented in the thesis found a direct application in the industry.

Chapter 10

Summary

10.1 Main contributions

The thesis investigates the metrological and operational properties of mechanical oscillator flowmeters with the objective to broaden their application range. The thesis focused on a particular design of the flowmeter that was validated in the industrial environment. The character of the thesis was mostly experimental and a great effort was made to ensure traceability of the measurement equipment used for the study. Computer modelling has also made a considerable contribution to the work. The main results of the thesis are as follows:

1. A CFD model of a mechanical oscillator flowmeter was developed and validated. Its sensitivity to grid and time step size was assessed. Best practices concerning problem setup were presented and encountered difficulties were outlined. The influence of the turbulence model and dynamic mesh approach on simulation results was studied. The developed model provided insight into the principle of operation of the flowmeter and allowed for design exploration.

2. It was demonstrated that the linearity of the flowmeter calibration curve is among others a result of the shape of the inlet flow profile, which is a function of Reynolds number. A cost-effective method of improving the linearity was examined. If nonlinearity of 0,5% is taken as a threshold value, then the rangeability of the flowmeter was increased from 6:1 to 26:1 at the cost of a 40% increase in pressure losses. It will find application in cases where low pressure losses are not critically important.

3. Previous studies on the optimal shape of the oscillator were verified and extended. It was demonstrated that only dynamic cases provide quantitively correct results. The significance of the individual components of the oscillator was shown. Experiments allowed outlining design recommendations for the measurement of fluids of low density. In the case of larger density, fluid damping and apparent mass effects become important and the optimal shape will be different. However, the developed numerical model and

measurement procedures allow extending the scope of the study in the future. Experiments confirmed that maximizing the nondimensional stiffness F is justified. It improves the threshold flow rate for flowmeter operation and reduces the influence of bearing wear. It was proven that in the case of disturbances that scale with mass properties of the oscillator, the nondimensional stiffness F is not the only important factor affecting flowmeter performance.

4. Valuable data regarding installation requirements were collected. It was demonstrated that the stream divider in its current form is highly effective in reordering the flow profile. The conducted experimental study has verified that previous recommendations on inlet pipe lengths may be relaxed. It was shown that the impact of disturbance sources not covered by the study can be verified numerically in the future, with the use of flatness parameter and swirl number to evaluate resultant flow profiles. It was shown that the mechanical oscillator flowmeter should not be applied for flow measurement if the flow pulsation is present and its frequency is in the lock-in range. Possible errors for specific amplitude thresholds have been determined. Methods of modifying the working frequency of flowmeter that could be applied to move outside the lock-in range were given. Of practical significance was also the study on alternative methods of oscillation frequency measurement. Inductive proximity sensors, Hall sensors and fast piezoelectric pressure sensors extend the application range of mechanical oscillator flowmeter.

5. Regarding the inlet pipe surface roughness, the study uncovered that it is insignificant even for $14 \cdot 10^4\, Ra/D$ in the range of Re = (25 000 – 70 000).

6. A study on cryogenic fluids was conducted with the use of liquid nitrogen and liquefied natural gas. It was a huge organizational effort and required preparing an ATEX-certified measurement system. In the study, it was verified that the mechanical oscillator flowmeter not only operates properly in cryogenic conditions, but also meets the legal criteria of LNG measurement. These experiments ultimately confirmed the potential of the solution. At the time of writing the thesis, PGNiG has stated interest in investing in this measurement method for the measurement of LNG at local regasification plants in Poland. Influence of density on the calibration constant was verified and it was shown that the existing formulas require a revision.

As listed above, all the objectives stated in Chapter 3 of thesis were accomplished. The problem of increasing the application range of mechanical oscillator flowmeters was solved through modelling of their metrological and operational properties.

10.2 Future study directions

There are future study directions that spawn from the findings presented in the thesis. However, most of them require huge investment either in research apparatus, computing power or manufacturing equipment.

1. Flow conditioners did not reduce installation requirements, as they need to be installed at a certain distance upstream of the flowmeter. It was found that the required distance exceeded the distance for which studied disturbance sources had any impact on the installation error. However, disturbances introducing swirl are harder to eliminate. It can be verified if flow straighteners could apply in this case, e.g. fin-type, tube type or a folded vane.

2. Additional insight into the principles of flowmeter operation can be provided by performing a CFD simulation with Large Eddy Simulation (LES) or Scale Adaptive Simulation (SAS) turbulence model. It was successfully applied in the case of vortex flowmeters (Penttinen and Nilsson, 2015).

3. A multiple-objective optimization with the use of the developed numerical model may be performed for the cases of high-density or high-viscosity fluids.

4. Durability tests can be performed for various materials, coating, bearing types and manufacturing methods. The methodology for the study and apparatus for bearing durability testing in laboratory conditions was devised.

5. Threshold amplitude pulsation that does not yet introduce additional measurement errors should be determined. Influence of the pulsation on the measurement errors outside the lock-in range should be studied.

6. Correction factors for density and temperature should be further investigated with the use of experiments on different fluids and with the use of CFD.

7. The study on the influence of roughness should be extended for larger values of Reynolds number, where roughness impact on the flow profile is the most significant. Existing measurement stands did not allow for larger flow rates for the studied nominal diameter.

10.3 Acknowledgements

The author wishes to gratefully acknowledge the support of PGNiG and Vein companies for organizing calibration using liquid nitrogen and the support of PGNiG and PSG companies for organizing calibration using liquefied natural gas.

Computations were performed on a high-performance cluster Cray XC40 Okeanos thanks to the support of Interdisciplinary Centre for Mathematical and Computational Modelling at University of Warsaw through grant GB74-0.

This work was partially supported by the Warsaw University of Technology, Faculty of Mechatronics Dean's Grant.

References

Adamczak, S. (2008) *Pomiary geometryczne powierzchni: zarysy kształtu, falistość i chropowatość*. Wydawnictwa Naukowo-Techniczne.

AIAA (1998) *Guide for the Verification and Validation of Computational Fluid Dynamics Simulations*. Reston: American Institute of Aeronautics and Astronautics. doi: doi.org/10.2514/4.472855.001.

Badger Meter Europe (1985) *LS - 8904 - HPV Catalog*. Stuttgart.

Bahrton, P. S. (1981) 'Oscillating vane flowmeter'. US Patent 4.409.851.

Baker, R. C. (2016) *Flow Measurement Handbook*. Cambridge University Press. doi: doi.org/10.1017/CBO9781107054141.

Balasubramanian, S. and Skop, R. A. (1996) 'A nonlinear oscillator model for vortex shedding from cylinders and cones in uniform and shear flows', *Journal of Fluids and Structures*, 10, pp. 197–214. doi: doi.org/10.1006/jfls.1996.0013.

Bandi, M. M. *et al.* (2013) 'A pendulum in a flowing soap film', *Physics of Fluids*, 25(4). doi: doi.org/10.1063/1.4800057.

Bartran, D. S. *et al.* (1999) 'Flow induced vibration of thermowells', *ISA Transactions*, 38(2), pp. 123–132. doi: doi.org/10.1016/S0019-0578(99)00010-5.

Bek, J. and Turkowski, M. (1987) 'Nowy krajowy przepływomierz wibracyjny - właściwości metrologiczne i eksploatacyjne', *PAK*, 11.

Blacharski, T. *et al.* (2016) 'Wpływ terminalu LNG na rozwój krajowego rynku gazu ziemnego', *Przegląd gazowniczy*, 2(50), pp. 8–11.

Blevins, R. D., Tilden, B. W. and Martens, D. . (1998) 'Vortex-induced vibration and damping of thermowells', *Journal of Fluids and Structures*, 12(4), pp. 427–444. doi: doi.org/10.1006/jfls.1997.0150.

Boszniak, L. L. and Słowskij, W. M. (1976) 'Raschodomier dla żikdostiej i gazow'. ZSRR Patent 523282.

Carlander, C. and Delsing, J. (2000) 'Installation effects on an ultrasonic flow meter with

implications for self diagnostics', *Flow Measurement and Instrumentation*, 11, pp. 109–122. doi: doi.org/10.1016/S0955-5986(00)00005-4.

Çarpinlioğlu, M. Ö. and Gündoğdu, M. Y. (2001) 'Presentation of a test system in terms of generated pulsatile flow characteristics', *Flow Measurement and Instrumentation*, 12(3), pp. 181–190. doi: doi.org/10.1016/S0955-5986(01)00019-X.

Cheesewright, R., Clark, C. and Bisset, D. (1999) 'Understanding the experimental response of Coriolis massflow meters to flow pulsations', *Flow Measurement and Instrumentation*, 10(4), pp. 207–215. doi: doi.org/10.1016/S0955-5986(99)00014-X.

Ciemnołońska, M. and Rosłonek, G. (2018) 'SMOK - innowacyjne rozwiązanie dla rynku małego LNG', *PGNiG INFO*, 2(84), pp. 3–5.

DeCarlo, J. P. (1978) 'Oscillating wing flowmeter'. US Patent 4.092.859.

DeCarlo, J. P. (1982) 'Oscillating wing flowmeter: a new concept in large line size gas flow measurement', *ISA Trans.;(United States)*, 21(2).

Dobrowolski, B. and Kabza, Z. (1992) *Teoretyczna analiza wpływu osiowosymetrycznej deformacji pola prędkości i zawirowania strugi na właściwości metrologiczne zwężek pomiarowych*. Wyższa Szkoła Inżynierska w Opolu.

Dz. U. 2016 Poz. 815 (2016) *Rozporządzenie Ministra Rozwoju z dnia 2 czerwca 2016 r. w sprawie wymagań dla przyrządów pomiarowych*.

EURAMET (2010) *Metrology for Liquefied Natural Gas*. Available at: https://www.euramet.org/research-innovation/search-research-projects/details/project/metrology-for-liquefied-natural-gas (Accessed: 18 January 2019).

EURAMET (2017) *Metrological support for LNG and LBG as transport fuel*. Available at: https://www.euramet.org/research-innovation/search-research-projects/details/project/metrological-support-for-lng-and-lbg-as-transport-fuel (Accessed: 18 January 2019).

European Accreditation Laboratory Committee (2013) *Evaluation of the uncertainty of measurement in calibration, EA04/02 M.*

Facchinetti, M. L., Langre, E. De and Biolley, F. (2002) 'Vortex shedding modeling using diffusive van der Pol oscillators', *Comptes Rendus Mecanique*, 330(7), pp. 451–456. doi:

doi.org/10.1016/S1631-0721(02)01492-4.

Facchinetti, M. L., Langre, E. De and Biolley, F. (2004) ‘Coupling of structure and wake oscillators in vortex-induced vibrations’, *Journal of Fluids and Structures*, 19(2), pp. 123–140. doi: doi.org/10.1016/j.jfluidstructs.2003.12.004.

Fani, A. and Gallaire, F. (2014) ‘The motion of a 2D pendulum in a channel subjected to an incoming flow’, *Journal of Fluid Mechanics*, 764, pp. 5–25. doi: doi.org/10.1017/jfm.2014.670.

Ferziger, J. H. and Peric, M. (1996) ‘Further discussion of numerical errors in CFD’, *International Journal for Numerical Methods in Fluids*, 23, pp. 1263–1274. doi: doi.org/10.1002/(SICI)1097-0363(19961230)23:12<1263::AID-FLD478>3.0.CO;2-V.

Gibson, J. E. (1968) *Nieliniowe układy sterowania automatycznego*. Warszawa: WNT.

GIIGNL (2017) *LNG custody transfer handbook*. 7th edn. Paris.

Giné, J. (2013) ‘On the determination of the limit cycles using the harmonic balance method’, *Journal of Mathematical Physics*, 54(10). doi: doi.org/10.1063/1.4826105.

Goltsman, A. *et al.* (2019) ‘Generation of sinusoidal pulsating flows in the channels of experimental setups’, *Flow Measurement and Instrumentation*, 66(April 2019), pp. 60–66. doi: doi.org/10.1016/j.flowmeasinst.2019.02.006.

Górecki, J. and Kubas, K. (2005) ‘Oscillatory mechanical flowmeter - theoretical analysis of operation’, *Metrology and Measurement Systems*, 12(2), pp. 183–194.

Grevendonk, W., Herreman, W. and De Bock, A. (1970) ‘Measurements on the viscosity of liquid nitrogen’, *Physica*, 46(4), pp. 600–604. doi: doi.org/10.1016/0031-8914(70)90148-5.

Gutkowski, L. and Turkowski, M. (1985) ‘Przepływomierz wibracyjny’. PRL Patent 135544.

Hayashi, C. (1968) *Drgania nieliniowe w układach fizycznych*. Warszawa: WNT.

Hebrard, P., Malard, L. and Strzelecki, A. (1992) ‘Experimental study of a vortex flowmeter in pulsatile flow conditions’, *Flow Measurement and Instrumentation*, 3(3), pp. 173–186. doi: doi.org/10.1016/0955-5986(92)90033-2.

Heckle, M. (1971) ‘Ein neues Durchflussmessverfahren mit Frequenzausgang’, *Messtechnik*, 9, pp. 207–214.

Heckle, M. (1973) ‘Ein neues digitales Verfahren zur Durchflußmessung’, *Chemie Ingenieur Technik*. Wiley Online Library, 45(6), pp. 402–407. doi: doi.org/10.1002/cite.330450615.

Heckle, M. (1974) ‘Method and apparatus for measuring the flow rate of fluids such as gases or liquids’. U.S. Patent 3,824,855.

Hellevik, K. and Gudmestad, O. T. (2017) ‘Limit cycle oscillations at resonances’, in *IOP Conference Series: Materials Science and Engineering*. IOP Science. doi: doi.org/10.1088/1757-899X/276/1/012020.

Hilgenstock, A. and Ernst, R. (1996) ‘Analysis of installation effects by means of computational fluid dynamics—CFD vs experiments?’, *Flow Measurement and Instrumentation*, 7(3–4), pp. 161–171. doi: doi.org/10.1016/S0955-5986(97)88066-1.

Hogendoorn, J., Boer, A. and Danen, H. (2007) ‘An Ultrasonic Flowmeter for Custody Transfer Measurement of LNG: A Challenge for Design and Calibration’, in *25 th International North Sea Flow Measurement Workshop*, pp. 1–16.

International Organization for Standardization (1980) *Measurement of fluid flow by means of pressure differential devices inserted in circular cross-section conduits running full*. ISO Standard No. 5167.

International Organization for Standardization (1998) *ISO 11631:1998 Measurement of fluid flow. Methods of specifying flowmeters performance*. ISO Standard No. 11631.

International Organization for Standardization (2003a) *ISO 5167-1:2003 Measurement of fluid flow by means of pressure differential devices inserted in circular cross-section conduits running full — Part 1: General principles and requirements*.

International Organization for Standardization (2003b) *ISO 5167-2:2003 Measurement of fluid flow by means of pressure differential devices inserted in circular cross-section conduits running full — Part 2: Orifice plates*.

International Organization for Standardization (2003c) *ISO 5167-3:2003 Measurement of fluid flow by means of pressure differential devices inserted in circular cross-section conduits running full — Part 3: Nozzles and Venturi nozzles*.

International Organization for Standardization (2003d) *ISO 5167-4:2003 Measurement of fluid flow by means of pressure differential devices inserted in circular cross-section conduits running full — Part 4: Venturi tubes*.

International Organization for Standardization (2007) *Measurement of fluid flow by means of pressure-differential devices—Guidelines for the specification of orifice plates, nozzles and Venturi tubes beyond the scope of ISO 5167*. Technical Report No. 15377.

International Organization for Standardization (2018) *Measurement of fluid flow in closed conduits. Guidelines on the effects of flow pulsations on flow-measurement instruments*. ISO/TR 3313.

Jan, Y. and Sheu, T. W. (2004) 'A numerical confirmation of the dual body vortex flowmeter design', *Computers and Fluids*, 33(9), pp. 1157–1174. doi: doi.org/10.1016/j.compfluid.2003.09.004.

Jeżowiecka-Kabsch, K. and Szewczyk, H. (2001) *Mechanika płynów*. Wrocław.

Johnson, A. (2001) 'Applying vortex flow metering technology in demanding process applications', *Proceedings of the Flow Measurement*.

Joint Committee for Guides in Metrology (2008) 'Evaluation of measurement data—Guide to the expression of uncertainty in measurement', *JCGM*, 100.

Kabacinski, M., Lachowicz, C. and Pospolita, J. (2008) 'Analysis of flowing fluid effect on flow averaging tube', *TASK Quarterly*, 12(3), pp. 217–226.

Kabaciński, M., Lachowicz, C. and Pospolita, J. (2013) 'Numerical analysis of flow averaging tubes in the vortex-shedding regime', *The Archive of Mechanical Engineering*, LX(2), pp. 283–297. doi: doi.org/10.2478/meceng-2013-0018.

Kabaciński, M., Pospolita, J. and Zamorowski, R. (2007) 'Właściwości metrologiczne i możliwości zastosowania przepływomierzy wirowych', *Pomiary Automatyka Robotyka*, 11, pp. 13–20.

Van der Kam, P. M. and Dam, A. M. (1993) 'Large turbine meters for custody transfer measurements : the renovation of the Gasunie export stations', *Flow Measurement and Instrumentation*, 4(2), pp. 91–98. doi: doi.org/10.1016/0955-5986(93)90019-F.

Kremlewskij, P. P. (1989) *Raschodomiery i szczіotczіki koliczestwa*. Leningrad: Maszynostrojenie.

Lagasse, F. H. (1944) 'Means for measuring the velocity and volume of fluids'.

Lavante, E. V, Humener, T. and Schieber, W. M. (2001) 'Numerical investigation of the flow

field in a 2-stage turbine flow meter', in *Proc. of the 9th Int. Conf. on Flow Measurement*, pp. 8–10.

Lavante, E. Von *et al.* (1999) 'Optimization of acoustic signals in a vortex-shedding flowmeter using numerical simulation', *International Journal of Heat and Fluid Flow*, 20(4), pp. 402–404. doi: doi.org/10.1016/S0142-727X(99)00004-1.

Lucas, P. and Pelevic, N. (2017) 'Flow metering', in *LNG workshop*. Noordwijk.

Lutz, K. (1973) 'Der neuartige Schwingkörper----Durchflußmesser Rotaflux', *CZ-Chemie-Technik*, 7, pp. 286–289.

Mahulikar, S. P. and Sane, S. (2005) 'Theoretical Analysis of Experimentally Observed Perplexing Calibration Characteristics of Ball-in-Vortex', *Journal of Fluids Engineering*, 127(5), pp. 1021–1028. doi: doi.org/10.1115/1.1988342.

Menter, F. R. (1994) 'Two-Equation Eddy-Viscosity Turbulence Models for Engineering Applications', *AIAA Journal*, 32(8). doi: doi.org/10.2514/3.12149.

Merzkirch, W. *et al.* (2005) *Fluid mechanics of flow metering*. Berlin: Springer.

Miau, J. J. *et al.* (2002) 'A study on signal quality of a vortex flowmeter downstream of two elbows out-of-plane', *Flow Measurement and Instrumentation*, 13(3), pp. 75–85. doi: doi.org/10.1016/S0955-5986(02)00027-4.

Miau, J. J., Hu, C. C. and Chou, J. H. (2000) 'Response of a vortex flowmeter to impulsive vibrations', *Flow Measurement and instrumentation*. Elsevier, 11(1), pp. 41–49. doi: doi.org/10.1016/S0955-5986(99)00018-7.

Morrison, G. L., Deotte, R. E. and Beam, E. J. (1992) 'Installation effects upon orifice flowmeters', *Flow Measurement and Instrumentation*, 3(2), pp. 89–93. doi: doi.org/10.1016/0955-5986(92)90005-P.

Mottram, R. C. (1991) 'Vortex flowmeters - Installation effects', *Flow Measurement and Instrumentation*, 2(1), pp. 56–60. doi: doi.org/10.1016/0955-5986(91)90056-W.

Mottram, R. C. (1992) 'Introduction: An overview of pulsating flow measurement', *Flow Measurement and Instrumentation*, 3(3), pp. 114–117. doi: doi.org/10.1016/0955-5986(92)90027-3.

Orchini, A., Kellay, H. and Mazzino, A. (2015) 'Galloping instability and control of a rigid

pendulum in a flowing soap film', *Journal of Fluids and Structures*. Elsevier, 56(July 2015), pp. 124–133. doi: doi.org/10.1016/j.jfluidstructs.2015.04.006.

Özdinç Çarpinlioğlu, M. and Yaşar Gündoğdu, M. (2001) 'A critical review on pulsatile pipe flow studies directing towards future research topics', *Flow Measurement and Instrumentation*, 12(3), pp. 163–174. doi: doi.org/10.1016/S0955-5986(01)00020-6.

Ozgoren, M. *et al.* (2015) 'Flow characteristics around a vortex flow meter via CFD and PIV methods', in *10th Pacific Symposium on Flow Visualization and Image Processing*. Naples.

Parry, A. (2001) 'Computation of fluid-rigid body dynamic interaction in flowmeters', *Flow Measurement*.

Peisker, I. and Bohac, Z. (1980) 'Prutokomer na tekutiny'. CSRS Patent 201360.

Penttinen, O. and Nilsson, H. (2015) 'Large Eddy Simulation and Laser Doppler Velocimetry on a vortex flow meter model', in *International Symposium for Fluid Flow Measurements*.

PGNiG (2018) *Small-scale LNG market to grow driven by smaller customers*. Available at: http://en.pgnig.pl/news/-/news-list/id/pgnig-small-scale-lng-market-to-grow-driven-by-smaller-customers/newsGroupId/1910852?changeYear=2018&currentPage=1 (Accessed: 18 January 2019).

Pochwała, S., Kabaciński, M. and Pospolita, J. (2012) 'Influence of typical flow disturbing elements on the flow rate in selected averaging Pitot tubes', *TASK Quarterly*, (3–4), pp. 219–228.

Pochwala, S. and Pospolita, J. (2016) 'Analysis of Applicability of Flow Averaging Pitot Tubes in the Areas of Flow Disturbance', *Metrology and Measurement Systems*, 23(1), pp. 71–84. doi: doi.org/10.1515/mms-2016-0005.

Pospolita, J. (2004) *Pomiary strumieni płynów*. Opole.

Ramesh, K., Murua, J. and Gopalarathnam, A. (2015) 'Limit-cycle oscillations in unsteady flows dominated by intermittent leading-edge vortex shedding', *Journal of Fluids and Structures*, 55, pp. 84–105. doi: doi.org/10.1016/j.jfluidstructs.2015.02.005.

Reddy, H. (2004) 'Performance Evaluation of Static and Dynamic Load-Balancing Schemes for a Parallel Computational Fluid Dynamics Software (CFD) Application (Fluent) Distributed Across Clusters of Heterogeneous Symmetric Multiprocessor Systems', *IBM*

Redbooks.

Reynolds, O. (1895) 'IV. on the dynamical theory of incompressible viscous fluids and the determination of the criterion.', *Philosophical Transactions of the Royal Society of London.*, 186, pp. 123–164. doi: doi.org/10.1098/rsta.1895.0004.

Rota (1976) *Rotaflux - Schwingkoerper-Durchflussmesser Catalog*. Koln.

SAE (2017) *A methodology for assessing inlet swirl distortion. AIR 5686*.

Safinowski, M., Szudarek, M. and Szewczyk, R. (2017) *Capabilities of an open-source software, Elmer FEM, in finite element analysis of fluid flow*, *Advances in Intelligent Systems and Computing*. doi: doi.org/10.1007/978-3-319-48923-0_16.

Shih, T. *et al.* (1995) 'A New k-e Eddy Viscosity Model for High Reynolds Number Turbulent Flows', *Computers and Fluids*, 24(3), pp. 227–238. doi: doi.org/10.1016/0045-7930(94)00032-T.

Shimomura, T. (1980) 'Flow rate measuring instrument'. US Patent 4.343.192.

Singh, R. K., Singh, S. N. and Seshadri, V. (2009) 'Study on the effect of vertex angle and upstream swirl on the performance characteristics of cone flowmeter using CFD', *Flow Measurement and Instrumentation*, 20(2), pp. 69–74. doi: doi.org/10.1016/j.flowmeasinst.2008.12.003.

Skibina, L. V *et al.* (1985) 'Thermal expansion of the austenitic stainless steels and titanium alloys in the temperature range 5--300 K', *Cryogenics*, 25(1), pp. 31–32. doi: doi.org/10.1016/0011-2275(85)90092-X.

Spalart, P. and Allmaras, S. (1992) 'A One-Equation Turbulence Model for Aerodynamic Flows', in *30th aerospace sciences meeting and exhibit*, p. 439. doi: doi.org/10.2514/6.1992-439.

Spitzer, D. W. (2001) *Flow Measurement: Practical Guides for Measurement and Control*. ISA (Practical guide series).

Steger, J. L., Dougherty, F. C. and Benek, J. A. (1983) 'A chimera grid scheme.[multiple overset body-conforming mesh system for finite difference adaptation to complex aircraft configurations]', in *Advances in grid generation; Proceedings of the Applied Mechanics, Bioengineering, and Fluids Engineering Conference*. Houston: American Society of

Mechanical Engineers, pp. 59–69.

Stramigioli, S. and Van Dijk, M. (2008) ‘Energy conservative limit cycle oscillations’, *IFAC Proceedings Volumes,* 17(2), pp. 15666–15671. doi: doi.org/10.3182/20080706-5-KR-1001.02649.

Strzałkowski, T., Gutkowski, L. and Turkowski, M. (1989) ‘Wyniki badań właściwości metrologicznych i eksploatacyjnych przepływomierzy z oscylatorem mechanicznym’, *Gazeta Cukrownicza,* 97(5), pp. 91–93.

Strzelczyk, F. and Gosk, W. (2010) ‘Granice możliwości pomiarowej strumienia objętości w stanowiskach wzorcowych dużych przepływów wody’, *PAK*, 56(11), pp. 1298–1301.

Studzinski, W. *et al.* (1997) *White Paper on Orifice Meter Installation Configurations with and without Flow Conditioners*. Houston.

Svete, A. *et al.* (2012) ‘Development of a liquid-flow pulsator’, *Flow Measurement and Instrumentation,* 23(1), pp. 1–8. doi: doi.org/10.1016/j.flowmeasinst.2011.12.002.

Szudarek, M., Turkowski, M. and Twaróg, G. (2019) ‘Test Stand for Studying Flowmeter Performance in Presence of Pulsatile Flow’, in *International Conference Mechatronics,* pp. 157–163. doi: doi.org/10.1007/978-3-030-29993-4_20.

Takahashi, S. and Itoh, I. (1993) ‘Intelligent vortex flowmeter’, in *Proc. of International Conference of Flow Measurement FLOMEKO*, pp. 107–113.

Thaler, G. J. and Pastel, M. P. (1965) *Nieliniowe układy automatycznego sterowania*. Warszawa: WNT.

Tomasik, J. and Turkowski, M. (2007) *Raport z realizacji projektu badawczego pt. Badania nad wpływem mikrogeometrii powierzchni rurociągu na charakterystykę przepływomierza zwężkowego*. Warszawa.

Tomasik, J., Turkowski, M. and Zagozdzon, M. (2008) ‘Wpływ chropowatości rurociągu na wskazania przepływomierzy zwężkowych – nowe podejście do zagadnienia’, *Pomiary Automatyka Robotyka*, (5), pp. 5–8.

Turkowski, M. (1987a) *Pomiary przepływów*. Wydawnictwa Politechniki Warszawskiej.

Turkowski, M. (1987b) ‘Przepływomierz wibracyjny’. PRL Patent 144059.

Turkowski, M. (1987c) ‘Przepływomierz wibracyjny’. PRL Patent 144060.

Turkowski, M. (1988) ‘Analiza możliwości wykorzystania przepływomierzy z oscylatorem mechanicznym w cukrownictwie’, *Gazeta Cukrownicza*, 96(3), pp. 66–68.

Turkowski, M. (2002) ‘Dokumentacja Techniczno-Ruchowa typoszeregu przepływomierzy wibracyjnych Vibroflux VX’. Warszawa.

Turkowski, M. (2003a) ‘Mathematical model and numerical simulation of a mechanical oscillator flowmeter’, *Metrology and Measurement Systems*, 10(1), pp. 77–100.

Turkowski, M. (2003b) *Optymalizacja właściwości metrologicznych oraz rozwiązań konstrukcyjno-technologicznych przepływomierzy z oscylatorem mechanicznym*. Warszawa: OWPW.

Turkowski, M. (2003c) ‘Progress towards the optimisation of a mechanical oscillator flowmeter’, *Flow Measurement and Instrumentation*, 14(1–2), pp. 13–21. doi: 10.1016/S0955-5986(02)00091-2.

Turkowski, M. (2004) ‘Influence of fluid properties on the characteristics of a mechanical oscillator flowmeter’, *Measurement: Journal of the International Measurement Confederation*, 35(1), pp. 11–18. doi: 10.1016/j.measurement.2003.10.002.

Turkowski, M. (2018) *Metrologia przepływów*. Warszawa: OWPW.

Turkowski, M., Strzałkowski, T. and Dąbrowski, W. (2000) *Sprawozdanie merytoryczne z realizacji zadań wykonanych w ramach prac badawczo-rozwojowych podczas realizacji projektu celowego pt. ‘Uruchomienie produkcji nowej generacji przepływomierzy z oscylatorem mechanicznym’*. Warszawa.

Turkowski, M. and Szufleński, P. (2013) ‘New criteria for the experimental validation of CFD simulations’, *Flow Measurement and Instrumentation*, 34, pp. 1–10. doi: doi.org/10.1016/j.flowmeasinst.2013.07.003.

Wahed, A. K. E. L., Johnson, M. W. and Sproston, J. L. (1993) ‘Numerical study of vortex shedding from different shaped bluff bodies’, *Flow Measurement and Instrumentation*, 4(4), pp. 233–240. doi: doi.org/10.1016/0955-5986(93)90030-M.

Waugh, C. S. (1963) ‘Oscillating vane flowmeter’. US Patent 3.273.389.

Wildner, J. *et al.* (2018) ‘Nowa metoda wzorcowania stanowisk z kontrolnymi zbiornikami dzwonowymi’, in *Problems and Progress in Metrology PPM’2018*. Szczyrk.

Wildner, J. *et al.* (2019) ‘Calibration of Bell Prover Test Stands with Critical Flow Venturi Nozzle’, in *International Conference Mechatronics,* pp. 172–177.

Williamson, C. H. K. and Govardhan, R. (2004) ‘Vortex-Induced Vibrations’, *Annual Review of Fluid Mechanics,* 36(1), pp. 413–455. doi: doi.org/10.1146/annurev.fluid.36.050802.122128.

WysokieNapiecie.pl (2018) *Gaz bezpiecznie dotrze tam, gdzie jest potrzebny*. Available at: https://wysokienapiecie.pl/14176-transport_gazu_w_polsce/ (Accessed: 2 February 2019).

Yeh, T. T. (1991) ‘Effects of pipe elbows and tube bundles on selected types of flowmeters’, *Flow Measurement and Instrumentation,* 2(1), pp. 4–13. doi: doi.org/10.1016/0955-5986(91)90050-2.

Zhao, H. and Peng, L. (2014) ‘CFD Aided Investigation of Multipath Ultrasonic Gas Flow Meter Performance Under’, *IEEE Sensors Journal,* 14(3). doi: doi.org/10.1109/JSEN.2013.2290863.

Appendix

Uncertainty analysis

A.1.1 Calibration using water

Volumetric calibration constant *K* was calculated as a number of pulses *n* generated by mechanical oscillator flowmeter divided by the reference volume of water *V* which was measured with a volumetric tank:

$$K = \frac{n}{V} \tag{A.1}$$

Combined uncertainty *u(K)* is equal to:

$$u(K) = \sqrt{\left(\frac{\partial K}{\partial n} \cdot u(n)\right)^2 + \left(\frac{\partial K}{\partial V} \cdot u(V)\right)^2} \tag{A.2}$$

Table A.1*:* Uncertainty budget for calibration using water.

Quantity	**Unit**	**Value** x_i	$u(x_i)$	**Probability distribution**	**Sensitivity coefficient** $c(x_i)$	$c(x_i) \cdot u(x_i)$ **in pulse/dm^3**	**% of total**
n	pulse	10 060	0,41	triangular	0,001	0,00041	3%
V	dm^3	1 000	0,25	normal	-0,01	-0,0025	97%
K	**pulse/dm^3**	**10,060**	**0,0025**				**100%**

The uncertainty budget is presented in Table A.1. Relative standard uncertainty of volumetric calibration constant *K* equals 0,025%.

A.1.2 Calibration using air, low-pressure air facility

Volumetric calibration constant K was calculated as a number of pulses n generated by mechanical oscillator flowmeter divided by the reference volume of air V_T which was measured with a turbine gas meter. Correction for pressure and temperature difference between unit under test (subscript u) and turbine gas meter (subscript t) was taken into account:

$$K = n \cdot \frac{p_u T_t}{V_t (p_u - \Delta p) T_u} \tag{A.3}$$

Combined uncertainty $u(K)$ is equal to:

$$u(K) = \sqrt{\left(\frac{\partial K}{\partial n} \cdot u(n)\right)^2 + \left(\frac{\partial K}{\partial p_u} \cdot u(p_u)\right)^2 + \left(\frac{\partial K}{\partial \Delta p} \cdot u(\Delta p)\right)^2 + \left(\frac{\partial K}{\partial T_t} \cdot u(T_t)\right)^2 + \left(\frac{\partial K}{\partial T_u} \cdot u(T_u)\right)^2 + \left(\frac{\partial K}{\partial V_t} \cdot u(V_t)\right)^2} \tag{A.4}$$

Table A.2: Uncertainty budget for calibration using air at the low-pressure facility.

Quantity	**Unit**	**Value** x_i	$u(x_i)$	**Probability distribution**	**Sensitivity coefficient** $c(x_i)$	$c(x_i) \cdot u(x_i)$ **in pulse/dm^3**	**% of total**
n	pulse	1619	0,41	triangular	$5{,}1 \cdot 10^{-4}$	$2{,}1 \cdot 10^{-4}$	3%
p_u	Pa	100864	5,77	rectangular	$-6{,}5 \cdot 10^{-5}$	$-3{,}7 \cdot 10^{-4}$	10%
Δp	Pa	794	1,15	rectangular	$-8{,}2 \cdot 10^{-3}$	$-9{,}5 \cdot 10^{-6}$	0%
T_t	K	296,75	0,12	rectangular	2,77	$3{,}2 \cdot 10^{-4}$	7%
T_u	K	296,55	0,12	rectangular	-2,77	$-3{,}2 \cdot 10^{-4}$	7%
V_t	dm^3	1985,9	2,48	normal	$-4{,}14 \cdot 10^{-4}$	$-1{,}0 \cdot 10^{-3}$	73%
K	**pulse/dm^3**	**0,803**	**0,0012**				**100%**

The uncertainty budget is presented in Table A.2. Relative standard uncertainty of volumetric calibration constant K equals 0,15%.

A.1.3 Calibration using air, bell prover

Volumetric calibration constant K was calculated as a number of pulses n generated by mechanical oscillator flowmeter divided by the reference volume of air V_T which was measured with a turbine gas meter. Correction for pressure and temperature difference between unit under test (subscript u) and turbine gas meter (subscript t) was taken into account:

$$K = n \cdot \frac{(p_a + p_u)T_b}{V_b(p_a + p_b)T_u} \tag{A.5}$$

where p_a is the atmospheric pressure. Combined uncertainty $u(K)$ is equal to:

$$u(K) = \sqrt{\left(\frac{\partial K}{\partial n}\cdot u(n)\right)^2 + \left(\frac{\partial K}{\partial p_u}\cdot u(p_u)\right)^2 + \left(\frac{\partial K}{\partial p_b}\cdot u(p_b)\right)^2 + \left(\frac{\partial K}{\partial T_b}\cdot u(T_b)\right)^2 + \left(\frac{\partial K}{\partial T_u}\cdot u(T_u)\right)^2 + \left(\frac{\partial K}{\partial V_b}\cdot u(V_b)\right)^2} \tag{A.6}$$

Table A.3*:* Uncertainty budget for calibration using air at the ball prover test stand.

Quantity	**Unit**	**Value** x_i	$u(x_i)$	**Probability distribution**	**Sensitivity coefficient** $c(x_i)$	$c(x_i)\cdot u(x_i)$ **in pulse/dm^3**	**% of total**
n	pulse	515	0,41	triangular	$4{,}8\cdot10^{-3}$	$2{,}0\cdot10^{-3}$	34%
p_a	Pa	101820	5,77	rectangular	$2{,}0\cdot10^{-4}$	$1{,}2\cdot10^{-3}$	12%
p_u	Pa	140	5,20	rectangular	$2{,}4\cdot10^{-5}$	$1{,}3\cdot10^{-4}$	0%
p_b	Pa	1000	5,77	rectangular	$-2{,}4\cdot10^{-3}$	$-1{,}4\cdot10^{-3}$	0%
T_b	K	298,35	0,12	rectangular	$8{,}4\cdot10^{-3}$	$9{,}6\cdot10^{-4}$	8%
T_u	K	298,55	0,12	rectangular	$-8{,}4\cdot10^{-3}$	$-9{,}6\cdot10^{-4}$	8%
V_b	dm^3	204,979	0,17	normal	$-1{,}2\cdot10^{-2}$	$-2{,}1\cdot10^{-3}$	38%
K	**pulse/dm^3**	**1,308**	**0,0031**				**100%**

The uncertainty budget is presented in Table A.3. Relative standard uncertainty of volumetric calibration constant K equals 0,24%.

A.1.4 Calibration using liquid nitrogen and LNG

Mass calibration constant K_m was calculated as a number of pulses n generated by mechanical oscillator flowmeter divided by the reference mass of liquid nitrogen m which was measured with the Coriolis flowmeter.

$$K_m = \frac{n}{m} \tag{A.7}$$

Combined uncertainty $u(K)$ is equal to:

$$u(K_m) = \sqrt{\left(\frac{\partial K_m}{\partial n} \cdot u(n)\right)^2 + \left(\frac{\partial K_m}{\partial m} \cdot u(m)\right)^2} \tag{A.8}$$

Table A.4*:* Uncertainty budget for calibration using cryogenic fluids.

Quantity	**Unit**	**Value x_i**	**$u(x_i)$**	**Probability distribution**	**Sensitivity coefficient $c(x_i)$**	**$c(x_i) \cdot u(x_i)$ in pulse/dm^3**	**% of total**
n	pulse	14 303	6,8	triangular	0,0012	0,0080	5%
m	kg	846,7445	1,7	normal	-0,020	-0,034	95%
K_m	**pulse/kg**	**16,892**	**0,035**				**100%**

The uncertainty budget is presented in Table A.4. Relative standard uncertainty of mass calibration constant K_m equals 0,208%.

A.1.5 Density correction coefficient *r*

Density correction coefficient was calculated basing on two calibration constants measured for two fluids of different density. The influence of temperature was accounted for by correction coefficient k_T.

$$r = \frac{K_{m1}^2 \rho_1 - K_{m2}^2 \rho_2 \frac{1}{k_T^{\ 2}}}{K_{m2}^2 \rho_2^2 - K_{m1}^2 \rho_1^2} \tag{A.9}$$

Combined uncertainty *u(r)* is equal to:

$$u(r) = \sqrt{\left(\frac{\partial r}{\partial K_{m1}} \cdot u\left(K_{m1}\right)\right)^2 + \left(\frac{\partial r}{\partial K_{m2}} \cdot u\left(K_{m2}\right)\right)^2 + \left(\frac{\partial r}{\partial \rho_1} \cdot u\left(\rho_1\right)\right)^2 + \left(\frac{\partial r}{\partial \rho_2} \cdot u\left(\rho_2\right)\right)^2 + \left(\frac{\partial K}{\partial k_T} \cdot u\left(k_T\right)\right)^2} \tag{A.10}$$

Table A.5: Uncertainty budget for density correction coefficient *r*.

Quantity	**Unit**	**Value** x_i	$u(x_i)$	**Probability distribution**	**Sensitivity coefficient** $c(x_i)$	$c(x_i) \cdot u(x_i)$ **in dm³/kg**	**% of total**
K_{m1}	pulse/kg	10,081	0,011	normal	$-4{,}6 \cdot 10^{-3}$	$-5{,}08 \cdot 10^{-2}$	21%
K_{m2}	pulse/kg	13,146	0,027	normal	$3{,}5 \cdot 10^{-3}$	$9{,}68 \cdot 10^{-2}$	77%
ρ_1	kg/m³	998	0,10	rectangular	$-3{,}8 \cdot 10^{-5}$	$-3{,}83 \cdot 10^{-3}$	0%
ρ_2	kg/m³	718	0,29	rectangular	$5{,}1 \cdot 10^{-5}$	$1{,}46 \cdot 10^{-2}$	2%
k_T	-	1,0045	$5{,}0 \cdot 10^{-5}$	rectangular	$-2{,}0 \cdot 10^{-2}$	$-1{,}00 \cdot 10^{-5}$	0%
r	**dm³/kg**	**1,71**	**0,11**				**100%**

The uncertainty budget is presented in Table A.5. Relative standard uncertainty of density correction coefficient *r* is equal to 6,4%.